

EMPIRICAL INVESTIGATION OF CO₂ UTILIZING ROOM TEMPERATURE
IONIC LIQUIDS

by

Edward William Graef Jr.



APPROVED BY SUPERVISORY COMMITTEE:

Shalini Prasad, Chair

Phillip C. Anderson

Lloyd Lumata

Jason D. Slinker

Copyright 2018

Edward William Graef Jr.

All Rights Reserved

This dissertation is dedicated to my wife and family. Who, through the years of education and hardships, have always been there to be an ear to listen or a voice of encouragement.

EMPIRICAL INVESTIGATION OF CO₂ UTILIZING ROOM TEMPERATURE
IONIC LIQUIDS

by

EDWARD WILLIAM GRAEF JR., BS, MS

DISSERTATION

Presented to the Faculty of
The University of Texas at Dallas
in Partial Fulfillment
of the Requirements
for the Degree of

DOCTOR OF PHILOSOPHY IN
PHYSICS

THE UNIVERSITY OF TEXAS AT DALLAS

May 2018

ACKNOWLEDGMENTS

I would first like to thank my advisor Dr. Shalini Prasad for giving me this opportunity to work on this SRC sponsored project. I would also like to thank my committee for taking their time to review and offer advice where necessary upon my research path. I would also like to thank the Semiconductor Research Council who funded this work. I would like to thank my industrial liaisons Rujuta Munje and Arthur Turner for helping guide this project toward developing a sensor. Thanks also goes to Badrinath Jagannath and Ashlesha Bhide for working on this SRC project and as we all worked together to provide the necessary updates to both our industry liaisons as well as the SRC. I would like to thank everyone in the BMNL group for reviewing papers, asking questions, and being sounding boards when preparing presentations. Finally, I would like to thank my wife Robin and my parents Ed and Dawn for being huge pillars of support through my life. I am sure I would not have made it this far without them.

December 2017

EMPIRICAL INVESTIGATION OF CO₂ UTILIZING ROOM TEMPERATURE IONIC LIQUIDS

Edward William Graef Jr., PhD
The University of Texas at Dallas, 2017

Supervising Professor: Shalini Prasad

Since the start of the industrial revolution, atmospheric carbon dioxide levels have been on the rise. CO₂ detection has been made possible through a number of different techniques though they all suffer one way or the other from cross-sensitivity, narrow temperature operation range, high temperature or power operation, or limited lifetimes due to exposure to CO₂. Room temperature ionic liquids are a purely ionic solution consisting of tunable inorganic anions and organic cations. Salt like in nature with below room temperature melting points, these novel materials express tunable physical and chemical properties that can be selected to make them highly sensitive to CO₂. Through the selection of different fluorinated anions, this work shows the empirical development of a CO₂ gas sensor as part of a SRC sponsored research project from initial evaluation of some of the RTILs physical properties, electrode design evaluation, through to the examination of down selected RTILs on gold interdigitated electrodes at different humidity and temperature conditions. EMIM[TF₂N] is shown as the front runner as the future RTIL for integration into an Arduino based prototype CO₂ gas sensing system.

TABLE OF CONTENTS

ACKNOWLEDGMENTS	v
ABSTRACT.....	vi
LIST OF FIGURES	ix
LIST OF TABLES	xiii
CHAPTER 1 INTRODUCTION	1
1.1 Health Effects	1
1.2 Current Sensing Methods	3
1.3 Room Temperature Ionic Liquids	6
CHAPTER 2 PHYSICAL EVALUATION	18
2.1 Initial physical properties of RTILs on different substrates	18
2.2 Materials and Methods	21
2.3 Discussion	29
CHAPTER 3 ELECTROCHEMICAL BASIS AT ROOM TEMPERATURE.....	31
3.1 Aim: Exploring a new RTIL with respect to cycling for efforts towards CO2 sensing in ideal conditions	31
3.2 Cyclic Voltammetry	32
3.3 Electrochemical Impedance Spectroscopy	33
3.4 Methods & Materials	35
3.5 Experimental Procedure	38
3.6 Results & Discussion.....	39
3.7 Conclusion.....	54
CHAPTER 4 RTILS AT ELEVATED TEMPERATURE AND HUMIDITY	55
4.1 Aim: Temperature and Humidity studies towards development of a portable low powered sensor.	55
4.2 Experimental Procedure and Setup	55
4.3 Temperature Results.....	57
4.4 Temperature and Humidity Results of RTILs	59

CHAPTER 5 CONCLUSIONS AND FUTURE EFFORTS	73
5.1 Conclusions on the Use of RTILs in residual CO ₂ gas sensing.....	73
5.2 Future work utilizing RTILs in gas sensing	74
APPENDIX.....	77
EMIM[TF ₂ N] plots at 45 %RH and 45 °C.....	77
EMIM[FAP] plots at 25 %RH and 25 °C	79
Overall DOE results for all combinations of CO ₂ , humidity, and temperature	82
BIBLIOGRAPHY.....	83
BIOGRAPHICAL SKETCH	88
CURRICULUM VITAE	

LIST OF FIGURES

Figure 1: Carbon dioxide main toxicity symptoms across different CO ₂ ranges. [11].....	2
Figure 2: Summary detailing the different CO ₂ sensing systems available on the market and some of their major drawbacks for use across a wide range of industries.	4
Figure 3: Graphic depicting just some of the many different applications that RTILs have been explored for or are being used in. [21,22].....	6
Figure 4: Schematic showing the alignment that can occur at the surface of an electrode coated in RTIL.....	8
Figure 5: Schematic showing basic model of the Gouy-Chapman-Stern theory.....	12
Figure 6: Schematic showing that as the potential at the electrode surface is increased the density of the anion or cations increases with respect to the potential applied creating a so-called over-screening effect.....	17
Figure 7: Sample droplet with a simulated least square fit.	20
Figure 8: Schematic showing how the contact angle can be calculated from the interface between the solid, liquid, and gas regimes.....	21
Figure 9: Goniometer from Ramé-Hart for use in the measurement of RTILs contact angle and surface tension.	22
Figure 10: Schematics of the different components that make up the different RTILs investigated. a) EMIM cation, b) BF ₄ anion, c) FAP anion, and d) TF ₂ N anion.	23
Figure 11: Schematic detailing layout of designed interdigitated electrodes.	24
Figure 12: Microscope image of a) IDEs on standard 4 in. silicon wafer. b) IDEs on standard glass microscope slide.....	25
Figure 13: Fabrication process for 4-inch silicon wafers for the construction of gold IDE electrodes. The finished electrodes consisted of 200nm of Cr with 700nm of Au.....	26
Figure 14: Microscopic image of gold electrodes to confirm lack of yield issues.	27
Figure 15: Contact angle calculation for EMIM[BF ₄] on gold electrodes deposited on both silicon wafers (left) and glass microscope plates (right).	28
Figure 16: EMIM[BF ₄] Pendant drop that was allowed to form on a 28 gauge flat nose needle for surface tension calculation.	29

Figure 17: Generic cyclic voltammogram showing the oxidation and reoxidation behavior for an arbitrary system. I_{pa} and i_{pc} stand for the peak anionic and peak cathodic current respectively.	32
Figure 18: Bode Nyquist results of a detector coated in EMIM[BF ₄] in and N ₂ environment scanned at 3.5 V with a perturbation voltage of 0.1 V at 0.1 Hz to 200 kHz.	34
Figure 19: Equivalent Randles Circuit that allows for the investigation of different components of an electrochemical based system.	35
Figure 20: Fitting parameters utilized to extract and differentiate between bulk and EDL effects.	35
Figure 21: Fitted Nyquist and Body plots with fitting lines created from the equivalent circuit and empirical data.	36
Figure 22: a) Initial layout and design schematic of environmental testing system. b) Final layout of testing system utilizing a dry box, potentiostat, gas mixer, hot plate, Vaisala sensor, and secondary testing box. The inset shows the secondary test box with input from the gas mixer and Vaisala for measurement of actual mixing output for offset adjustments.	37
Figure 23: Carbon pasted IDE from PCBUniverse, Inc. (left). Gold IDE with RTIL deposited from PCBUniverse (right).	38
Figure 24: Cyclic Voltammogram (CV) for EMIM[BF ₄]. The applied voltage was swept at a rate of 500 mV/s from -2.5 V to 3.5 V. For each concentration of CO ₂ , 400, 750, and 100ppm respectively, were compared.	40
Figure 25: Cyclic voltammogram for EMIM[FAP] with a voltage sweep at 500 mV/s from -2.5V to 3.5V. Each CV is the average of 3 cycles at the different CO ₂ concentrations of 400, 750, and 1000 ppm.	41
Figure 26: Impedance and phase dependence on frequency with a) EMIM[BF ₄], b) EMIM[TF ₂ N], and c) EMIM[FAP] on IDE carbon Paste electrodes.	43
Figure 27: Extracted capacitance response with a) EMIM[BF ₄], b) EMIM[TF ₂ N], and c) EMIM[FAP] on IDE carbon Paste electrodes with and without the RTILs present on the electrodes.	44
Figure 28: Impedance and phase dependence on frequency with a) EMIM[BF ₄], b) EMIM[TF ₂ N], and c) EMIM[FAP] on gold IDEs.	46
Figure 29: Extracted capacitance response with a) EMIM[BF ₄], b) EMIM[TF ₂ N], and c) EMIM[FAP] on gold IDEs with (left axis) and without (right axis) RTILs present.	49

Figure 30: a) Nyquist plot showing the behavior of EMIM[BF ₄] when exposed to N ₂ baseline to 1000ppm CO ₂ . b) Bode plots for N ₂ up to 1000ppm CO ₂ exposure. c) Extracted resistance change from the detectors tested with EMIM[BF ₄]. Adapted from “A Robust Electrochemical CO ₂ Sensor Utilizing Room Temperature Ionic Liquids,” by E. Graef, R. Munje, and S. Prasad, 2017, IEEE Nanotechnology Transactions, Vol. 16, No. 5, pg. 828-829.....	50
Figure 31: a) Nyquist plot showing the behavior of EMIM[TF ₂ N] when exposed to N ₂ baseline to 1000ppm CO ₂ . b) Bode plots for N ₂ up to 1000ppm CO ₂ exposure. c) Extracted resistance change from the detectors tested with EMIM[TF ₂ N]. d) Extracted capacitance change of EMIM[TF ₂ N] after exposure to different concentrations of CO ₂ . Adapted from “A Robust Electrochemical CO ₂ Sensor Utilizing Room Temperature Ionic Liquids,” by E. Graef, R. Munje, and S. Prasad, 2017, IEEE Nanotechnology Transactions, Vol. 16, No. 5, pg. 829-830.....	51
Figure 32: Nyquist plot of EMIM[FAP] when exposed to different levels of CO ₂ concentration. a) 400ppm, b) 750ppm, and c) 1000ppm.	53
Figure 33: Phase response of EMIM[FAP] over different CO ₂ concentrations from 400ppm to 1000ppm compared to their N ₂ baseline phase response.	54
Figure 34: Nyquist plot of EMIM[TF ₂ N] at 65 %RH and 65°C. This shows the change from N ₂ baseline to N ₂ with humidity to 400ppm CO ₂ with humidity.	60
Figure 35: Nyquist plot of EMIM[TF ₂ N] at 65 %RH, 65 °C, and 750ppm.	61
Figure 36: Nyquist plot for EMIM[TF ₂ N] at 65 %RH and 65 °C with 400ppm CO ₂	62
Figure 37: Nyquist plot of EMIM[FAP] at 45 %RH and 45 °C in 1000ppm CO ₂	63
Figure 38: Nyquist plot of EMIM[FAP] at 45 %RH and 45 °C with 750ppm CO ₂	64
Figure 39: Nyquist plot of EMIM[FAP] at 45 %RH and 45 °C in 400ppm CO ₂	65
Figure 40: Nyquist plot of EMIM[TF ₂ N] at 25 %RH and 25 °C at 1000ppm CO ₂	66
Figure 41: Nyquist plot of EMIM[TF ₂ N] at 25 %RH and 25 °C at 750ppm CO ₂	67
Figure 42: Nyquist plot of EMIM[TF ₂ N] at 25 %RH and 25 °C at 400ppm CO ₂	68
Figure 43: Proposed interaction mechanism for EMIM[TF ₂ N] with the addition of heat, humidity, and CO ₂ concentrations.....	69
Figure 44: Proposed interaction mechanism for EMIM[FAP] with the addition of heat, humidity, and CO ₂ concentrations.	70

Figure 45: Schematic of the potential applied and possible current response from and electrochemical system when performing Chronoamperometry.	74
Figure 46: Mockup of EMIM[TF ₂ N] sensing system operating in ambient environment.	75
Figure 47: Mockup of EMIM[TF ₂ N] sensing system in an elevated CO ₂ environment.	76
Figure 48: Nyquist of EMIM[TF ₂ N] at 45 %RH and 45 °C at 1000ppm CO ₂	77
Figure 49: Nyquist of EMIM[TF ₂ N] at 45 %RH and 45 °C at 750ppm CO ₂	78
Figure 50: Nyquist plot of EMIM[FAP] at 25 %RH and 25 °C at 1000ppm CO ₂	79
Figure 51: EMIM[FAP] Nyquist plot of EMIM[FAP] at 25 %RH and 25 °C at 750ppm CO ₂	80
Figure 52: Nyquist plot of EMIM[FAP] at 25 %RH and 25 °C at 400ppm CO ₂	81

LIST OF TABLES

Table 1: NIOSH exposure parameters with corresponding CO ₂ concentrations. [11]	2
Table 2: List of Symptoms from elevated levels of CO ₂ exposure. [12].....	3
Table 3: Shows the selected RTILs for this work along with some of their key electrochemical and physical properties used in initial evaluation towards the development of a CO ₂ sensor...7	
Table 4: Henry's constant for the selected RTILs for select gases.	24
Table 5: Summary table for contact angles of different RTILs on Si-SiO ₂ gold and SiO ₂ gold electrode surfaces made through standard metal deposition fabrication techniques.	29
Table 6: Extracted capacitance values comparing open circuit capacitance without RTILs to the capacitance in N ₂ with the RTIL present.	45
Table 7: Extracted capacitance values comparing RTIL in N ₂ vs open circuit capacitance of the gold electrode without RTIL present.	48
Table 8: Extracted capacitance ratio response of the 3 RTILs being investigated investigated.	52
Table 9: Extracted resistance and capacitance values of EMIM[TF ₂ N] across 25, 45, and 65°C.	57
Table 10: Extracted capacitance and resistance values of EMIM[FAP] at 25, 45, and 65°C.	58
Table 11: Summary table showing the extracted capacitance change for EMIM[FAP] ad EMIM[TF ₂ N] at 65 %RH and 65 °C between N ₂ and CO ₂	63
Table 12: Summary table showing the extracted capacitance change for EMIM[FAP] ad EMIM[TF ₂ N] at 45 %RH and 45 °C between N ₂ and CO ₂	66
Table 13: Summary table showing the extracted capacitance change for EMIM[FAP] ad EMIM[TF ₂ N] at 25 %RH and 25 °C between N ₂ and CO ₂	68
Table 14: Summary of capacitance change to CO ₂ concentration as the temperature and humidity are varied for EMIM[FAP] and EMIM[TF ₂ N].....	72

CHAPTER 1

INTRODUCTION

Carbon dioxide levels have been rising year after year well past the start of the industrial revolution. [1,2] As science and technology have advanced, we have been able to better study and understand the effects different gases may have on our environment and, in turn, our own individual health. [2,3] Scientists have identified several different gases that contribute to the effects of global warming and, specifically, their greenhouse effects. The most common of the greenhouse gases (GHG) is carbon dioxide (CO₂). It is also the most common gas created anthropogenically as it comes from natural respiration as well as through industrial and energy generation processes. [4,5,6] For the first time in recorded history, the average CO₂ levels monitored at the Mauna Loa Observatory in Hawaii have not dropped below 400ppm for an entire year. [3,4,7] This has been a call for countries and scientists to develop better methods of detecting and monitoring CO₂ sources the world over. [6,7,8]

1.1 Health Effects

Through normal respiration, all living mammals emit CO₂. This emission normally is above 1000ppm and with low concentrations of atmospheric CO₂, humans are able to reliably exchange for a higher concentration of O₂. [9, 10] However, when in a high CO₂ environment, this exchange isn't enough. The human body begins to go through different phases as the O₂ becomes scarce. [10] Table 1 shows the overall exposure limits for people who work in potentially high CO₂ environments. [11]

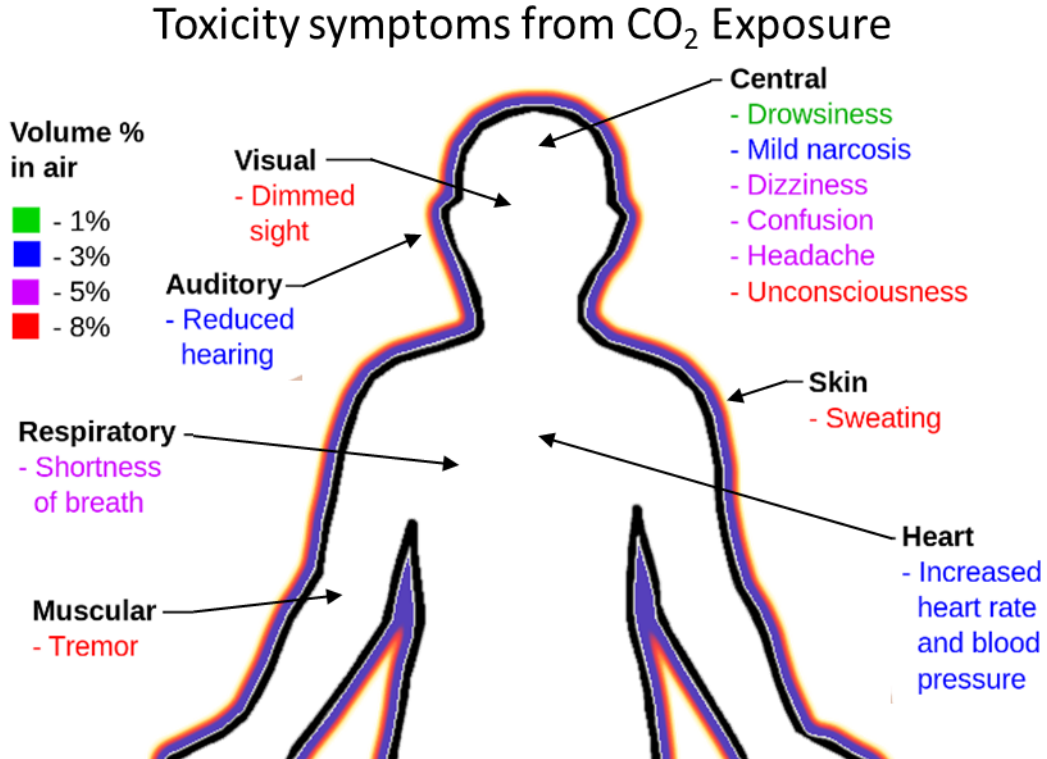


Figure 1: Carbon dioxide main toxicity symptoms across different CO₂ ranges. [11]

Table 1: NIOSH exposure parameters with corresponding CO₂ concentrations. [11]

NIOSH Exposure Parameters	CO ₂ Concentration	Exposure Level
Recommended Exposure Limit (REL)	5,000 ppm	8hr-Total working average (TWA)
TWA REL	10,000 ppm	10 minute average exposure
Short Term Exposure Limit (STEL)	30,000 ppm	15 minute average exposure
Immediately Dangerous to Life or Health (IDLH)	40,000 ppm	Health in immediate danger

Exposure to elevated levels of CO₂ also produce a myriad of different effects, Figure 1, than just headache, dizziness, unconsciousness, and death. Susan A. Rice and Associates released a paper detailing the effects of different concentrations of CO₂ on the human body. [12] Table 2

summarizes the regions of CO₂ and their corresponding health effects. It is important to note that increased breathing is always a leading symptom of low oxygen levels whether it be via exercise or high CO₂ concentration in the local environment. This shows that as CO₂ levels increase, we may not always notice once a dangerous environment is forming. [10]

Table 2: List of Symptoms from elevated levels of CO₂ exposure. [12]

CO2 Concentration	Effects
<3 %	Elevated respiration
3 to 5 %	Elevated respiration, heart rate, headaches, dizziness, and confusion
5 to 8 %	Respiration increase, dizziness, confusion, difficulty breathing
8 to 10+ %	Unbearable breathing issues, vomiting, disorientation, Increased blood pressure, and unconsciousness, death.

1.2 Current Sensing Methods

Carbon dioxide can be measured via several different methods. All have drawbacks with none really showing a clear wide application ability. The most common, non-dispersive infrared (NDIR) sensing, on the market are focused toward industrial or HVAC applications. [13] Other methods of sensing include electrolytic based and metal oxide based sensors.

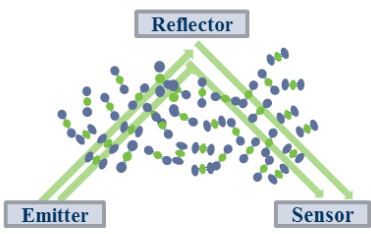
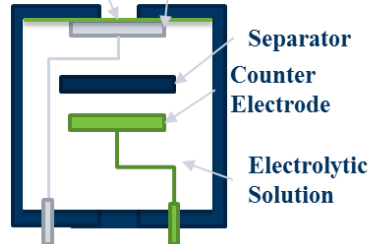
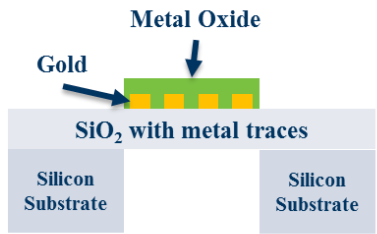
<p>Non-dispersive Infrared Sensor</p> 	<p>Electrochemical Sensor</p> 	<p>Metal Oxide Sensor</p> 
<ul style="list-style-type: none"> ▪ Long stabilization time (3+min) ▪ High power consumption ▪ High temperature operation ▪ Due to response time, may not see large changes in CO₂ on the order of minutes 	<ul style="list-style-type: none"> ▪ Life span is shortened via increased exposure to target gas. ▪ Response time is set by the time to diffuse through membrane ▪ Narrow temperature operation range ▪ Cross sensitivity issues: ie.CO & CO₂ 	<ul style="list-style-type: none"> ▪ High temperature operation. ▪ Diffusion limited ▪ Multiple gas cross sensitivities ▪ Purity issues during manufacturing

Figure 2: Summary detailing the different CO₂ sensing systems available on the market and some of their major drawbacks for use across a wide range of industries.

NDIR sensing has been available for several years. It consists of 3 different components; an IR emitter, a gas tube for alignment and air flow, and an IR detector, Figure 2. [13] Through tuning of the tuning of the blackbody, it is possible to select the necessary wavelengths for the detection of different absorbing gas species. One of the drawbacks of this type of sensor is the cross sensitivity with respect to other gases such as CO. [14] Other concerns are the necessary high temperature operation of the IR emitter as well as the high power (>12V) requirements of the total system. Even the geometry of some of the latest on-board NDIR sensors exceed easy integration into a wearable sensing system. [14,15]

Metal Oxide based sensors for different gases have been explored for their applications for detecting volatile organic compounds (VOCs) as well as for their ability to detect CO₂ and other gases. [16] These metal oxide sensors come in many different forms, but most rely on the

deposition and construction of surface based nanostructures and texturing in order to sense their specific molecule. [17] Some of the drawbacks for these sensors are that they can suffer greatly from cross sensitivity issues, operate at high temperatures due to the need to create reactive species of the gases to be sensed, as well as manufacturing issues to create consistent sensing materials. [16,17,18]

The last form of sensor that has been reviewed are those that are electrochemically sensitive to the different gases. These consist of a 2 or 3 electrode based system that are either submerged within a liquid electrolyte or have a solid electrolyte deposited on top of them, Figure 2. [19] The electrolyte covers the electrode system. While some offer low power and small geometry solutions, they still have drawbacks. Most low temp sensors of this type suffer from severe cross sensitivity issues and a very narrow temperature range of operation. Some electrolytes used also suffer from nonreversible reactions, so if placed in large concentrations of the analyte, they eventually become saturated and unable to detect changes. [20]

As summarized in Figure 2, all of these sensors are capable of monitoring CO₂ but suffer from one issue or another. Only through the development and application of new materials and technologies will it be possible to create new and novel sensors. [20] They must have sensitivity to CO₂, large impedance response, easy to deposit, and have high temperature tolerance. One such class of materials that fit these requirements are called room temperature ionic liquids. [21]

1.3 Room Temperature Ionic Liquids

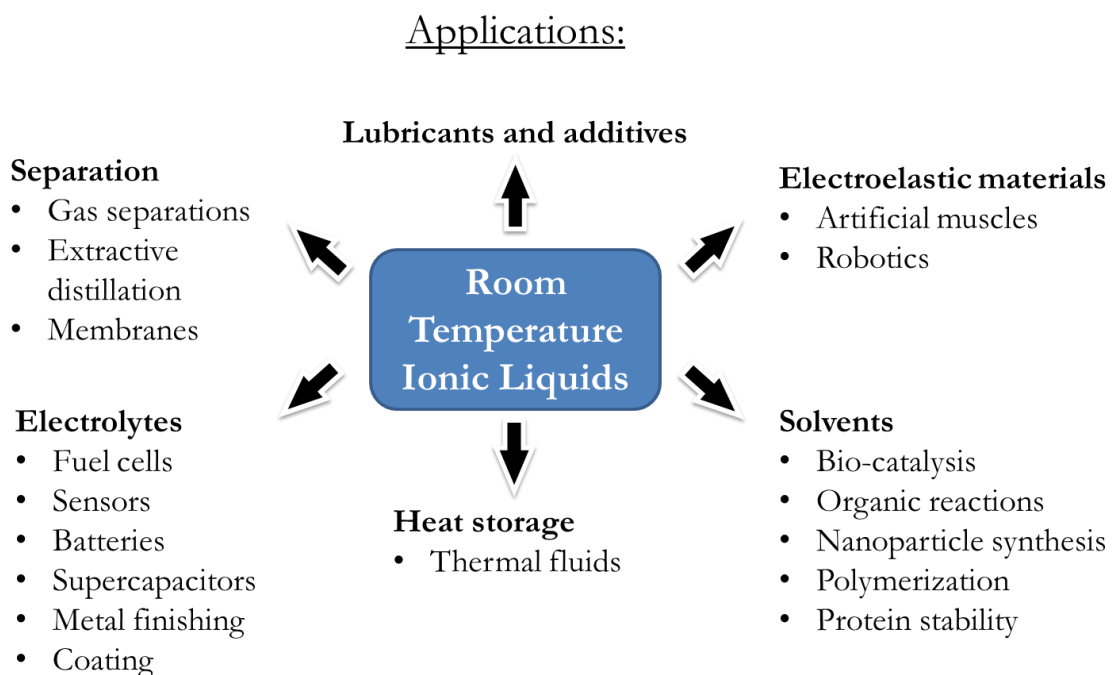


Figure 3: Graphic depicting just some of the many different applications that RTILs have been explored for or are being used in. [21,22]

Room temperature ionic liquids (RTILs) are a unique class of materials that have been utilized for a lot of different applications, Figure 3. [21,22,23] Ionic liquids & molten salts were first discovered in the middle of the 19th century. A so called “red oil” was observed during specific organic reactions. [24] The generation process for these liquids was patented, but was never widely used in any industry. It wasn’t until the middle of the early to middle 20th century that the more widely used alkylammonium nitrate based ionic liquids were discovered during thermal battery improvement research funded by the U.S. Air Force Research Laboratory. From this research, N-pyridinium and N-limidazolim based ionic liquids were discovered and investigated. [25] These cation/anion pairs were aimed at reducing the melting point of the electrolytes for better thermal

performance. [24, 25] From these initial investigations, it was also discovered that both of the cations reacted easily with water. To help combat this reactivity, inorganic hydrophobic anions such as tetrafluoroborate (BF_4), bis(trifluoromethane)sulfonimide (TF_2N or TFSI), as well as other sulfates and fluorine based anions were utilized. [25,26,27,28,29]

Table 3: Shows the selected RTILs for this work along with some of their key electrochemical and physical properties used in initial evaluation towards the development of a CO_2 sensor.

	RTIL	Decomposition temp	Electrochemical Window	Density
1	EMIM [TF_2N]	455 °C	4.9 V	0.139 g/mL
2	EMIM[BF_4]	350 °C	4.7 V	1.294 g/mL
4	EMIM [FAP]	300 °C	4.4 V	1.732 g/mL

The specific fluorine based anions shown in Table 1 combined with the 1-ethyl-3-methylimidazolium (EMIM) have been shown in previous research and applications as having a sensitivity towards CO_2 physi-sorption. [28,30] This interaction has also been shown to be reversible with the application of thermal energy, i.e. heating. [26] Just recently it was shown that if one were to wait a sufficiently long enough amount of time (hours) different ionic liquids will equilibrate with the CO_2 concentration in the atmosphere as well. [32] Both observations suggest that through the further interface investigations, an electrochemical based sensor could be developed for CO_2 sensing.

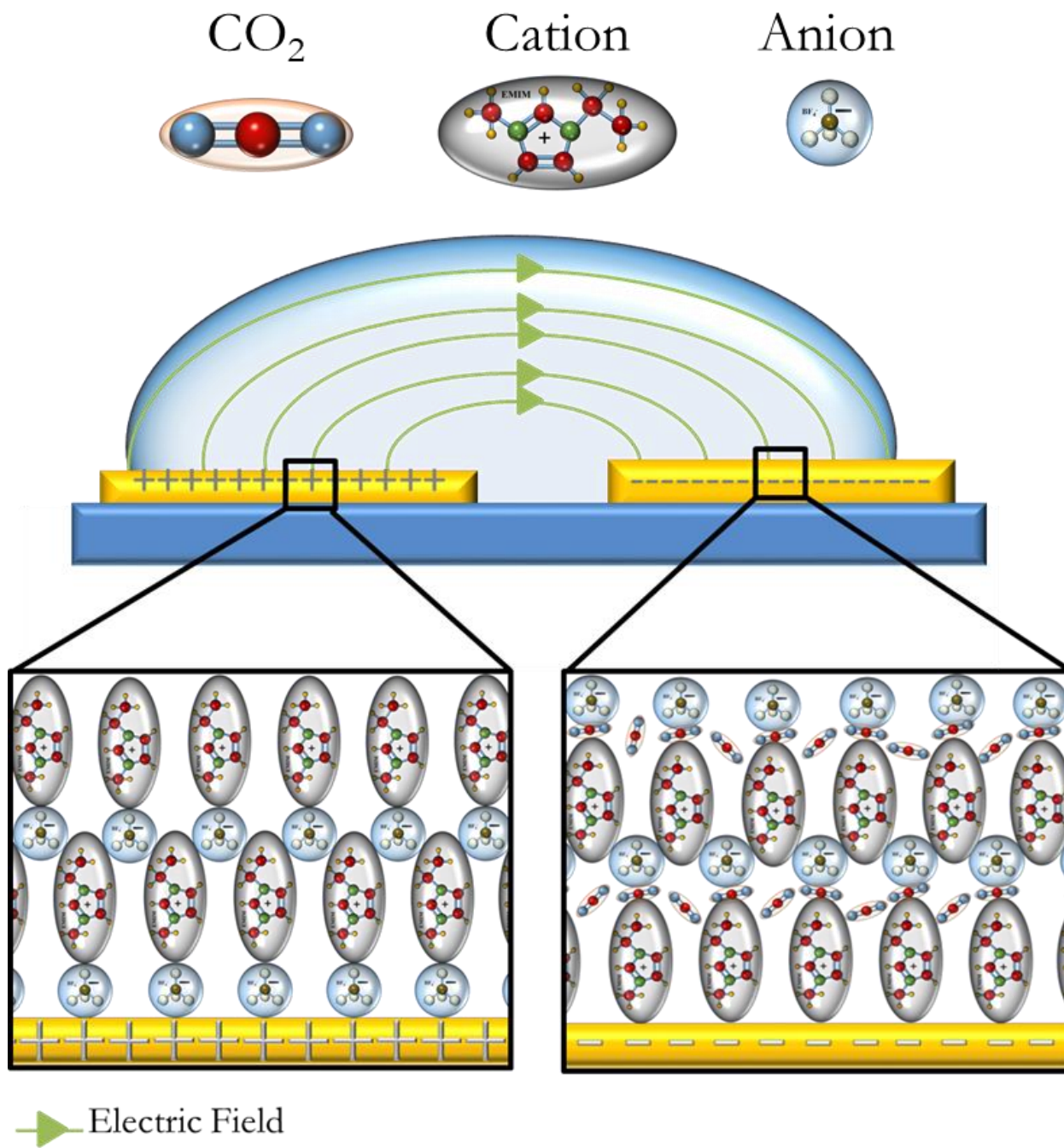


Figure 4: Schematic showing the alignment that can occur at the surface of an electrode coated in RTIL.

When one deposits this material onto some form of conductive or charged surface, an interesting thin film forms. [35,36] When the RTIL is first applied to a conductive surface, the closest layer of liquid, aligns itself with the potential at the surface, Figure 4. [36] This layer, called an electrochemical double layer (EDL), an important and vital behavior that scientists can exploit in efforts of developing electrochemical based sensing techniques.

Theoretically, for an electrolyte to form an EDL, one must recall a comparison to a basic dielectric based capacitor. When a potential is present of any kind, the dielectric will polarize such that a counter charge of ions forms on either of the plates of the capacitor. [39] This layer of ions, termed the Helmholtz layer, leads to behavior similar to the standard capacitance behavior of an ideal capacitor, Equation 1.

$$C_H = \frac{\epsilon^*}{4\pi d}$$

Equation 1

From previous literature, it was discovered that for EDL bases systems, it is not only a single layer of ions that are attracted to the given electrode. [39,40] What is unique to RTILs and most electrolytes is that their EDL do not follow this behavior. Gouy and Chapman, at the turn of the twentieth century, independently developed a new theory taking into account that EDLs are not only one layer deep. [39,41] They in fact have multiple layers of anions and cations that oscillate back in forth until thermal forces dominate. The thickness of this layer is dependent on both the temperature and potential the material experiences and can be quantified in the following section.

1.3.1 Gouy-Chapman-Stern Theory

As discussed above, when a voltage is applied to a metallic electrode in, an electrolyte will orient in efforts to cancel out the potential it sees. From the first principle of the Gauss Law, a metallic conductor contains all of it's charge on the surface. Considering a Gaussian surface enclosing

$$q = \epsilon_o \oint \vec{E} \cdot d\vec{S}$$

Equation 2

For Equation 2, E is the applied electric field, ϵ_o is the permittivity of free space, and dS is the vector normal from the surface pointed outward. If there is no current flowing, i.e. $I = 0$, then $E = 0$ at the surface of the Gaussian body. This allows for the conclusion that there is no net charge within the boundary of the surface. Therefore any excess charge will reside on the surface of these conductive electrodes.

Given a good conductor as the electrode, what happens when we deposit a dielectric on top of this electrode? If a potential is applied to the electrode, a charge q will reside on its surface. This charge will cause an excess of ions to concentrate near the electrode surface. Again, applying the Gauss Law, it can be shown that in a static state with no current flowing, $E = 0$ at all points. Therefor total charge $q = 0$ and implies that the $q_{\text{dielectric}} (q_d) = -q_{\text{metal}}(q_M)$.

Helmholtz postulated that due to the charge residing at the surface of a polarized perfect conductor. [31, 37, 38, 41, 42] A counter charge surrounds and encapsulates this conductor near the surface when in an ionic electrolyte solution. Due to these ions not being point charges, there would be some separation distance between the ion cloud and conductor surface approximately

the size of the molecular separation for the given solution. This behavior can be compared to that of a parallel plate capacitor shown in Equation 3. [34]

$$\sigma = \frac{\epsilon\epsilon_0}{d}V$$

Equation 3

Where σ is the charge density, ϵ is the dielectric constant of the medium, d is the plate spacing, and V is the applied potential. The capacitance is calculated by differentiating with respect to the voltage.

$$C_d = \frac{\partial\sigma}{\partial V} = \frac{\epsilon\epsilon_0}{d}$$

Equation 4

It is important to note that the capacitance of this layer is a constant dependent upon the on the behavior of the medium. However, it has been empirically observed that as one varies the ionic concentration of the solute and the applied potentials, C_d continues to vary. Therefore, the Helmholtz behavior is insufficient for describing the overall interface behavior of this system.

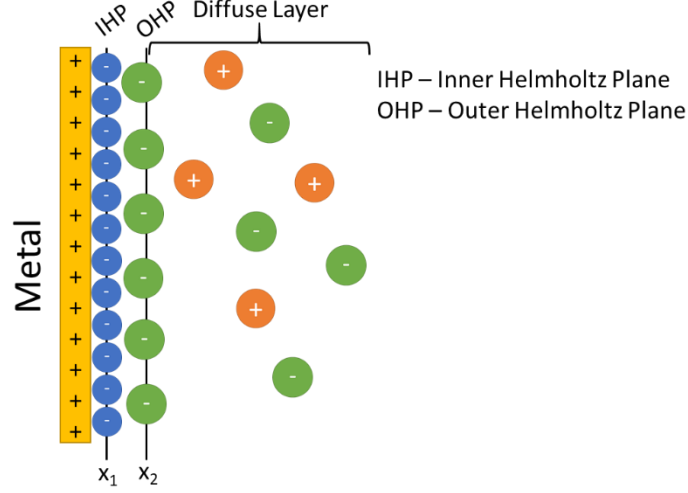


Figure 5: Schematic showing basic model of the Gouy-Chapman-Stern theory.

Both Louis Gouy and David Chapman proposed a form of diffuse layer that occurs at electrode surface that relied on the electrodynamic and thermodynamic behavior of the system. [37, 38, 40, 41] Consider that this diffuse layer will consist of oscillating layers that will form due to the application of a potential to a good conductor immersed in an electrolytic solution. A bunch of small layers the size of dx should form. In these different layers, due to the small changes in potential, the individual ions will exist at different energy levels. This behavior can be described utilizing a standard Boltzmann distribution.

$$n_i = n_o^i e^{\left(\frac{-z_i e V}{k T}\right)}$$

Equation 5

The charge density per unit volume can be defined as

$$\rho(x) = \sum_i e z_i n_i = e \sum_i n_i^o z_i e^{\left(\frac{-e z_i V}{k T}\right)}$$

Equation 6

Through this substitution, Poisson-Boltzmann statistics can be developed such that:

$$\frac{d^2V}{dx^2} = -\frac{e}{\varepsilon\varepsilon_o} \sum_i n_i^o z_i e^{\left(\frac{-z_i eV}{kT}\right)}$$

Equation 7

Recalling that $\frac{d^2y}{dx^2} = \frac{1}{2} \frac{d}{dy} \left(\frac{dy}{dx} \right)^2$ and substituting accordingly for Equation 7 allows for simplification.

$$\left(\frac{dV}{dx} \right)^2 = \frac{2kT}{\varepsilon\varepsilon_o} \sum_i n_i^o \left[e^{\left(\frac{-z_i eV}{kT}\right)} - 1 \right]$$

Equation 8

Now given the fact that $V = 0$ far from the electrode, $dV/dx = 0$, and the electrolyte components are symmetrical yields:

$$\left(\frac{dV}{dx} \right)^2 = \frac{2kT}{\varepsilon\varepsilon_o} n_i^o \left[e^{\left(\frac{-z_i eV}{kT}\right)} - 1 + e^{\left(\frac{z_i eV}{kT}\right)} - 1 \right]$$

Equation 9

Through simplification and a Pythagorean like identity, it is found that

$$\frac{dV}{dx} = -\left(\frac{8kTn^o}{\varepsilon\varepsilon_o} \right) \sinh\left(\frac{zeV}{2kT} \right)$$

Equation 10

To calculate the differential capacitance, it requires the application of the Gauss law and understand that the electric field is zero at all points of the Gaussian surface. Therefore $q/A = \sigma^S = \epsilon\epsilon_o(dV/dx)$ evaluated at the surface such that $x = 0$. This can be equated to σ^M .

$$\sigma^M = -\sigma^S = (8kT\epsilon\epsilon_o n^o)^{1/2} \sinh\left(\frac{zeV_o}{2kT}\right)$$

Equation 11

Now that the surface charge density has been calculated, the differential capacitance can finally be calculated.

$$C_d = \frac{d\sigma^M}{dV_o} = \left(\frac{2z^2 e^2 \epsilon\epsilon_o n^o}{kT}\right)^{1/2} \cosh\left(\frac{zeV_o}{2kT}\right)$$

Equation 12

Equation 12 was first used to describe the solution capacitance of these electrolyte systems, but theory diverged from empirical evidence. As the potential and/or electrolyte concentration was increased, the differential capacitance was observed to flatten out. [41, 42] Whereas for the theoretical predictions, the C_d would continue to increase indefinitely. A modification to the theory was needed to understand what was occurring to cause the flattening effect.

Stern suggested the use of an interfacial model that utilizes the Poisson-Boltzmann equations and solutions discussed previously, but suggested an additional set of layers shown in Figure X from x to x_2 . His proposal suggested that at high potentials and/or ion concentrations that an outer Helmholtz like plane would form due to a compression effect outside the inner Helmholtz layer. Following a similar process as laid out above, the GC theory yields

$$\sigma^M = -\sigma^S = \varepsilon\varepsilon_o \left(\frac{dV}{dx} \right)_{x=x_2} = (8kT\varepsilon\varepsilon_o n^o)^{1/2} \sinh\left(\frac{zeV_2}{2kT}\right)$$

Equation 13

The total potential drop across this new layer is given by $V_o = V_2 - \left(\frac{dV}{dx} \right)_{x=x_2} * x_2$. Substituting this into Equation 13 allows for the final calculation of differential capacitance which is shown below.

$$C_d = \frac{d\sigma^M}{dV_o} = \left(\frac{2\varepsilon\varepsilon_o (ze)^2 n^o}{kT} \right)^{1/2} \left(\frac{\cosh(zeV_2/2kT)}{1 + \left(\frac{x_2}{\varepsilon\varepsilon_o} \right) \left(\frac{2\varepsilon\varepsilon_o (ze)^2 n^o}{kT} \right)^{1/2} \cosh(zeV_2/2kT)} \right)$$

Equation 14

From this, C_d can be simplified such that two independent terms are observed.

$$\frac{1}{C_d} = \frac{x_2}{\varepsilon\varepsilon_o} + \left(\left(\frac{2\varepsilon\varepsilon_o (ze)^2 n^o}{kT} \right)^{1/2} \cosh eV_2/2kT \right)$$

Equation 15

These two components are proportional to two different capacitors in series with each other. These components represent the outer Helmholtz plane and diffuse charge region respectively. This Gouy-Chapman-Stern model has been shown to adequately represent ionic solutions of different concentrations across different applied potentials. [39, 40, 41] However, undiluted RTILs being of a pure liquid electrolyte causes this model to not adequately describe the behavior of the system.

There are currently several competing theories on how the EDL is formed for RTILs. [39, 41, 42] From a multilayer model suggested by A. Koryshev et. al. to the regular solution theory

proposed by S. Moganty and R. Baltus. The interface behavior of RTILs as they are perturbed is still being actively researched. [39, 40, 41, 42]

What is known though is that as the potential of the system is increased an “over-crowding” effect can occur, Figure 6. [42] This effect creates, in theory, a very dense EDL region that will respond significantly when perturbed via changes in its environment. This layer has been confirmed via atomic force microscopy by Atkins and Warr. [43] It is this effect that is hoped to be exploited for CO₂ sensor development and evaluation.

The work of this dissertation is to address the requirements set forth by the SRC documents, including industrial liaison guidance, to investigate and develop a CO₂ gas sensor utilizing room temperature ionic liquids. The requirements for the system include determining some of the initial physical parameters towards process development on gold such as contact angle and surface tension. Construction of an environmental chamber was paramount in being able to evaluate the CO₂ sensitivity of these fluorinated RTILs for 400, 750, and 1000ppm. Another requirement of these RTILs was that they be able to show a trend in sensitivity across a selection of different humidity (25%, 45%, and 65% relative humidity) and temperature (25°C, 45°C, and 65 °C) values. From these results down selection was to occur till the best choice of RTIL was proposed for the final project, developing a working prototype that can differentiate between ambient and elevated CO₂ levels.

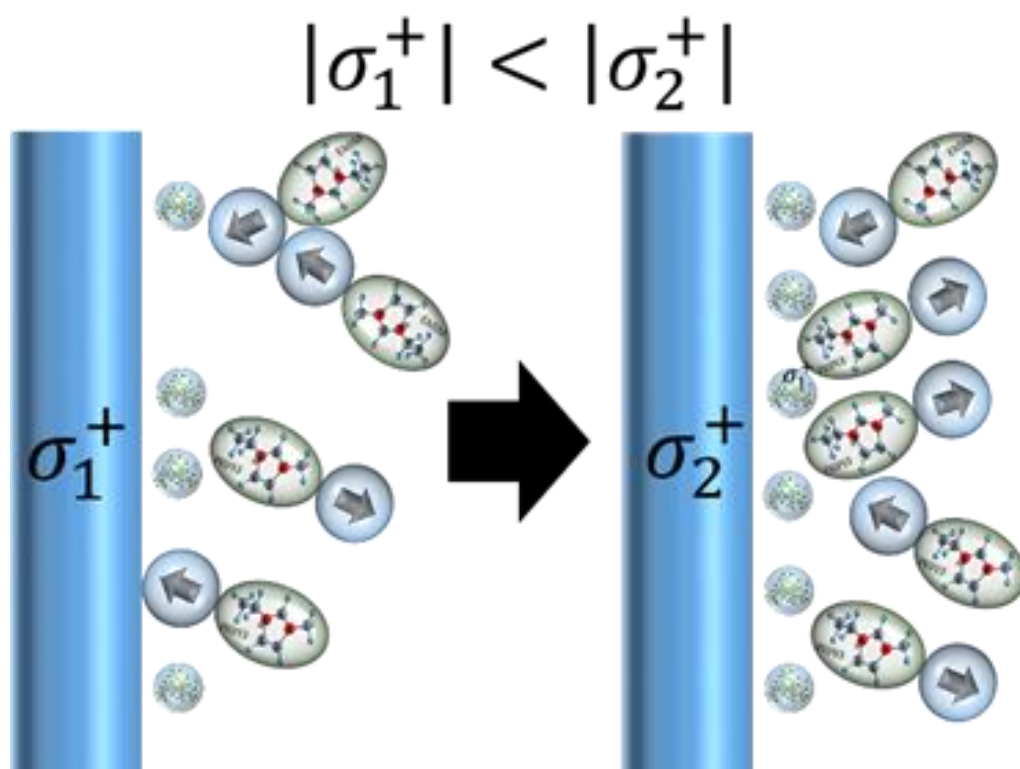


Figure 6: Schematic showing that as the potential at the electrode surface is increased the density of the anion or cations increases with respect to the potential applied creating a so-called over-screening effect.

CHAPTER 2

PHYSICAL EVALUATION

2.1 Initial physical properties of RTILs on different substrates

In efforts towards developing a CO₂ sensor utilizing RTILs, understanding how the material will interact with different sets of electrodes and some of their physical properties is needed. Measurement of both their surface tension and contact angle lend insight into how RTILs will work in terms of EDL interface formation as well as some manufacturability behavior. [42] Part of this work was completed and accepted for publication in IEEE Nanotechnology Transactions. It was titled “A Robust Electrochemical CO₂ Sensor Utilizing Room Temperature Ionic Liquids.” [54]

2.1.1 Surface tension (γ) calculations

There are multiple ways in which to measure surface tension. The most common of methods utilizes the Young-Laplace Equation, Equation 16. [43,44]

$$\Delta p = \gamma \left(\frac{1}{R_1} + \frac{1}{R_2} \right)$$

Equation 16

Here in Equation 16, Δp is the pressure differential of two liquids at the interface, γ is the surface tension (dynes/cm), and R_1 and R_2 are the principle radii of curvature. From Equation 16, we can determine the interfacial tension γ if we know the drop phase density. [43]

$$\gamma = \left(\frac{1}{R_1} - \frac{1}{R_2} \right)^{-1} (\Delta P_0 - \Delta \rho g z)$$

Equation 17

In Equation 17 we see that if we know the density of both the air and liquid. Utilizing symmetry as well as changing into a spherical coordinate system, it is possible to develop a set of dimensionless differential equations, Equation 18,

$$\frac{d\varphi}{ds} = 2 - B_0 z - \frac{\sin\varphi}{r}$$

$$\frac{dr}{ds} = \cos\varphi$$

$$\frac{dz}{ds} = \sin\varphi$$

Equation 18

From these differential equations, it is possible to extract a solution to be solved with respect to the Bond number, Equation 19. The Bond number is a dimensionless number commonly used in fluid dynamics. [44]

$$B_0 = \frac{\Delta\rho g R_0^2}{\gamma}$$

Equation 19

From these set of equations, it is now possible to start to calculate the surface tension of the given liquid. What comes next is taking an image of a droplet and, using a form of linear least squares fit, defining the radii (ideally $R_1=R_2=R_0$) of the droplet that is being analyzed, Figure 7.

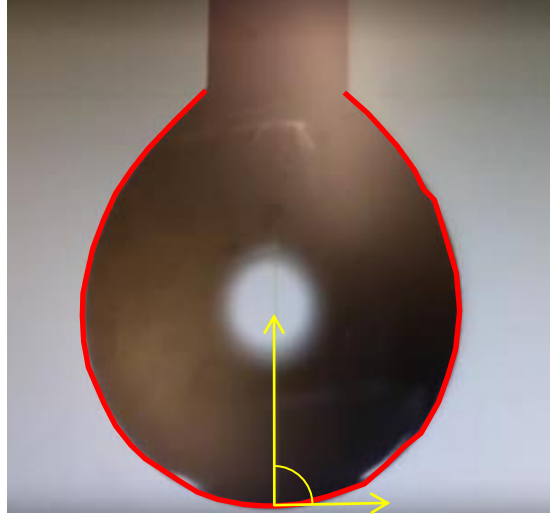


Figure 7: Sample droplet with a simulated least square fit.

Once this least squares fit is found, utilizing $z = r = \phi = 0$ as an initial condition, the actual surface tension γ can be calculated. This is all performed systematically and automatically utilizing the Ramé-Hart goniometer. [45,46]

2.1.2 Contact angle χ measurements

Contact angle is also another parameter that gives insight into the physical characteristics of a material on a solid surface in a gaseous environment. At equilibrium, Figure 8, the tension being exerted on and exerted by the liquid, surface, and environment allows for the following Young relation to hold true. [47,48]

$$r_{gs} = r_{ls} + r \cos \chi$$

Equation 20

From Equation 20, the contact angle can be solved such that

$$\cos \chi = \frac{r_{gs} - r_{ls}}{r}$$

Equation 21

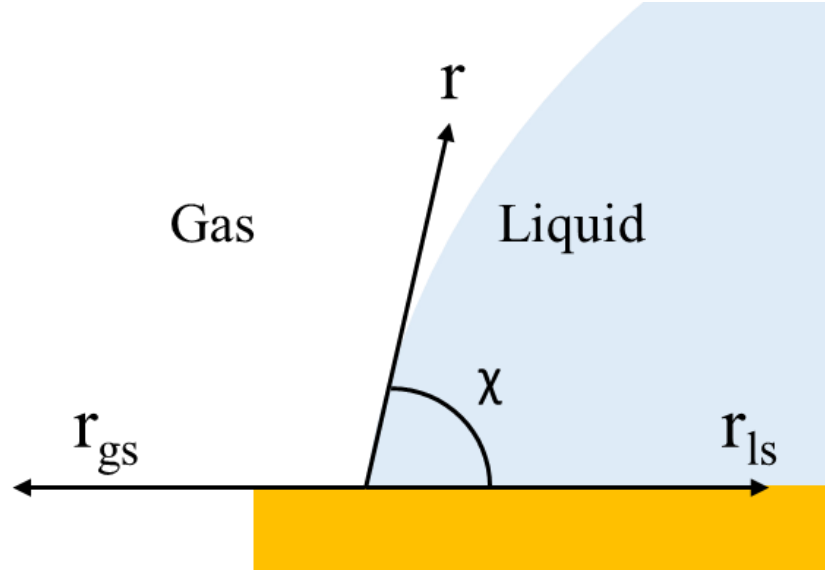


Figure 8: Schematic showing how the contact angle can be calculated from the interface between the solid, liquid, and gas regimes.

In practice however, a goniometer and its imaging software take a set of images and fits a set of lines using edge detection and linear least squares fitting to calculate the contact angle χ . [48]

2.2 Materials and Methods

2.2.1 Goniometer

All measurements were taken utilizing a Ramé-Hart 100-25-A goniometer, Figure 9. These goniometers operate via proprietary software that allows for the calculation of surface energy, surface tension, contact angle, etc. These systems can be used to observe changes of liquids when exposed to temperature, environment, as well as surface changes. The 100-25-A automatic tilt

goniometer for these studies allowed for automated tilt control, but required manual leveling and height adjustment. In order for the droplets or surfaces to be brought into view of the imaging camera, additions to the leveling base sometimes had to be added and releveled accordingly.



Figure 9: Goniometer from Ramé-Hart for use in the measurement of RTILs contact angle and surface tension.

2.2.2 Fluorinated RTILs

Fluorinated anions have been shown to be able to interact selectively with CO_2 . To this end, it was determined that 3 different types of fluorinated anions may be viable as CO_2 sensing material. RTILs come in a large selection of different anion and cation combinations that have been discussed previously in 1.3. Due to this ease of modification, three specific RTILs were selected

due to their ideal chemical and physical characteristics, in addition to their off the shelf purchase, for use in CO₂ sensor based research and development.

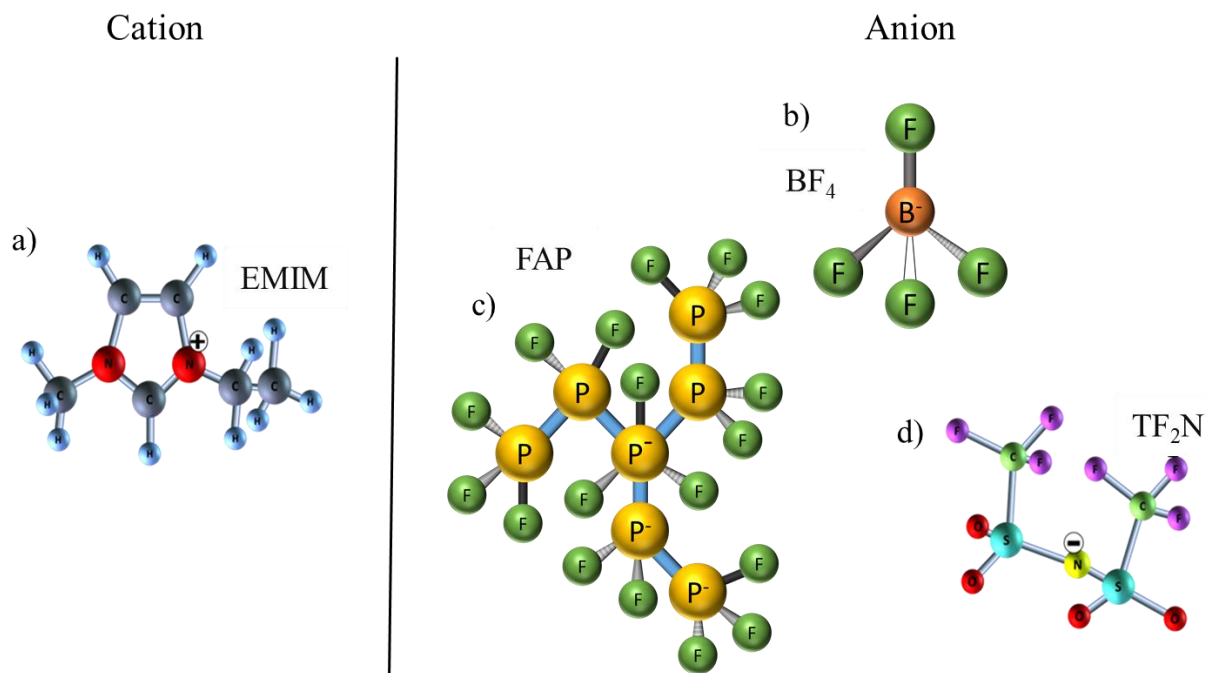


Figure 10: Schematics of the different components that make up the different RTILs investigated. a) EMIM cation, b) BF₄ anion, c) FAP anion, and d) TF₂N anion.

The cation 1-ethyl-3-methylimidazolium (EMIM) was chosen due to its unique viscosity and its minimal hydrophobicity properties. The anions tetrafluoroborate (BF₄), tris(perfluoroethyl)trifluorophosphate (FAP or FEP), and bis(trifluoromethylsulfonyl)-imide (TF₂N) were chosen due to their fluorination being a known interaction mechanism with CO₂ in addition to their known stabilizing properties with EMIM. This specificity of these RTILs is dictated by the ability of CO₂ to diffuse faster than other gases that may react with the RTIL under evaluation.

Table 4: Henry's constant for the selected RTILs for select gases.

RTIL/Gas	EMIM[BF ₄]	EMIM[TF ₂ N]	EMIM[FAP]
CO ₂	7.7	3.96	2.95

This is shown in Table 4 where the Henry's constant for CO₂ are shown at room temperature. The lower the Henry's constant via Henry's gas law means the higher the partial pressure or gas uptake is allowed by the liquid, Equation 22. [40,44,45]

$$H^{cp} = \frac{c_a}{p}$$

Equation 22

2.2.3 Electrode Design and Materials

Two forms of electrodes were explored. Both were of an interdigitated design, once consisted of a comb like interdigitated electrode, Figure 11. This design was chosen due to the ease of mask modification for larger or smaller electrode geometry. It was also suggested that a comb like geometry be utilized due to commonality with different sensing systems on the market that utilize IDE based designs.

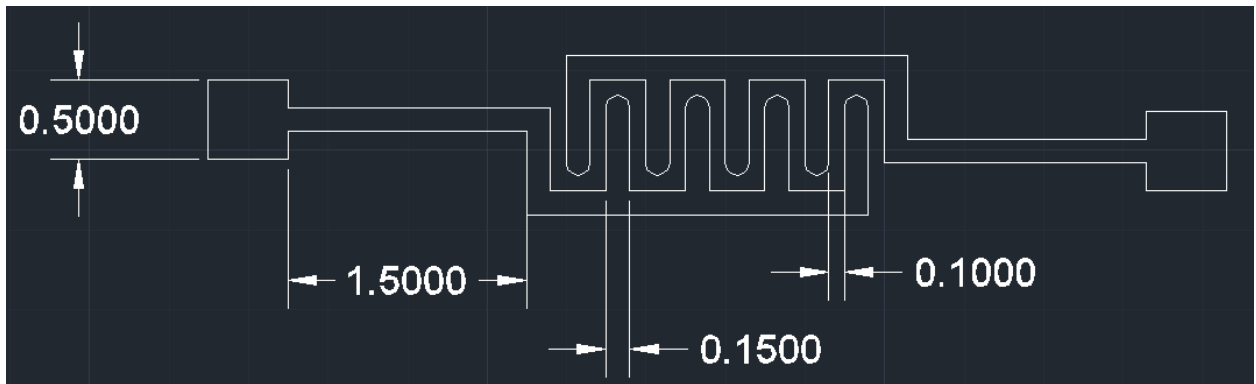


Figure 11: Schematic detailing layout of designed interdigitated electrodes.

These electrodes were initially deposited with gold on silicon and gold on glass, Figure 12 using standard metal/mask sputter deposition techniques. The main concern for this initial investigation was wettability of the surface with respect to the RTIL in addition to investigating some of the other physical parameters of these RTILs. Establishment of these parameters allows for develop for the next generation electrode designs.

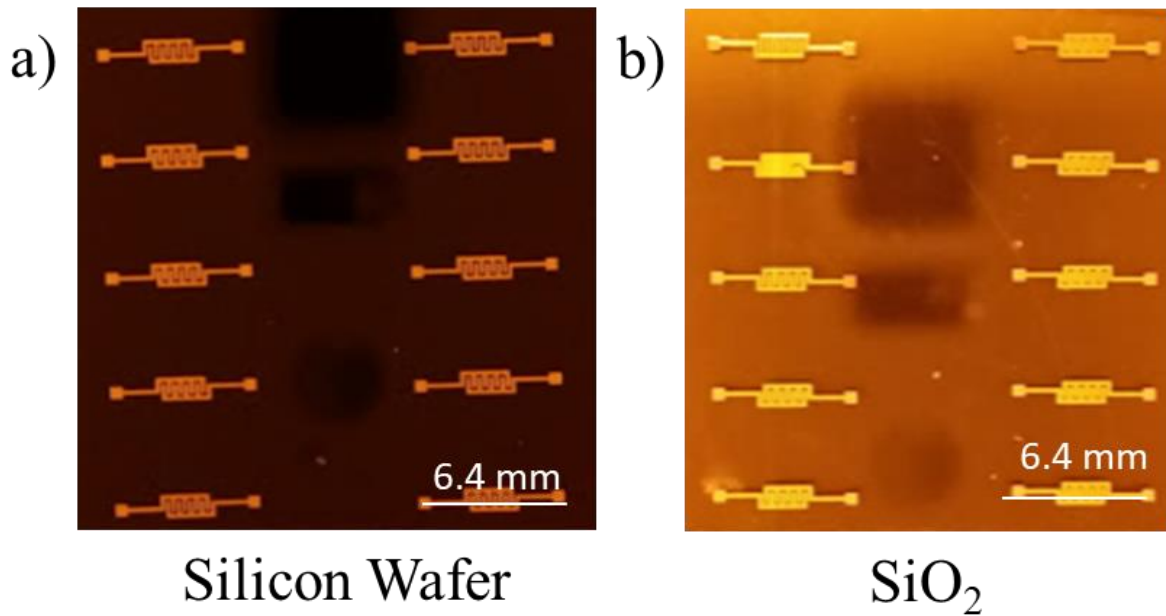


Figure 12: Microscope image of a) IDEs on standard 4 in. silicon wafer. b) IDEs on standard glass microscope slide.

The fabrication process for the silicon wafer deposited electrodes is outlined in Figure 13. The wafers were first cleaned to remove the outer most oxide layer on the backside of the silicon wafer, the wafer was then sputtered with chrome on the backside to a thickness of 300nm to provide a uniform surface for handling. The topside oxide was left to minimize response from the bulk silicon. A 2.5 μ m thick layer of S1813 was spin coated onto the wafer. A chrome mask was aligned

using a Karl Suss MA6 mask aligner and the photoresist exposed. The resist was developed and the patterned exposed, the wafer then had 200nm of chrome and 700 nm of gold deposited via Cryo e-beam evaporation. After deposition, the wafer was sent through a lift cycle to remove the developed resist. They were then cleaned with acetone, isopropyl alcohol, and N₂ dried.

The glass electrode system utilized microscope slides, and they followed a different process. They were first cleaned with acetone and attached to the wafer plate of the Cryo e-beam evaporator. A set of laser cut acetate films with the same pattern as the chrome mask were aligned on top of the class slides and attached with Kapton tape. The slides then had 200nm of chrome and 700nm of gold deposited. A diamond scribe was used to separate the individual sensors on both the silicon and glass substrates.

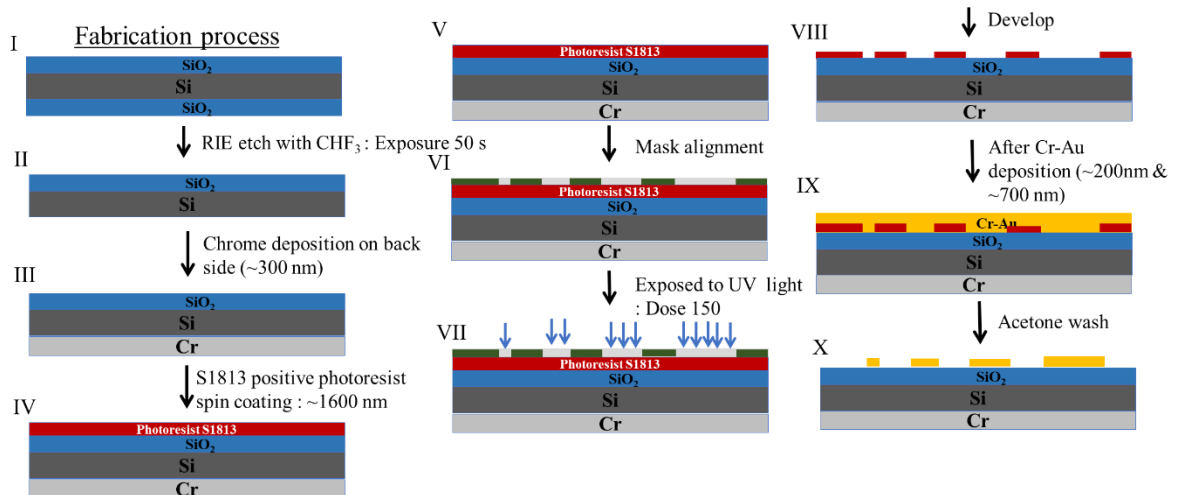


Figure 13: Fabrication process for 4-inch silicon wafers for the construction of gold IDE electrodes. The finished electrodes consisted of 200nm of Cr with 700nm of Au.

After the resist or masks have been removed, selected detectors are examined across the wafer to confirm that they electrodes have been deposited properly, Figure 14.

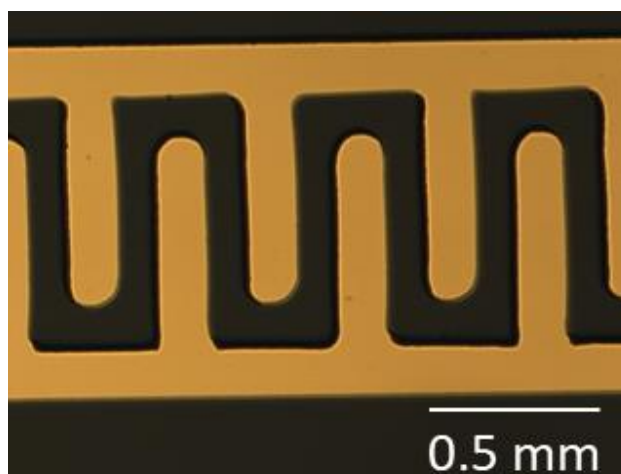


Figure 14: Microscopic image of gold electrodes to confirm lack of yield issues.

2.2.4 Experimental Procedure

A Ramé-Hart goniometer was used for all investigations of RTILs with respect to contact angle on both the carbon or gold IDEs. 5, 3, and 1 μL s of each of the RTILs were applied to the different electrode designs. Each volume measurement was taken in triplicate on Si-gold and glass-gold substrates. The substrate was first brought into view on the camera screen and leveled. A single droplet was deposited onto a clean are of the substrate. The alignment lines were arranged such that they horizontal line was at the interface between the RTIL and substrate and the vertical line was located at the midpoint of the droplet. Their contact angle for each of these volumes were measured 32 times on both the right and left angles at the electrode interface and then averaged together.

Surface tension was also measured utilizing the Ramé-Hart goniometer system as well. This was performed utilizing a 28-gauge flat end needle with a small volume of liquid. The RTIL was allowed to slowly form a drop such take maximum volume was reached before the weight of the droplet overcame the surface tension of the RTIL. A horizontal line was moved via the control

software such that it defined the edge of the needle. An image of the stable droplet was captured and the software calculated the experimental surface tension. This method was performed 32 times with each RTIL.

2.2.5 Results

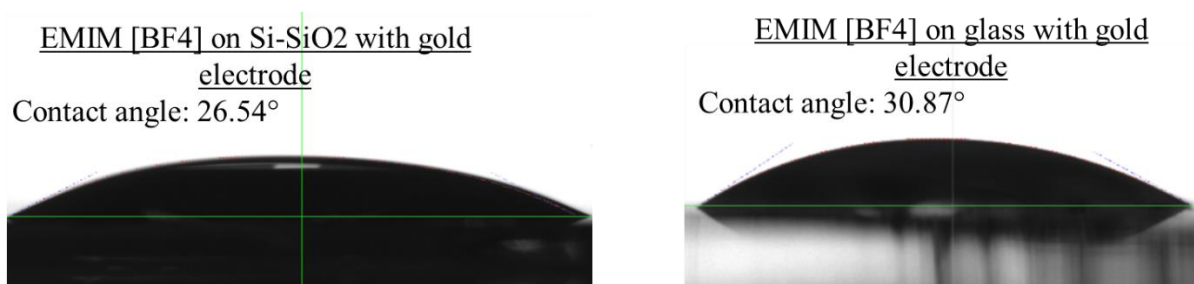


Figure 15: Contact angle calculation for EMIM[BF₄] on gold electrodes deposited on both silicon wafers (left) and glass microscope plates (right).

All three RTILs were tested for contact angle issues on both the Si-SiO₂ & SiO₂ substrates to determine if any major gold contact issues would be observed. For EMIM[BF₄], it is shown that on gold based electrodes on silicon, it has a contact angle of 26.54 \pm 0.05 $^{\circ}$ and for glass, a contact angle of 30.87 \pm 0.077 $^{\circ}$ as shown in Figure 15. The surface tension for EMIM[BF₄] was measured from the droplet in Figure 16 and found to be 39.51 \pm 1.93 dynes/cm shown in Table 5. The contact angles and surface tensions for EMIM[FAP] and EMIM[TF2N] are also summarized in Table 5.

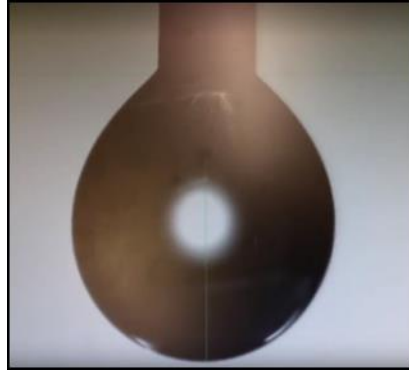


Figure 16: EMIM[BF₄] Pendant drop that was allowed to form on a 28 gauge flat nose needle for surface tension calculation.

Table 5: Summary table for contact angles of different RTILs on Si-SiO₂ gold and SiO₂ gold electrode surfaces made through standard metal deposition fabrication techniques.

RTIL	Contact angle		Standard deviation		Surface Tension (dynes/cm)	Standard deviation (dynes/cm)
	On Si-SiO ₂ wafer	On Gold electrodes	On Si-SiO ₂ wafer	On Gold electrodes		
EMIM[BF ₄]	30.8°	26.5°	0.077°	0.05°	39.51	1.93
EMIM[TFSI]	32.4°	31.9°	2.8°	1.76°	22.91	0.22
EMIM[FAP]	33.2°	36.1°	0.68°	2.8°	24.34	0.91

2.3 Discussion

The main concerns with this research was to confirm the wettability of gold with respect to RTILs and if the surface tension would be too high for use in different additive manufacturing techniques. As shown in Table 5, all three of the RTILs have been reported to have contact angles that are comparable to each other independent of the main substrate used. With respect to the gold, all the RTILs studied reported show excellent contact with the surface. As reported in literature, water normally has a contact angle of $< 10^\circ$ on clean gold surfaces, but on ordinary gold

surfaces have shown contact angles as high as 60 °. [46,47,48] These RTILs show acceptable contact angles less than 40 °, so they cover normal gold surfaces better than water in that regards. This points toward gold being an ideal substrate for testing these different RTILs when exposed to CO₂.

CHAPTER 3

ELECTROCHEMICAL BASIS AT ROOM TEMPERATURE

3.1 Aim: Exploring a new RTIL with respect to cycling for efforts towards CO₂ sensing in ideal conditions

Rising CO₂ gas levels have been shown to have adverse effects on both the environment and our own wellbeing in sufficiently high concentrations. Current monitoring devices utilize high temperature high power devices that do not allow for the further miniaturization for IOT based applications. Other solutions suffer from temperature restrictions or cross sensitivity issues. Room temperature ionic liquids (RTILs) are a form of liquid salt that can be tuned for optimal physical and chemical properties for gas sensing applications. In this work, two different electrode designs are explored and three fluorinated RTILs are subjected to different CO₂ exposures for understanding their electrochemical response via impedance spectroscopy. This effort is towards a large work that will deliver a low power IOT based CO₂ sensing mechanism. [49,50]

The main evaluation for this research is to better understand the electrochemical reactions that occur with these RTILs on carbon and gold electrodes, to determine if they provide the necessary leverage towards next generation low power CO₂ sensing, and the determination of next steps towards RTIL analysis and evaluation. To this end we present published results investigating the effects of electrode design and fluorinated RTILs in determining CO₂ concentration utilizing electrochemical impedance spectroscopy. Part of this work was completed and accepted for publication in IEEE Nanotechnology Transactions. It was titled “A Robust Electrochemical CO₂ Sensor Utilizing Room Temperature Ionic Liquids.” [54]

3.2 Cyclic Voltammetry

Cyclic Voltammetry is a form of potentiodynamic electrochemical study that utilizes a linear potential that ramps up and down with respect to time. The current for the system is recorded and is used to see how the behavior of the analyte varies over time and potential. This technique works best when working with a system that undergoes a redox reaction that results in some form of charge transfer. [51,52]

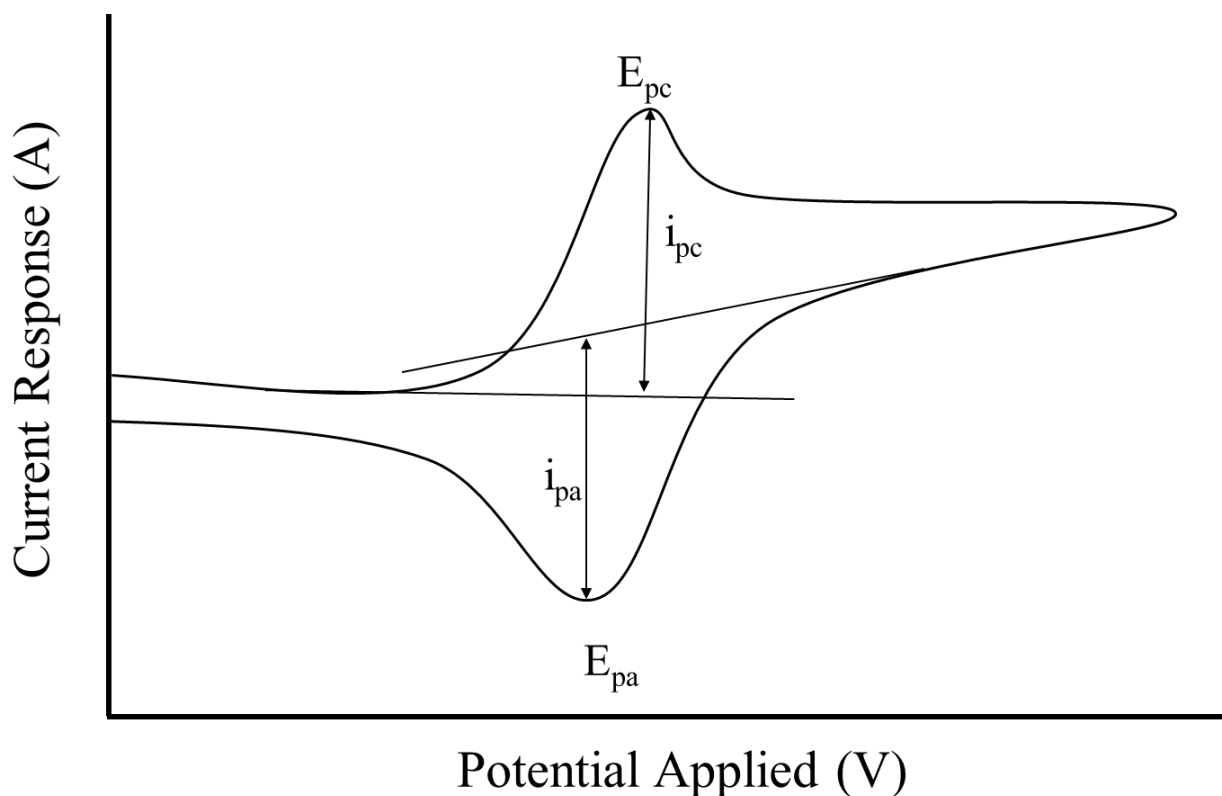


Figure 17: Generic cyclic voltammogram showing the oxidation and reoxidation behavior for an arbitrary system. i_{pa} and i_{pc} stand for the peak anodic and peak cathodic current respectively.

This technique also requires an understanding of material type selected as the working electrode due to it having an effect on the speed of electron transfer. When a sample is running, in the ideal case (i.e. reversible), the anodic and cathodic peak currents should be equivalent in magnitude. If,

however, the reactions taking place in the analyte are not completely reversible, the different amplitudes of peak current will be observed along with different current response curves. Through the cyclical nature of this voltage technique, exploring the diffusion limited reactions from the bulk to the EDL are possible. [26,30,44]

If we assume an ideal case for the redox reaction, we can utilize the Randles-Sevcik equation to derive interactions between a given RTIL and CO₂.

$$i_p = 0.4463nFAC \left(\frac{nFvD}{RT} \right)^{0.5}$$

Equation 23

From the Randles-Sevik: i_p is the max current, n is the number of electrons transferred, F is Faraday's constant, A is the area of the electrode, C is the concentration of the material, v is the scan rate of the voltage, D is the diffusion constant of the analyte, R is the Gas constant, and T is the temperature. [41]

3.3 Electrochemical Impedance Spectroscopy

Electrochemical Impedance Spectroscopy (EIS) is an electrical technique that is heavily used in the study of bimolecular systems. [41,51,52] This technique, also called dielectric spectroscopy, works by applying a sinusoidal voltage and monitoring the current response of the system. The excitations of these frequency based voltages are set to small amplitudes such that we can assume the response of the system behaves in a pseudo-linear way. [51,52] Starting with Ohm's Law.

$$R = \frac{V}{I}$$

Equation 24

From Equation 24 we note that with the application of an AC signal, phase effects may appear depending on the circuit that is being investigated, Equation 25.

$$Z = \frac{V(t)}{I(t)} = \frac{V_o}{I_o} \frac{\sin(2\pi ft)}{\sin(2\pi ft + \phi)}$$

Equation 25

The response of the system being investigated will show no frequency dependence if it is resistive in nature. However, if there are capacitive or inductive behavior present in the system, any application of a sinusoidal voltage will result in a phase shift occurring in the current response. The ratio between of the applied voltage and the system current gives the user insight into the impedance of the system. By utilizing Nyquist and Bode plots, Figure 18, one can determine the capacitive and resistive behavior of the sensor surface. [41,51]

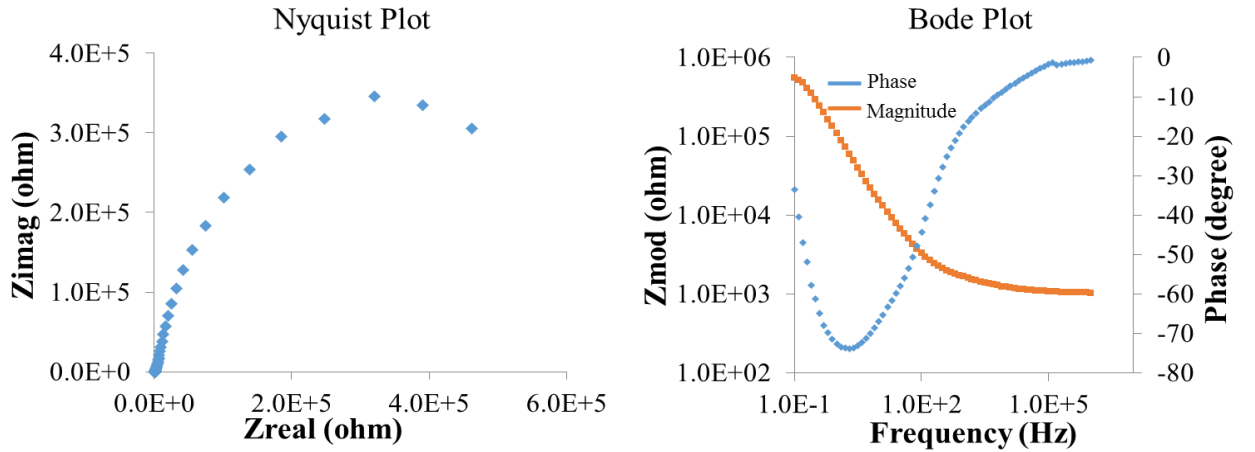


Figure 18: Bode Nyquist results of a detector coated in EMIM[BF4] in and N2 environment scanned at 3.5 V with a perturbation voltage of 0.1 V at 0.1 Hz to 200 kHz.

In the case of electrochemical systems, there is a standard equivalent circuit that can be used to fit data from the system. Called a Randles Circuit, Figure 19, this equivalent circuit allows for

bulk behavior, diffusion effects, and EDL effects to be extracted out utilizing 3rd party fitting software (ZView, Scribner Associates, Inc.).

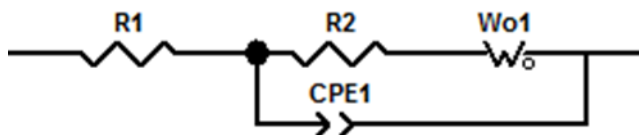


Figure 19: Equivalent Randles Circuit that allows for the investigation of different components of an electrochemical based system.

3.4 Methods & Materials

3.4.1 Capacitance of the electrochemical double layer

EDL capacitance changes can be measured by utilizing an equivalent circuit extraction process through the use of the ZView software from Scribner Associates, Inc. The process is not completely automatic and requires some initial conditions to be provided before an automated routine can be ran. From the raw data and literature studies, we determine what a close equivalent circuit is for our given system, Figure 19, and begin apply some of our initial conditions.

Element	Freedom	Value	Error	Error%
R1	\pm Free(\pm)	231.3	2.2514	0.97337
R2	\pm Free(\pm)	3.6977E6	5.5579E05	15.031
Wo1-R	\pm Free(\pm)	2.0563E7	3.0253E06	14.712
Wo1-T	\pm Free(\pm)	0.10701	0.043395	40.552
Wo1-P	\pm Free(\pm)	0.21161	0.0052639	2.4875
CPE1-T	\pm Free(\pm)	2.8646E-8	7.2069E-11	0.2431
CPE1-P	\pm Free(\pm)	0.97447	0.00024424	0.025064

Figure 20: Fitting parameters utilized to extract and differentiate between bulk and EDL effects.

For fitting to begin, empirically speaking, we set the bulk resistance, R_1 (R_s), of the system to 200Ω . From the raw data, Figure 21, we initially input the raw $\text{Mod}(Z)$ value as the R_2 (R_{ct}). CPE-T is set to initially to the maximum Z_{img} raw value. From observation, the Warburg value W_{o1-R} is usually set an order of magnitude higher than R_{ct} and allowed to be adjusted by the software. From these initial conditions, subtle tweaking of W_{o1-P} , W_{o1-T} , and CPE1-P are used for each iteration to minimize the overall error for each of the fitting parameters.

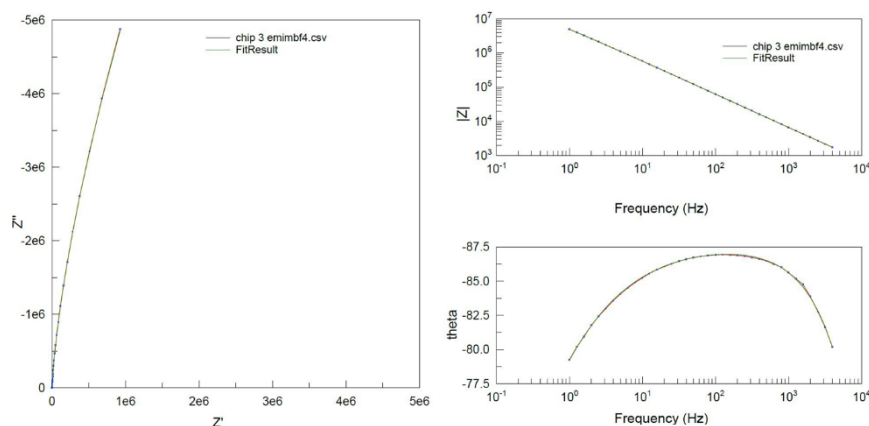


Figure 21: Fitted Nyquist and Bode plots with fitting lines created from the equivalent circuit and empirical data.

3.4.2 Experimental Apparatus and Environmental System

To properly control the levels of CO_2 that the different RTILs can be exposed to, some gas delivery system is necessary to allow for proper control of what the RTILs are exposed to for proper experimental analysis, Figure 22. The system used for these experiments utilized a dual chamber system. The primary chamber was an 850-LCM/SP from Pas-Labs, Inc nitrogen dry box used to isolate the secondary testing chamber from outside humidity and secondary gas sources. A Gamry Instruments, Inc. experiment box or a galvanized electrical box from Home Depot. These were used in conjunction with a Torrey Pines Scientific, Inc. HS60 digital hotplate for temp

control. The smaller boxes have had additional gas and electrical connections to provide the primary environment for us to test our RTIL response to CO₂ concentrations.

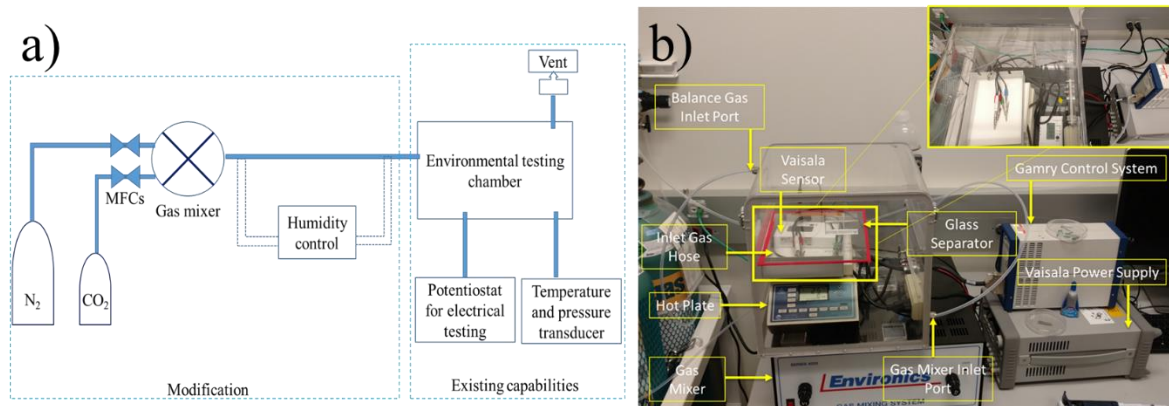


Figure 22: a) Initial layout and design schematic of environmental testing system. b) Final layout of testing system utilizing a dry box, potentiostat, gas mixer, hot plate, Vaisala sensor, and secondary testing box. The inset shows the secondary test box with input from the gas mixer and Vaisala for measurement of actual mixing output for offset adjustments.

Either premixed cylinders of 400ppm, 750ppm, or 1000ppm CO₂ concentrations or an Environics, Inc. 4000 series gas mixing system were utilized in order to deliver the different levels of CO₂ concentrations need for testing. The gas mixing system utilized a 5% CO₂ UPC grade cylinder combined with house N₂ at greater than 95% purity. Utilizing a Vaisala GMW95RD CO₂ monitor, the settings for the Environics are confirmed via the Vaisala which we use as our true measurement device.

3.4.3 Electrode designs

As shown in Figure 23, two different styles of electrode designs were used for this research. For consistency and high-quality control, an order for carbon based circular IDE and gold based linear IDE sensors were both purchased from PCB Universe, Inc. These consisted of insulated

copper lines with carbon-plated and or gold-plated electrodes on one end and through hole gold coated solder pads at the other end of the lines. These were all supported and insulated with FR-5 glass epoxy. These two materials were chosen due to literature review showing that RTILs can be enhanced by the presence of carbon as an electrode surface. [32,48] It has been shown by Yu et. al. that when BMIM[PF₆], a larger analog to EMIM[BF₄], is deposited with pasted carbon electrodes that the overall charge transfer rate of the system increases significantly than with just the carbon electrodes themselves. This is thought to be due to the RTIL depositing itself inside the interstitial layers of the carbon electrodes. [48] To this end, it was hypothesized that the carbon electrodes may increase the sensitivity of the RTIL to CO₂ via an enhanced charge transfer mechanism.



Figure 23: Carbon pasted IDE from PCBUniverse, Inc. (left). Gold IDE with RTIL deposited from PCBUniverse (right).

3.5 Experimental Procedure

The process for these experiments utilize a similar process for each of the RTILs tested as well as for each of the electrode investigated. The electrodes were first soldered to two 24 gauge wires for easier interfacing with the Gamry connection wires. They were then cleaned using a Chem-

wipe Kimwipe soaked with acetone, followed by a Kimwipe soaked in isopropyl alcohol, and then dried using house dry N₂. The electrodes were coated with 5 μ L of either EMIM[BF₄], EMIM[TF₂N], or EMIM[FAP]. These devices were then placed inside the secondary environment chamber and baked for 90 minutes at 155 °C in a pure dry N₂ environment. They were then allowed to cool to room temperature in this environment. For baseline measurements, the Gamry Reference 600 Potentiostat was allowed to stabilize for 15mins with the detector attached in a powered-on state. EIS was performed in triplicate in an N₂ environment before dosing the detector with CO₂. The house N₂ flow was shut off and the CO₂ concentration being tested was allowed to flow into the smaller test chamber for 10 minutes to ensure a uniform environment for testing. EIS was then performed in triplicate to investigate the changes in charging dynamics of the EDL. The EIS settings consisted of a 3.5 V DC bias with a 100 mV AC voltage. This AC voltage was swept from 1 Hz up to 10k Hz for all of the RTILs under investigation. For the chronoamperometry experiments, only EMIM[BF₄] and EMIM[FAP] were explored and the voltage settings for these experiments were swept from -2.5 V to 3.5 V at a rate of 500 mV/sec.

3.6 Results & Discussion

3.6.1 Cyclic Voltammetry Analysis

Cyclic voltammetry was used initially to investigate the possible differentiation and electrochemical response to EMIM[BF₄] and EMIM[FAP] with respect to different concentrations of CO₂. Understanding the charge transfer mechanism was of these RTILs was important in attempting to determine the rate of diffusion of these materials. Figure 24 shows 4 voltammograms of EMIM[BF₄] detectors that are scanned at a rate of 500 mV/s at N₂ baseline, 400ppm, 750ppm,

and 1000ppm respectively. Figure 25 is a set of voltammograms showing the CO₂ response of EMIM[FAP] at different CO₂ concentrations as well. From both of these figures, we can now investigate what type of charge characteristics each of these RTILs offer. These initial efforts were to determine how reversible the reactions with CO₂ were in efforts to determine next steps for sensor development testing.

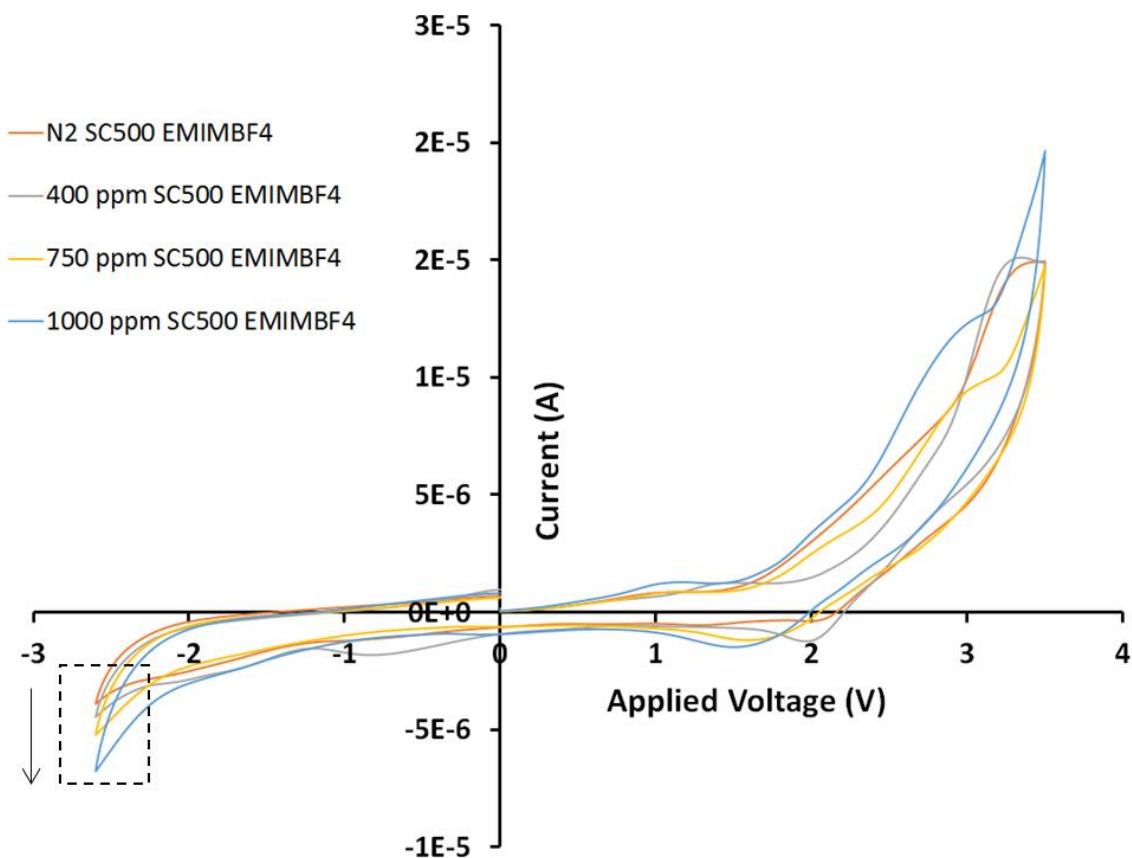


Figure 24: Cyclic Voltammogram (CV) for EMIM[BF₄]. The applied voltage was swept at a rate of 500 mV/s from -2.5 V to 3.5 V. For each concentration of CO₂, 400, 750, and 100ppm respectively, were compared.

As can be shown from Figure 24 and Figure 25, the anodic side of the CVs with increased concentration of the CO₂ that both EMIM[BF₄] and EMIM[FAP] are exposed to, shows a slight reduction in the electrochemical window of the RTIL under test. What is of interest is that for

EMIM[BF₄], the change from N₂ to 1000ppm is 30mV to the right with no clear anodic peak (*i*_{pa}). An increase in the tail is observed of the CV such that it shows a 30 mV shift to the right and the peak current goes from 4 μ A in N₂ to 6.8 μ A. The cathodic peak current (*i*_{pc}) is observed for EMIM[BF₄] and goes from 20 μ A in N₂ and 400ppm to 10 μ A at 750ppm then up to 16 μ A at 1000ppm.

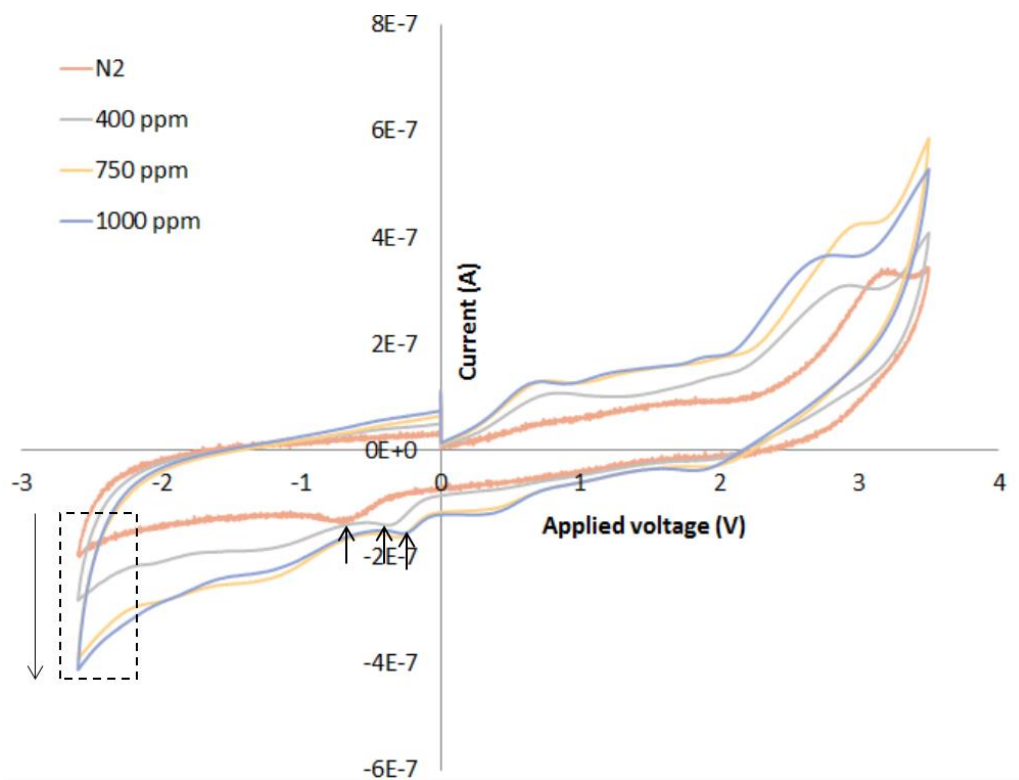


Figure 25: Cyclic voltammogram for EMIM[FAP] with a voltage sweep at 500 mV/s from -2.5V to 3.5V. Each CV is the average of 3 cycles at the different CO₂ concentrations of 400, 750, and 1000 ppm.

The cathodic side of the voltammograms show a slight redox peak at ~3V for EMIM[BF₄] and 2.8V for EMIM[FAP]. There is an anodic peak for EMIM[FAP] as well, but it shifts strongly to the right with the introduction of CO₂. Originally centered at 0.72V at a *i*_{pa} of -0.13 μ A in N₂, we see a shift to the right of 0.26V with a peak anodic current of -0.16 μ A. For *i*_{ac} in Figure 25 we also

see an oscillating behavior for the cathodic current similar to that with EMIM[BF₄] though we see 0.34 μ A at N₂, 0.33 μ A at 400ppm, 0.41 μ A at 750ppm, and 0.37 μ A at 1000ppm CO₂ respectively.

From these CVs, it is shown that when CO₂ is added to the system a reduction of the overall electrochemical window of the material is observed due to the redox (i_{ac}) current shifting left of right with respect to the concentration of CO₂. It has been observed in the literature that the electrochemical window of different RTILs can be reduced due to the introduction of different materials to the system that they are sensitive. The specific responses that we have observed show that redox behavior is dependent on the concentration of CO₂ present at minimal loss in reduction of the overall electrochemical behavior of the RTIL and it is differentiable we respect to the CO₂ concentration. In the case of EMIM[FAP] there is also a minor oxidation peak that is also responsive to CO₂ concentration. These results show that fluorinated RTILs are suitable in terms of stability and sensitivity for further CO₂ detection analysis.

3.6.2 EIS Evaluation of Carbon and Gold based electrodes with RTILs

For Figure 26, we see the EIS results for 5 μ L of EMIM[BF₄], EMIM[TF₂N] and EMIM[FAP] across three carbon paste electrode based detectors in an N₂ environment. With a constant DC bias of 3.5V with an AC voltage of 100mV, they were scanned across a range of frequencies from 1 Hz to 10kHz. This work was in efforts to determine at what set of frequencies would maximum EDL capacitance (ideally -90°) of the system would occur. For EMIM[BF₄] we show a maximum capacitance response at <100 Hz across 3 different devices. EMIM[TF₂N] and EMIM[FAP] both also show max capacitance at <100 Hz. Overall, the CPE based electrode results show that regardless of RTIL used, they still show remarkable similarity to each other in a nonreactive environment and show a similar logarithmic response in their impedance across frequencies.

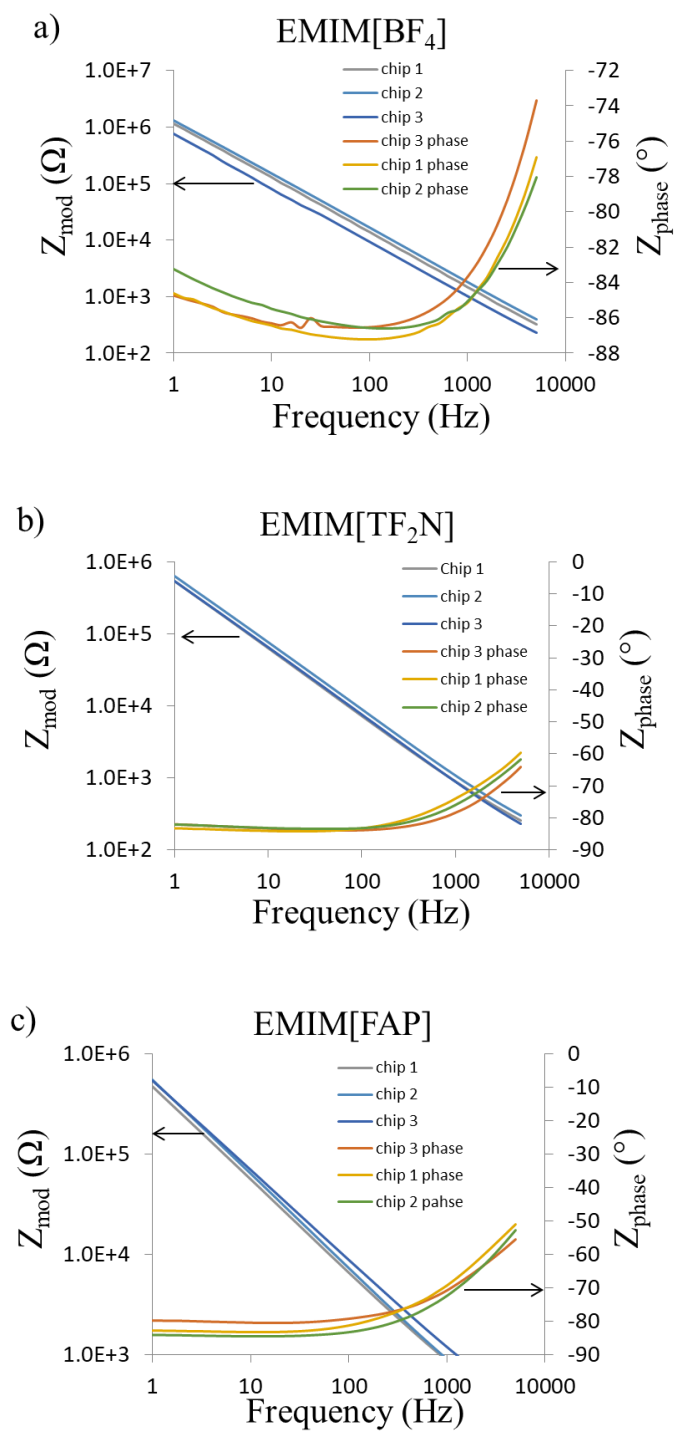


Figure 26: Impedance and phase dependence on frequency with a) EMIM[BF₄], b) EMIM[TF₂N], and c) EMIM[FAP] on IDE carbon Paste electrodes.

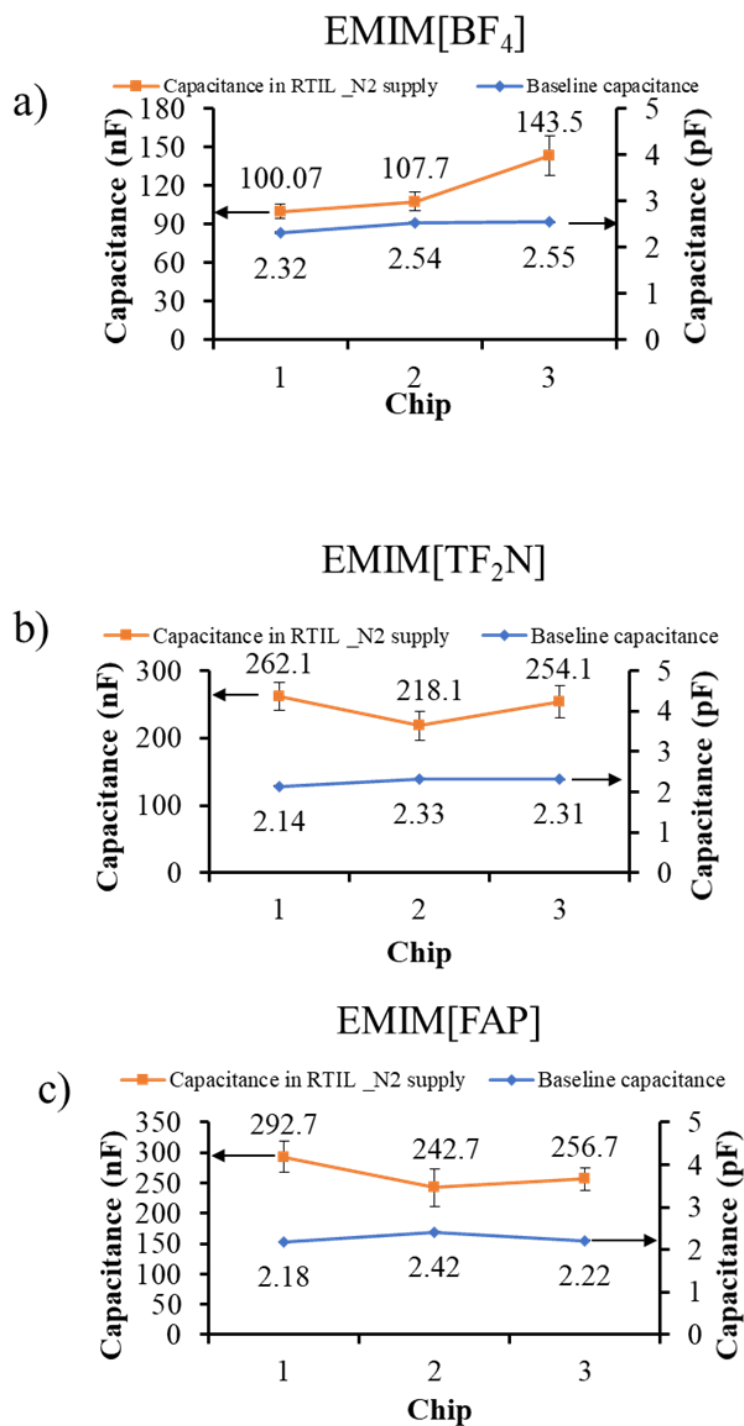


Figure 27: Extracted capacitance response with a) EMIM[BF₄], b) EMIM[TF₂N], and c) EMIM[FAP] on IDE carbon Paste electrodes with and without the RTILs present on the electrodes.

Understanding how the CPE based systems work when compared to their open circuit potential (i.e. baseline) behavior is useful in determining what, if any interactions are occurring with only the RTIL and electrode interface, Figure 27. What we see is that open circuit wise, the detectors behave similarly which is to be expected from a 3rd party supplier. On average, the baseline capacitance is 2.34 pF as summarized in Table 6. Where we do see the change is with the addition of any of the RTILs. From just the addition of the different RTILs, we see an increase in extracted capacitance of 1000 pF. In the case of EMIM[TF2N] and EMIM[FAP] a factor of over 2000 pF. This change in response is solely due to the presence of the RTIL and the strong EDL that is forming at the detector interface. A drawback of note is that on these CPE detectors, we see a significant increase in the run to run variance of these detectors. In the case of EMIM[BF₄] as much as 16%.

Table 6: Extracted capacitance values comparing open circuit capacitance without RTILs to the capacitance in N2 with the RTIL present.

RTIL on CPEs	Average	St. Dev.	% St. Dev
Open Circuit (pF)	2.47	0.11	4.3
EMIM[BF ₄] (nF)	117.1	18.9	16.1
Open Circuit (pF)	2.3	0.1	4.6
EMIM[TF ₂ N] (nF)	264.1	21.1	7.9
Open Circuit (pF)	2.26	0.08	3.77
EMIM[FAP] (nF)	244.7	19.1	7.8

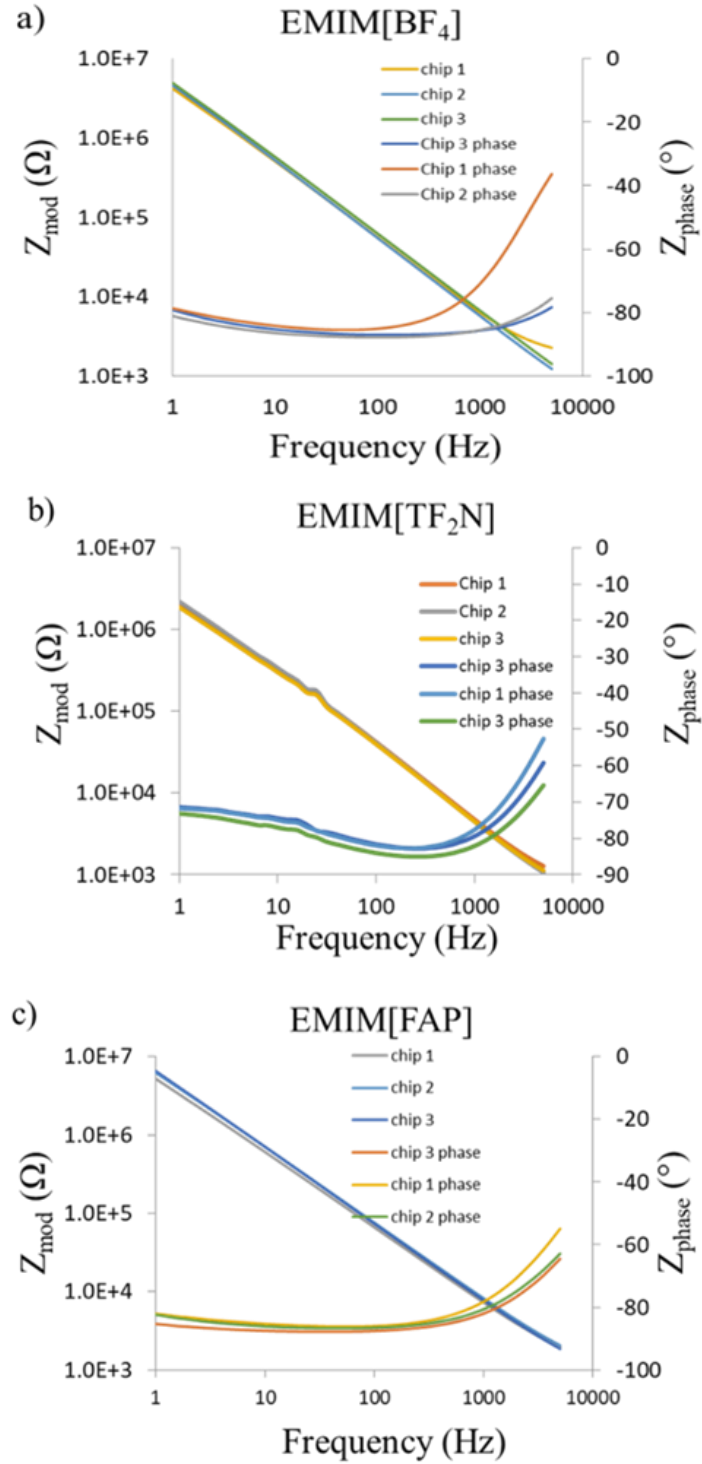


Figure 28: Impedance and phase dependence on frequency with a) EMIM[BF₄], b) EMIM[TF₂N], and c) EMIM[FAP] on gold IDEs.

Gold based IDE sensors were also explored as a possible sensing platform due to gold's intrinsic characteristic to be nonreactive with most chemicals excluding Aqua Regia. From the initial EIS results, all RTILs show variance on where their frequency of maximum capacitance is located.

For EMIM, Figure 28 a), we see a maximum capacitance around 100 Hz. The behavior of chip 1 in Figure 28 a) is thought to be caused from a bad solder joint which would result in higher frequency noise. EMIM[TF₂N] in Figure 28 b) shows a capacitance maximum around 520 Hz. EMIM[FAP], Figure 28 c) shows a capacitance maximum at approximately 84 Hz.

The extracted capacitances with respect to baseline are shown in Figure 29. The baseline capacitance of the gold IDEs are, on average, 1 pF. This shows that there is great consistency between the individual detectors with the baseline behavior mostly effected due to the wire soldering process done within the lab. With the addition of the RTIL, we see a large shift in the capacitance that is only due to the formation of the EDL on the electrode surface. For EMIM[BF₄] in Figure 29 a), the average capacitance in N₂ is 30.8 nF with a % std error of 5.5%. EMIM[TF₂N] also shows a large increase in capacitance as well, Figure 29 b), with a 56.8 nF response in N₂ with an % std error of 5.4%. Figure 29 c) shows the shift from baseline capacitance with the addition of EMIM[FAP]. The extracted capacitance for EMIM[FAP] comes to an average of 24.5 nF with a % std error of 7.7%. A summary of these RTILs on gold electrodes can be found in Table 7.

The two electrode designs were compared by evaluation the C_{DL} response of the RTILs EMIM[BF₄] and EMIM[TF₂N]. The devices measurements were carried out inside a nitrogen environment to eliminate the exposure to CO₂. The interface stability between the RTIL and electrode directly effects to formation and capacitance response of the electrical double layer.

From these initial results, the CPE based electrodes offer at significantly higher capacitive baseline when the RTILs are added, ~200 nF. The down side to the RTIL/electrode interaction is significant higher standard deviation, in the case of EMIM[BF₄] the deviation is 16.1% over 3 cycles and 3 different chips. EMIM[TF₂N] and EMIM[FAP] also have large standard deviations on the order of 7%. When we compare the behavior of these CPE based sensors to the RTILs on gold, we see that the overall initial capacitance is an order of magnitude lower, but the standard deviation of the sensors is also smaller in general, though EMIM[FAP] still shows a % standard deviation around 7%. Overall to move forward on the development of a new CO₂ sensor, gold electrodes show the most promise in terms of consistency and, from literature review, low to nonexistent reaction with the RTILs. Due to the elevated variance on the carbon electrodes, the gold electrodes were chosen for further experimental analysis with CO₂ in efforts to reduce base line variance in the C_{DL} values for the RTILs under investigation.

Table 7: Extracted capacitance values comparing RTIL in N₂ vs open circuit capacitance of the gold electrode without RTIL present.

RTIL on Au IDEs	Average	St. Dev.	% St. Dev
Open Circuit (pF)	1.07	0.11	10.2
EMIM[BF ₄] (nF)	30.8	1.7	5.5
Open Circuit (pF)	1.04	0.14	13.3
EMIM[TF ₂ N] (nF)	56.8	3.1	5.4
Open Circuit (pF)	0.87	0.10	10.7
EMIM[FAP] (nF)	24.5	1.9	7.7

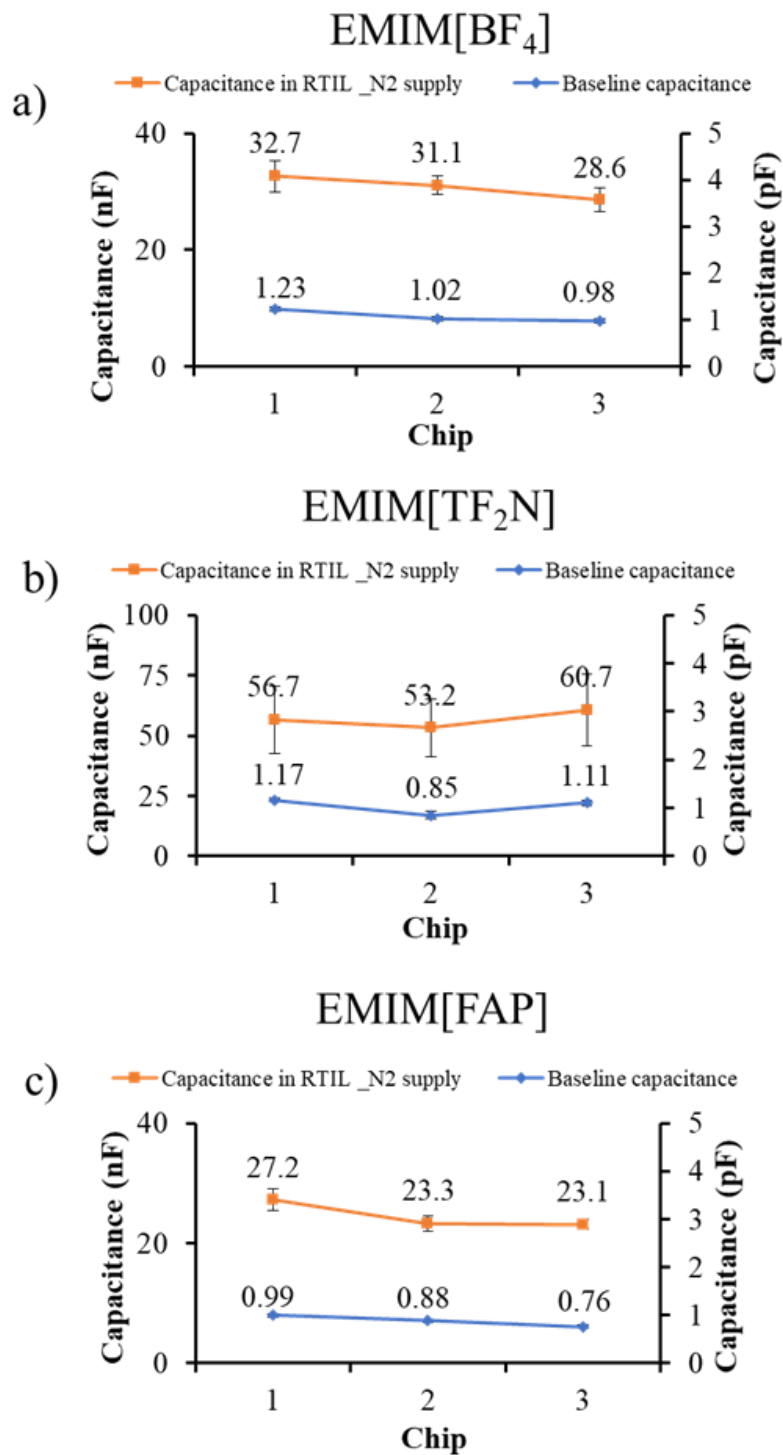


Figure 29: Extracted capacitance response with a) EMIM[BF₄], b) EMIM[TF₂N], and c) EMIM[FAP] on gold IDEs with (left axis) and without (right axis) RTILs present.

3.6.3 CO₂ Response on linear Au-IDEs

Now that the behavior of the different electrodes has been characterized, it was determined that the gold linear IDE electrodes would provide the best opportunity towards continued development of a low power CO₂ sensor. This section will highlight the response of EMIM[BF₄], EMIM[TF₂N], and EMIM[FAP] to concentrations of CO₂ at 400ppm, 750ppm, and 1000ppm using EIS using a process explained previously in the Experimental Procedure located on page 38. Through the investigation of their initial exposure behavior, it is possible to determine effectivity of different RTILs in measuring CO₂ changes in an environment.

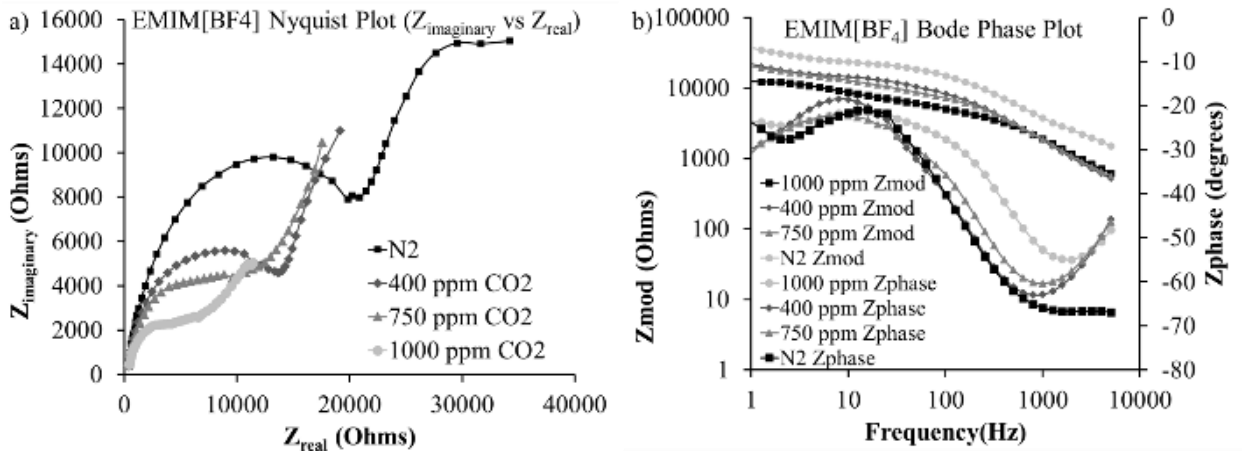


Figure 30: a) Nyquist plot showing the behavior of EMIM[BF₄] when exposed to N₂ baseline to 1000ppm CO₂. b) Bode plots for N₂ up to 1000ppm CO₂ exposure. c) Extracted resistance change from the detectors tested with EMIM[BF₄]. Adapted from “A Robust Electrochemical CO₂ Sensor Utilizing Room Temperature Ionic Liquids,” by E. Graef, R. Munje, and S. Prasad, 2017, IEEE Nanotechnology Transactions, Vol. 16, No. 5, pg. 828-829.

From the initial work in the electrode analysis, it was shown that with the addition of EMIM[BF₄] it was shown that a significant capacitance behavior with gold electrodes in N₂. With

the addition of CO₂ to the environment, we see significant changes to the impedance response. Figure 30 a) shows that the charge transfer resistance decreases as the CO₂ concentration is increased from 0 ppm up 1000 ppm. This implies that as the CO₂ concentration is increased, the interaction mechanism of EMIM[BF₄] causes a reduction in the bulk (R_{CT}) response. From the Bode magnitude plots shown in Figure 30 b) the total impedance response (Z_{MOD}) decreases as there is an increase in CO₂ concentration. The ratio of capacitance change (C_{CO_2}/C_{N_2}) is shown in Table 8 and changes by over 2x of the baseline N₂ capacitance.

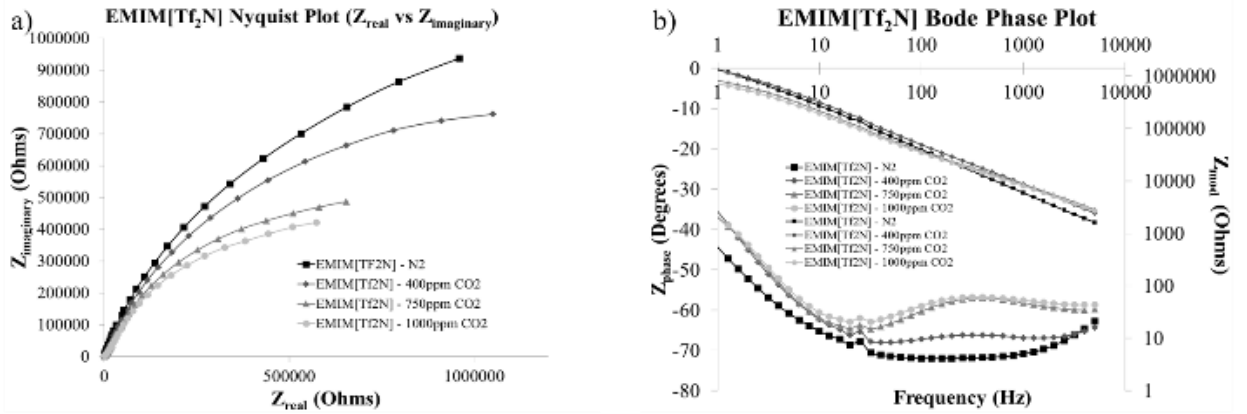


Figure 31: a) Nyquist plot showing the behavior of EMIM[TF₂N] when exposed to N₂ baseline to 1000ppm CO₂. b) Bode plots for N₂ up to 1000ppm CO₂ exposure. c) Extracted resistance change from the detectors tested with EMIM[TF₂N]. d) Extracted capacitance change of EMIM[TF₂N] after exposure to different concentrations of CO₂. Adapted from “A Robust Electrochemical CO₂ Sensor Utilizing Room Temperature Ionic Liquids,” by E. Graef, R. Munje, and S. Prasad, 2017, IEEE Nanotechnology Transactions, Vol. 16, No. 5, pg. 829-830.

EMIM[TF₂N] was investigated for CO₂ responses as well, Figure 31. The real and imaginary components of the impedance response were recorded as the CO₂ concentration changes. From Figure 31 a), the capacitive behavior dominates the system. This is shown as the reduction of the semicircular region of Figure 31 a), the charge transfer resistance decreases inversely with the

concentration of CO₂. Figure 31 b) shows the Bode plot and how there is a highly capacitive response due to the phase angle increasing from 50° to 80°s across the frequency sweep. The summary of the average extracted is showed in Table 8 and it shows a significant capacitance change at over 2.5x of the N₂ signal.

Table 8: Extracted capacitance ratio response of the 3 RTILs being investigated investigated.

RTIL/Ratio CO₂/N₂)	EMIM[BF₄]	EMIM[TF₂N]	EMIM[FAP]
400 ppm	1.00	1.10	1.00
750 ppm	1.47	1.63	1.01
1000 ppm	2.12	2.52	1.04

EMIM[FAP] Nyquist responses are shown in Figure 32. The real and imaginary components show, again, that the capacitive response of the system dominates. There is a variation between the detectors ran in terms of over Z_{mod} , but as shown in Figure 33, the phase change does not shift significantly. This also confirmed by the extracted capacitance ratios shown in Table 8.

From these results, we can begin comparing the behavior of these different RTIL based systems. EMIM[TF₂N] appears to be best when we compare the extracted CO₂ ratios to that of the other two RTILs. Though EMIM[BF₄] also shows potential as a highly capacitive system as well. EMIM[FAP] shows the lowest capacitive ratios. This caused a reanalysis of the data in terms of charge per unit area shown in Table 8.

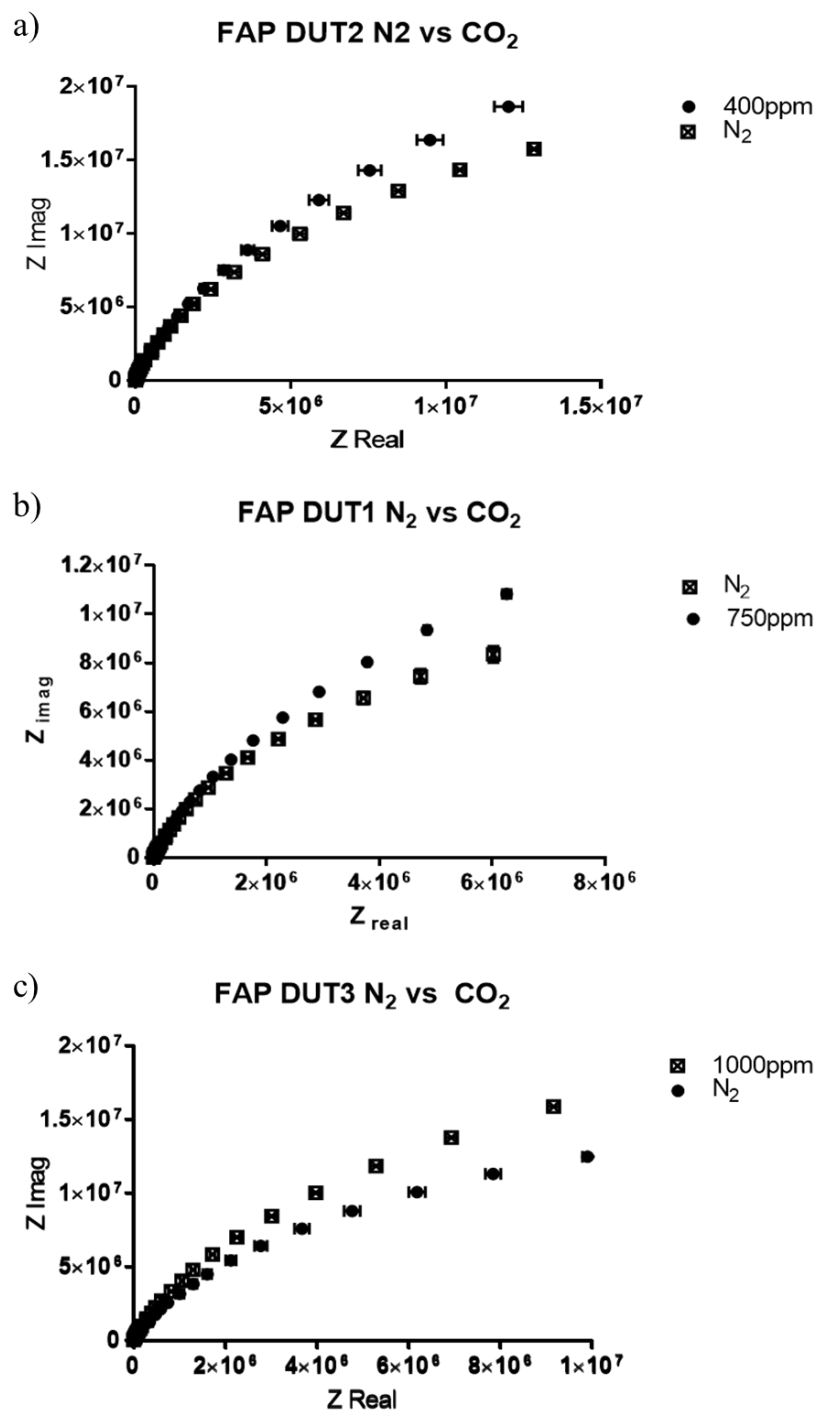


Figure 32: Nyquist plot of EMIM[FAP] when exposed to different levels of CO₂ concentration. a) 400ppm, b) 750ppm, and c) 1000ppm.

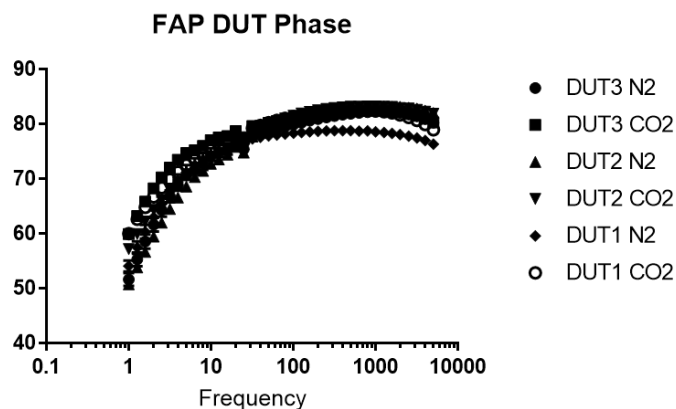


Figure 33: Phase response of EMIM[FAP] over different CO₂ concentrations from 400ppm to 1000ppm compared to their N₂ baseline phase response.

3.7 Conclusion

From these initial studies, we evaluated the effectivity of different electrode designs on a subset of RTILs towards future efforts of CO₂ sensing. The behavior of the CPE based circular electrodes showed larger baseline open circuit capacitance as well as significantly larger N₂ capacitance response with RTILs present than found on the linear gold IDEs. However, the noise behavior was more favorable using the gold IDEs. It was also shown in later literature reviews that the carbon-based electrodes may cause chemical interactions with different RTILs that could not be easily controlled. [53,54] Moving forward to the actual CO₂ testing on gold IDEs, it was shown that all showed a reduction in the overall semicircular behavior of the Nyquist impedance plots. This tracks with a decrease in the charge transfer resistance in the materials. EMIM[FT₂N] showed the best capacitive response to the CO₂ changes followed by EMIM[BF₄] then EMIM[FAP]. Through this analysis it was determined that temperature and humidity responses would now need to be explored for these materials in the next steps towards the development of a low power CO₂ sensor. [54]

CHAPTER 4

RTILs AT ELEVATED TEMPERATURE AND HUMIDITY

4.1 Aim: Temperature and Humidity studies towards development of a portable low powered sensor.

It has been shown previously that select RTILs have a sensitivity to detecting different concentrations of CO₂. In efforts towards that, understanding the effects of temperature and humidity on different RTILs is necessary for continued work toward a low power CO₂ gas sensor. Towards that effort, initial results are presented in this chapter showing how different RTILs react to temperature and humidity effects as well as preliminary results of a portable sensing system detecting changes in CO₂ in controlled conditions. [40,44,50,55]

EMIM[FAP] & EMIM[TF₂N] have been selected for this work due to a literature review showing that EMIM[BF₄] is soluble in high humidity (water) environments. [26,50,55] It has been shown in Holbrey & Seddon (1999) that EMIM[BF₄] is capable of adsorbing significant quantities of water. [26] This strongly effects both its chemical and physical properties, so in terms of actual real-world sensor development, it was determined that EMIM[FAP] and EMIM[TF₂N] have the better chance as actual sensor systems due to their hydrophobic properties.

4.2 Experimental Procedure and Setup

Using the same gas system and electronics previously detailed in Chapter 3, it was determined that the DC bias of 3.5 V used for the initial evaluations exceeded the electrochemical windows except for EMIM[BF₄]. There were also concerns about the large capacitance changes we observed and interest in moving towards a lower voltage based on electronic standards. To that

end, 1.7 V was chosen as the new DC offset while maintaining a 100mV oscillatory current from 1 Hz to 10 kHz.

Two sets of experiments were performed for this study. The first dealt only with the increase of temperature to determine if these materials were capable of sensing CO₂ at room temperature (25°C) as well as the elevated temperatures of 45°C, or 65°C. The second set of experiments involved controlling the humidity provided. These humidity values were set at 25%, 45%, and 65% respectively while the temperature ranges consisted of 25°C, 45°C, or 65°C.

For the temperature experiments, 1 μ L of a given RTIL was deposited onto a soldered gold IDE that had been cleaned using an acetone, isopropyl alcohol, N₂ dry process. The sensors were then baked out in a 0% relative humidity (%RH) N₂ environment at 155°C for 90 minutes before being allowed to stabilize at the appropriate testing temperature (25°C, 45°C, or 65°C). This environment setting was allowed to stabilize for 10 minutes before baseline impedance measurements were taken in triplicate for 3 different detectors. The CO₂ concentration for the given test was then turned on. This environment setting was allowed to stabilize for 10 minutes before the dosed impedance measurements were taken in triplicate for 3 different detectors.

For the humidity based measurements, the 1 μ L RTIL detectors were again baked out at 155°C in a dry (0%RH) environment for 90min. The temperature was then allowed to equilibrate to the necessary test temperature. At this point, the dry N₂ was then turned off while allowing humidified N₂ gas from the Environics gas mixing system to enter the secondary test chamber. This environment setting was also allowed to stabilize for 10 minutes before baseline impedance measurements were taken in triplicate for 3 different detectors. After this, the CO₂ concentration

was changed to one of the 3 being monitored and allowed to equilibrate with for 10 minutes. At this point, the dosed impedance measurements were taken in triplicate for the 3 different detectors.

4.3 Temperature Results

Literature has supported that RTILs lose their capture ability as their overall temperature increases. This is one of the reasons why we use 155 °C as our bake out temperature. Providing a temperature above 100 °C guarantees that any initial contaminants, CO₂, H₂O, etc., have been removed. What was of initial concern was whether detection of CO₂ concentration was possible at an elevated temperature in efforts toward industrial or automotive applications. To that end, the extracted results of these tests are presented in Table 9 and Table 10.

Table 9: Extracted resistance and capacitance values of EMIM[TF₂N] across 25, 45, and 65°C.

RTIL Under Test EMIM[TF ₂ N] 1 μ L Samples											
Test Temperature 25°C				Test Temperature 45°C				Test Temperature 65°C			
Gas Type	R _{ct} (Ω)	C _{dl} (nF)	Δ C (nF)	Gas Type	R _{ct} (Ω)	C _{dl} (nF)	Δ C (nF)	Gas Type	R _{ct} (Ω)	C _{dl} (nF)	Δ C (nF)
N2	3.00E+06	35.40	7.1	N2	7.00E+06	24.2	4.4	N2	6.00E+06	32.8	4
400ppm	3.00E+06	28.30		400ppm	7.00E+06	19.8		400ppm	6.00E+06	28.8	
N2	2.80E+06	54.9	10.9	N2	8.00E+06	16	2.6	N2	8.20E+06	17.1	3.4
750ppm	2.80E+06	44.00		750ppm	8.00E+06	13.4		750ppm	8.20E+06	13.7	
N2	2.20E+06	60.50	18.3	N2	8.00E+06	17	0.1	N2	7.80E+06	17.4	0.9
1000ppm	2.20E+06	42.20		1000ppm	8.00E+06	16.9		1000ppm	7.60E+06	16.5	

From Table 9, we see that EMIM[TF₂N], overall, is still able to differentiate between different concentrations of CO₂ not only at room temperature, but also up to 65 °C. What is seen for all three of the different experiments is that as the temperature increases, the overall capacitive response changes. At room temperature we see similar behavior shown in the previous chapter

such that the capacitance change follows with CO₂ concentration while the overall charge transfer resistance decreases, though at 400ppm, there is no real observable change, so 400ppm may be considered a threshold value in this case. At the actual elevated temperatures EMIM[TF₂N] showed a downward trend in capacitance change as the CO₂ concentration is increased while the R_{ct} remained mostly unchanged. While not conclusive, what this is showing is that at elevated temperatures there is a significantly weaker physisorption interaction coming into play than at lower temperatures. This implies that as the temperature of operation is increased in a dry environment, a decrease in the upper detection threshold may occur.

Table 10: Extracted capacitance and resistance values of EMIM[FAP] at 25, 45, and 65°C.

RTIL Under Test EMIM[FAP] 1 μ L Samples											
Test Temperature 25°C				Test Temperature 45°C				Test Temperature 65°C			
Gas Type	R _{ct} (Ω)	C _{dl} (nF)	ΔC (nF)	Gas Type	R _{ct} (Ω)	C _{dl} (nF)	ΔC (nF)	Gas Type	R _{ct} (Ω)	C _{dl} (nF)	ΔC (nF)
N2	4.00E+06	7.2	0.12	N2	1.80E+07	12.2	0.6	N2	8.20E+06	17.5	6.2
400ppm	4.00E+06	7.32		400ppm	2.30E+07	11.6		400ppm	8.00E+06	11.3	
N2	316480	10.2	0.4	N2	2.11E+06	22.7	0.2	N2	7.80E+06	19.6	2.9
750ppm	314050	9.8		750ppm	2.11E+06	22.9		750ppm	8.20E+06	16.7	
N2	305710	12.7	1.6	N2	8.00E+06	8.3	0.3	N2	8.80E+06	15.1	0.5
1000ppm	272710	11.1		1000ppm	8.00E+06	8		1000ppm	8.80E+06	14.6	

Table 10 shows the results of EMIM[FAP] for all the explored temperature ranges in a dry environment. Room temperature behavior, again, follows what was shown previously with an inverse relationship describing the charge transfer resistance changes with respect to CO₂ concentration and a proportional trend describing the change in the double layer capacitance. Again, we see an inversely proportional change in the double layer capacitance change with respect to CO₂ concentration as the temperature is increased. This implies that as the temperature of the

environment is increased for EMIM[FAP] the physisorption interaction is weakened, but not enough to where the EDL is insensitive to CO₂ concentration changes.

While understanding that the temperature of the RTIL does affect their ability to physisorb CO₂, from an electrochemical perspective these materials are still able to differentiate capacitive changes in the EDL with respect to CO₂ concentration. While the method of interaction may have changed, this does not reduce the capabilities to be utilized in the development of a CO₂ sensor. However, temperature is just one of many concerns for these materials in being able to detect CO₂ and can be taken into account through the utilization of an integrated temperature sensor to determine what calibration constants or look up tables to use at the different temperature ranges.

4.4 Temperature and Humidity Results of RTILs

While the RTILs under review have still been able to be successfully shown to operate at elevated temperatures, a concern is their ability to detect CO₂ while also being exposed to H₂O. While the anions initially selected were shown to have the strongest hydrophobicity response with respect to water, the cation EMIM has been known to be sensitive to water. While showing sensitivity to water is a hurdle that can be overcome by the integration of an additional humidity sensor, understanding how large of an effect it may have is of larger importance. While this is only a summary and overview of the work, a larger DOE was conducted with respect to the 9 different combinations of temperature (25, 45, and 65 °C) and humidity (25, 45, and 65 %RH). The summary will narrow its reporting to only deal with 25/25, 45/45, 65/65 °C/%RH respectively. This will allow for the detailed analysis for a later publication detailing their overall behavior in a multi-gas/temperature environment.

4.4.1 RTIL capacitive response at 65 %RH and 65 °C

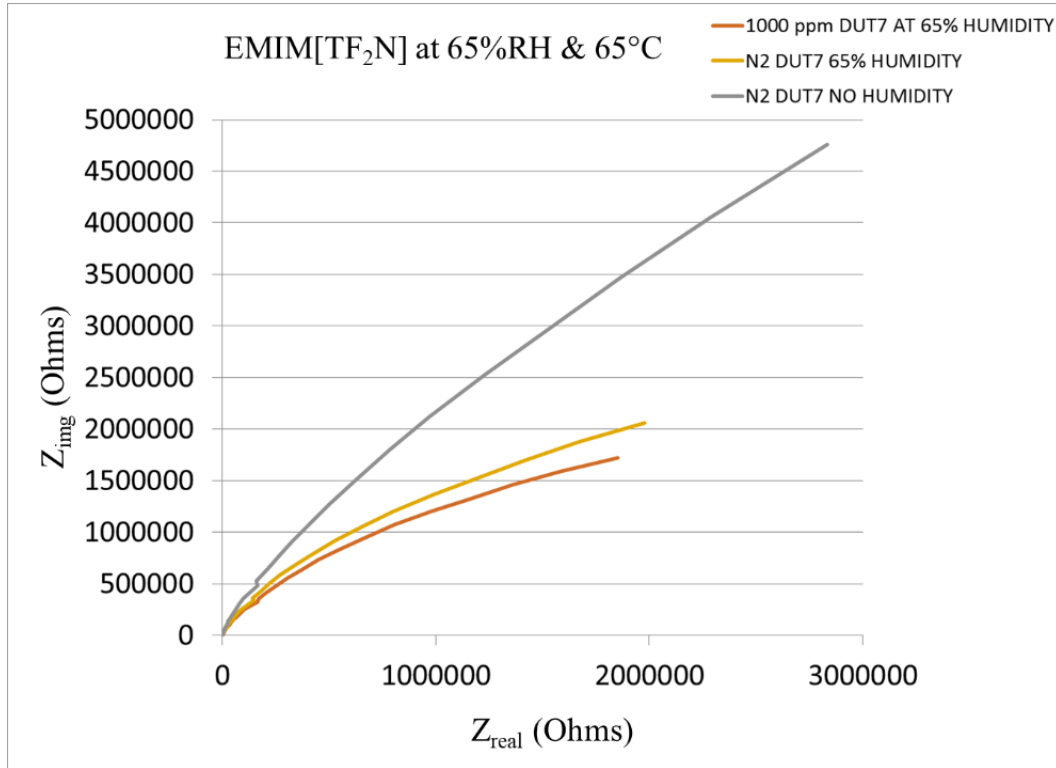


Figure 34: Nyquist plot of EMIM[TF₂N] at 65 %RH and 65°C. This shows the change from N₂ baseline to N₂ with humidity to 400ppm CO₂ with humidity.

The maximum & most extreme condition was explored first. This consisted of 1000ppm CO₂ at 65 % RH and 65 °C. From Figure 34 we see that with just the addition of 65% RH into a N₂ environment, a significant reduction of the charge transfer resistance is observed with respect to the humidity. This shows that the presence of water does affect the charge transfer and double layer response of the system. However, we also note that while a large response is shown with the addition of H₂O, we still see a response to the addition of CO₂. The extracted capacitance change at the EDL is observed to be 0.9 nF.

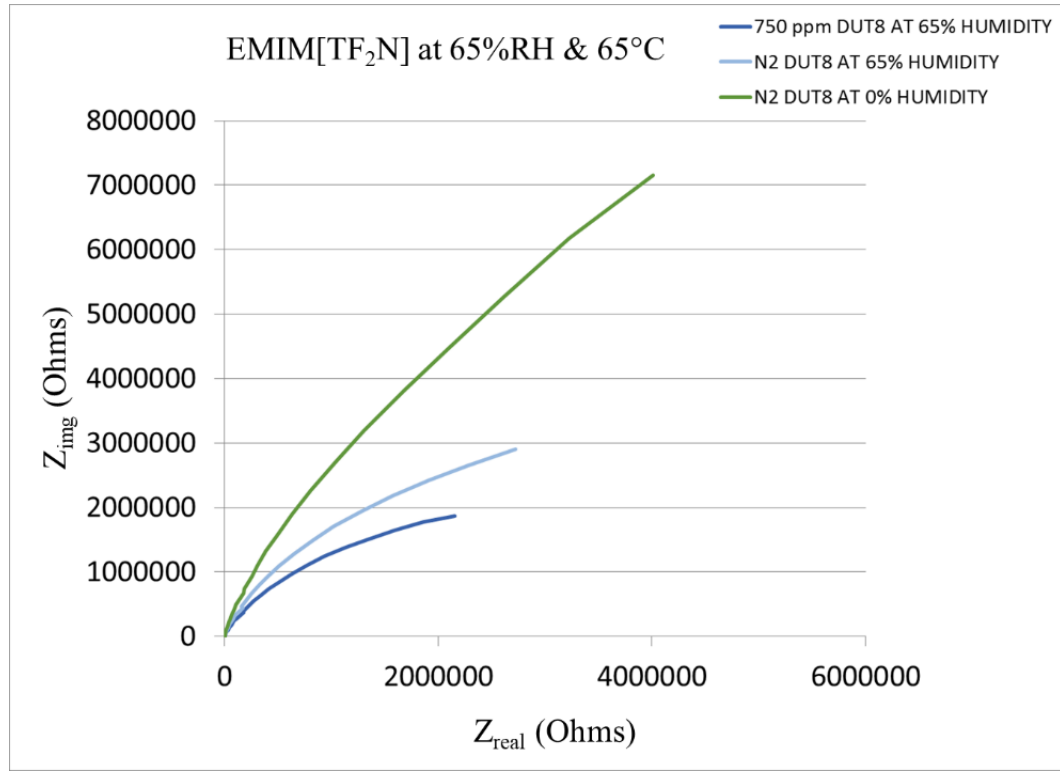


Figure 35: Nyquist plot of EMIM[TF₂N] at 65 %RH, 65 °C, and 750ppm.

The behavior of EMIM[TF₂N] in 750ppm CO₂ at 65 %RH and 65 °C , Figure 35, shows a similar trend as at 1000ppm. The RTIL shows a significant reduction in the charge transfer behavior from the addition of humidity, but is still able to interact with CO₂ as it preferentially interacts with CO₂. To that end, the change we observe from N₂ with humidity to CO₂ with humidity is found to be 1.20 nF. Following a similar vein to the previous two conditions, we explore the application of 400ppm of CO₂, Figure 36. We see again see the reduction of the capacitance with H₂O, but see an even greater change in capacitance with the extracted capacitance change of 22.0 nF.

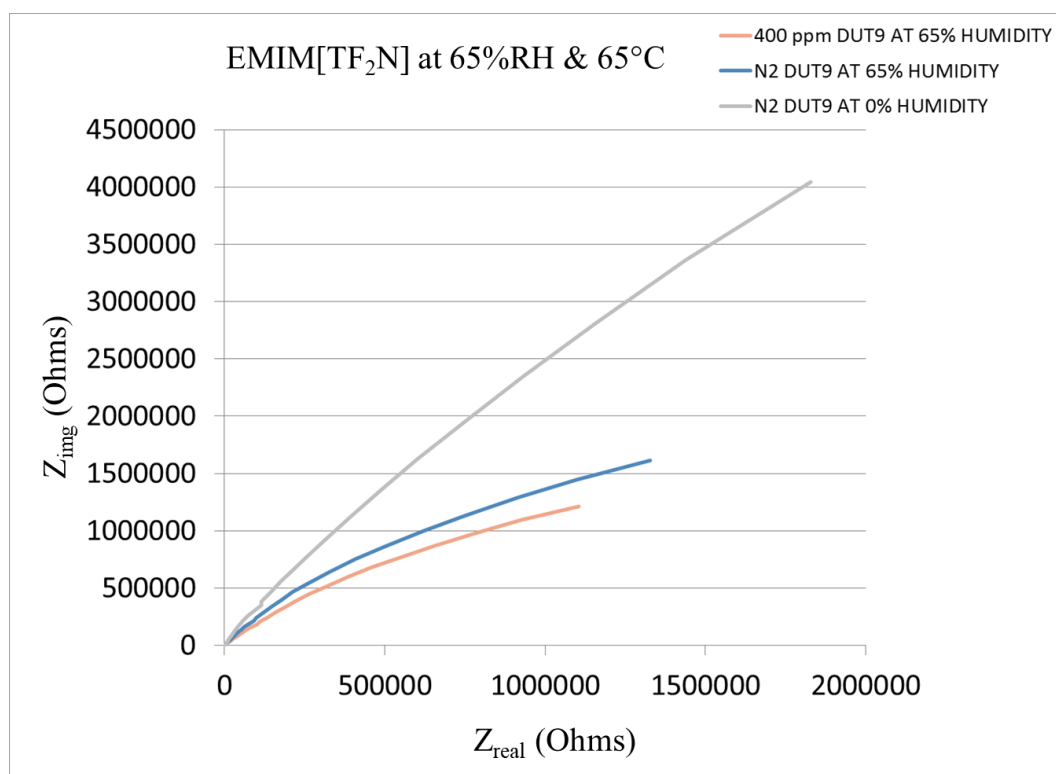


Figure 36: Nyquist plot for EMIM[TF₂N] at 65 %RH and 65 °C with 400ppm CO₂.

Behavior like that shown in the previous temperature only modulation is shown across these different CO₂ concentrations when humidity is held constant. However, a stronger capacitive response is shown with the addition of H₂O to the system. This is leading towards an additive or enhancement effect occurring with the combination of CO₂ and H₂O such that at lower concentrations allows for a higher opportunity of interaction which would explain the increased capacitive response.

Summarized in Table 11, it is shown that for both EMIM[TF₂N] as well as EMIM[FAP], Appendix A, we see an inverse relationship of capacitance change with respect to CO₂ concentration. This is thought to occur due to a competing interaction between the CO₂ and H₂O as well as the H₂O and EDL.

Table 11: Summary table showing the extracted capacitance change for EMIM[FAP] and EMIM[TF₂N] at 65 %RH and 65 °C between N₂ and CO₂.

RTIL	400ppm	750ppm	1000ppm
EMIM[FAP]	3.9nF	3.0nF	1.4nF
EMIM[TF ₂ N]	22.0nF	1.20nF	0.9nF

4.4.2 RTIL capacitive response at 45 %RH and 45 °C

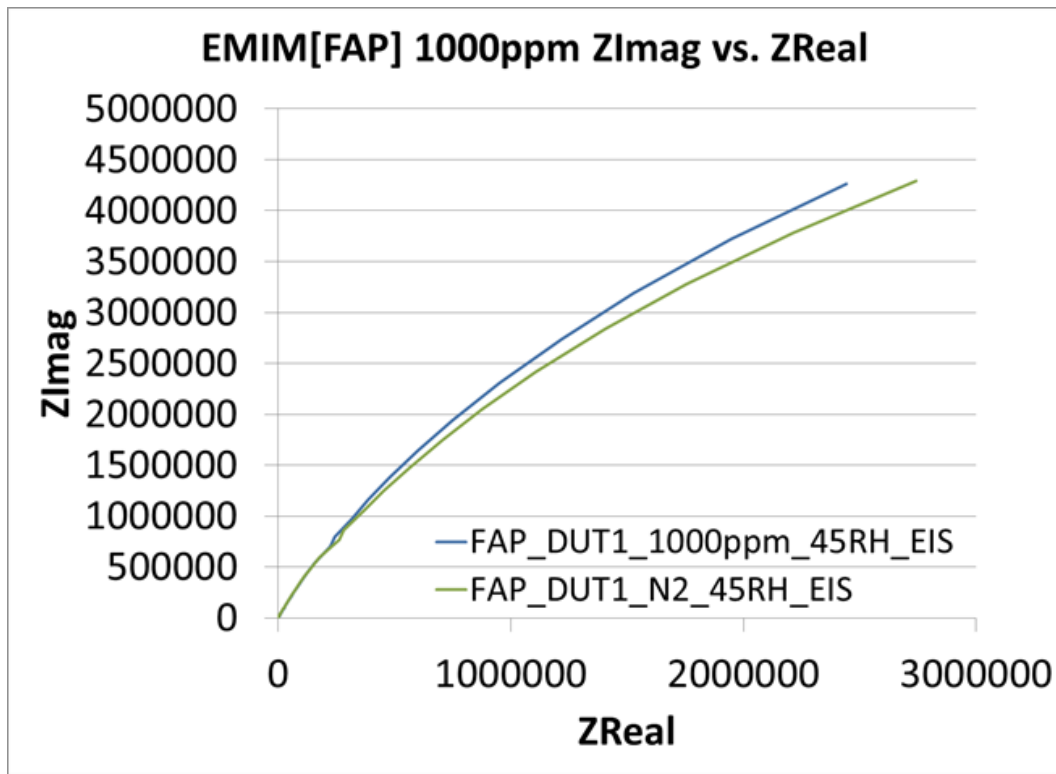


Figure 37: Nyquist plot of EMIM[FAP] at 45 %RH and 45 °C in 1000ppm CO₂.

EMIM[FAP] was also tested using the same process as EMIM[TF₂N]. Testing at the extremes first allowed us to determine if further investigation was needed. Because both showed similar

response to CO₂ at 65 %RH and 65 °C, it was decided to begin investigating the results at 45 %RH and 45 °C for both of these RTILs.

Looking at Figure 37, it is shown that when EMIM[FAP] is exposed to an initial response to the addition of humidity is observed. Forgoing the initial dry N₂ runs, it is shown that when the system is doped with 1000ppm CO₂, there is an increase in the charge transfer resistance shown by the increase of the semicircular radius. However, it still shows an absolute change of 8.1 nF at the given humidity conditions. This behavior was unexpected, but showed consistent between detectors at this concentration of CO₂.

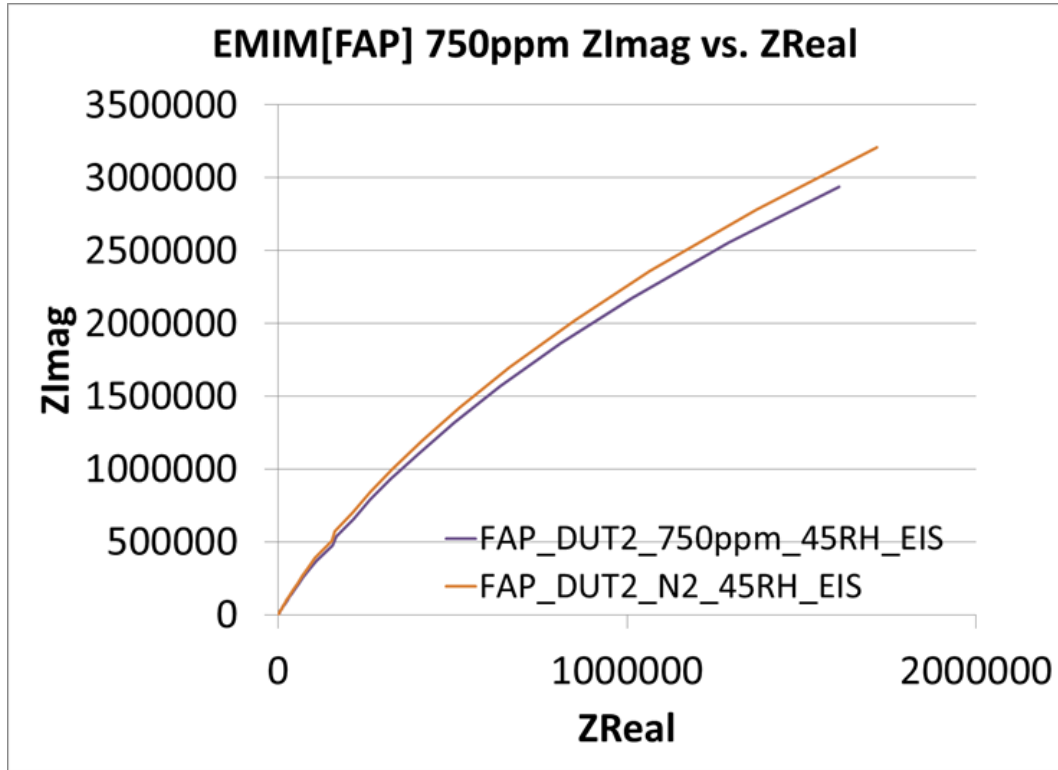


Figure 38: Nyquist plot of EMIM[FAP] at 45 %RH and 45 °C with 750ppm CO₂.

When the detectors were ran for 750ppm, Figure 38, it is shown that an absolute EDL capacitance change of 4.3 nF change occurs between the humidified N₂ and CO₂ runs. The

decrease of the charge transfer resistance and an increase in the EDL capacitive response is shown by the reduction in radius of the semicircular EIS response shown in Figure 38: Nyquist plot of EMIM[FAP] at 45 %RH and 45 °C with 750ppm CO₂.. This shows that there may be an inflection point between 750ppm and 1000ppm due to an interaction between the RTIL, H₂O, and CO₂.

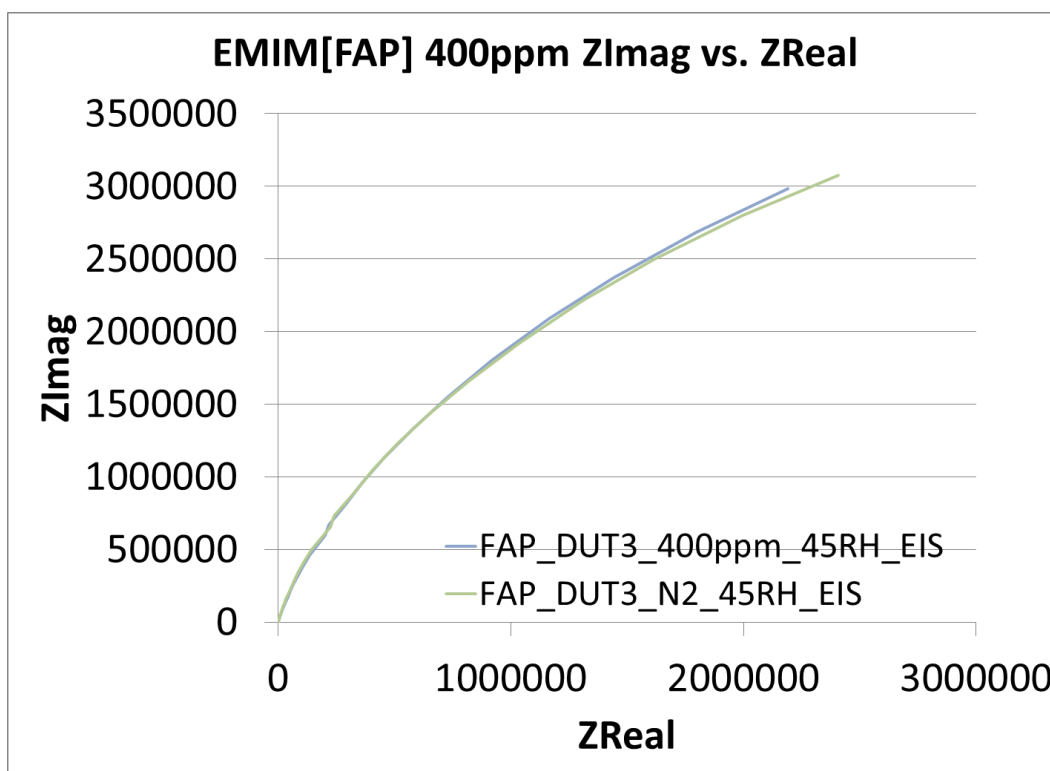


Figure 39: Nyquist plot of EMIM[FAP] at 45 %RH and 45 °C in 400ppm CO₂.

The final set of data shown is that of the lowest concentration; that of 400ppm in Figure 39. The reduction in charge transfer resistance and increase in capacitive response is still shown between the N₂ and CO₂ runs, but the overall capacitive change is less. Summarized in Table 12, the capacitive change is 1.8 nF for 400ppm.

Table 12: Summary table showing the extracted capacitance change for EMIM[FAP] and EMIM[TF₂N] at 45 %RH and 45 °C between N₂ and CO₂.

RTIL	400ppm	750ppm	1000ppm
EMIM[FAP]	1.8nF	4.3nF	8.1nF
EMIM[TF ₂ N]	4.3nF	16.5nF	34nF

The capacitive changes for the different CO₂ concentrations for the RTILs is summarized in Table 12. For the 45%/RH and 45 °C conditions, the overall absolute capacitance change does track proportionally with the CO₂ concentration. EMIM[TF₂N] shows a significant increase in EDL capacitance change at 1000ppm. On the order of 34 nF. Understanding the behavior of these RTILs close to what is considered ambient conditions is also important to cover the gambit of possible applications. The data for the EIS CO₂ runs of EMIM[TF₂N] is provided in Appendix A.

4.4.3 RTIL capacitance response at 25 %RH and 25 °C

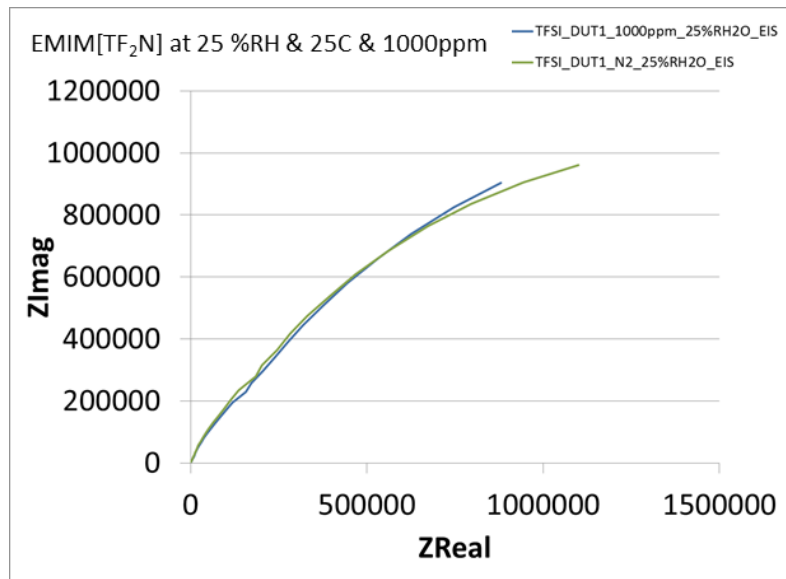


Figure 40: Nyquist plot of EMIM[TF₂N] at 25 %RH and 25 °C at 1000ppm CO₂.

Room temperature and 25 %RH was also chosen as part of an overall larger DOE, Appendix A, in efforts to explore and understand the behavior of these RTILs at the lower edge of our suggested operation space. For the dosing of EMIM[TF₂N] at 1000ppm, it is shown in Figure 40 that after the dosing of N₂ with humidity, we see a very little change in terms of the charge transfer resistance, but the overall capacitance change is quite large, Table 13 , at 19.6 nF.

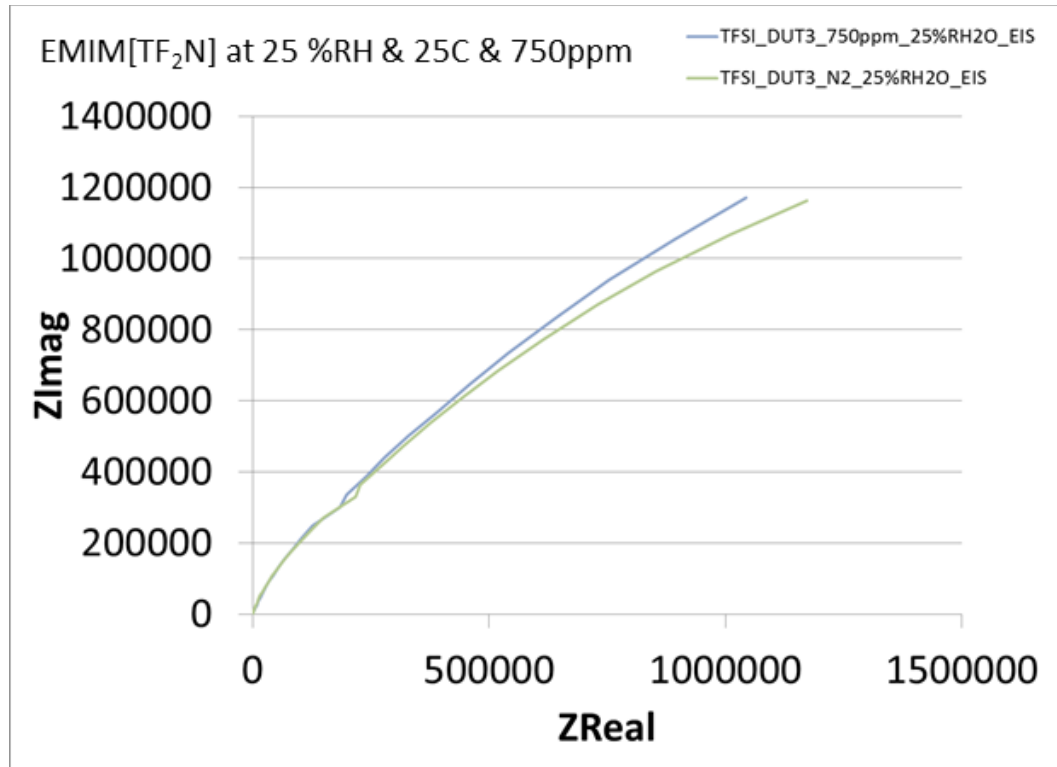


Figure 41: Nyquist plot of EMIM[TF₂N] at 25 %RH and 25 °C at 750ppm CO₂.

The data shown in Figure 49, shows that there is an increase in the overall charge transfer resistance, but the capacitive response of the system does increase. Through fitting of the data, it is found that an overall change of 4.8 nF is found when it comes to the EDL capacitance change between the N₂ and CO₂ runs. Room temperature behavior is starting to show a downward trend when it comes to proportional response to CO₂ concentration.

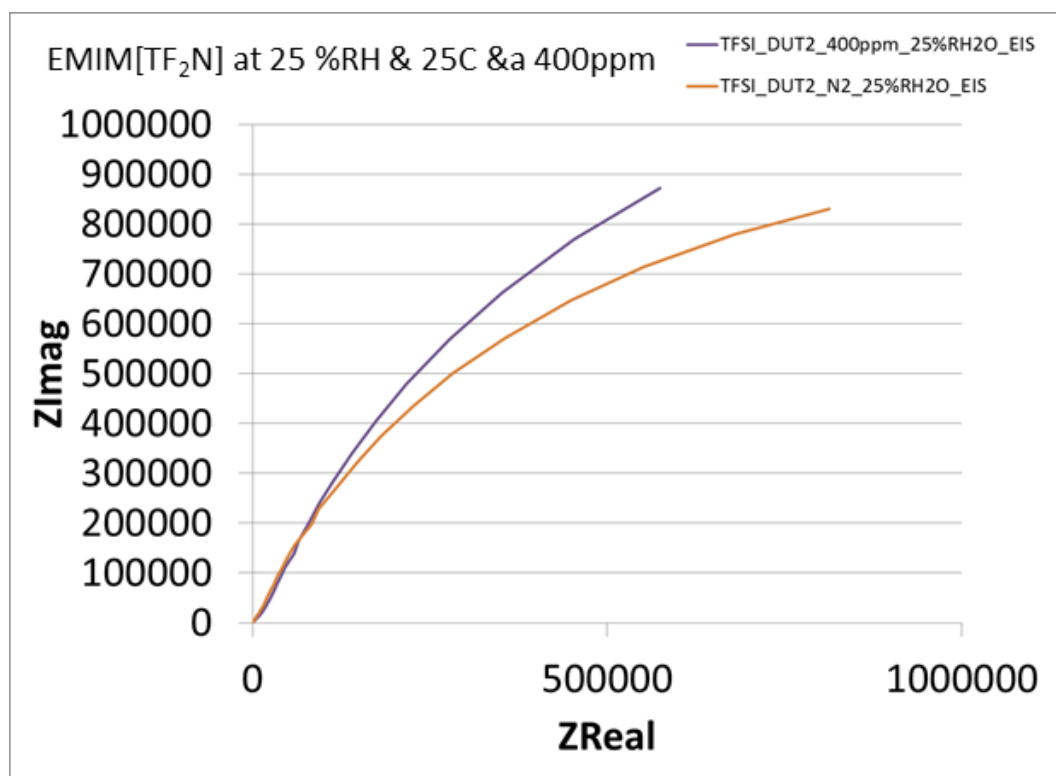


Figure 42: Nyquist plot of EMIM[TF₂N] at 25 %RH and 25 °C at 400ppm CO₂.

The 400ppm run continues to show the trend of an increase in charge transfer resistance, Figure 42. The absolute value of the capacitive change for these runs is 5.9 nF. The overall trend for EMIM[TF₂N] at 25 %RH and 25 °C is that of a proportional capacitive response with respect to CO₂. While the Nyquist plots for EMIM[FAP] are included in Appendix A, it also shows a continuing proportional trend with respect to the CO₂ concentration applied at 25 %RH and 25 °C.

Table 13: Summary table showing the extracted capacitance change for EMIM[FAP] and EMIM[TF₂N] at 25 %RH and 25 °C between N₂ and CO₂.

RTIL	400ppm	750ppm	1000ppm
EMIM[FAP]	5.9nF	8.8nF	11.5nF
EMIM[TF ₂ N]	2.3nF	4.8nF	19.6nF

4.4.4 Discussion of humidity effects

From the previous results, an interesting and complex set of responses have been shown for EMIM[TF₂N] and EMIM[FAP]. The addition of temperature and humidity cause significant changes from the initial dry environment results. Through the changes in the charge transfer resistance (R_{ct}) as well as the EDL capacitance (C_{DL}) we begin to start developing a possible hypothesis for what is occurring.

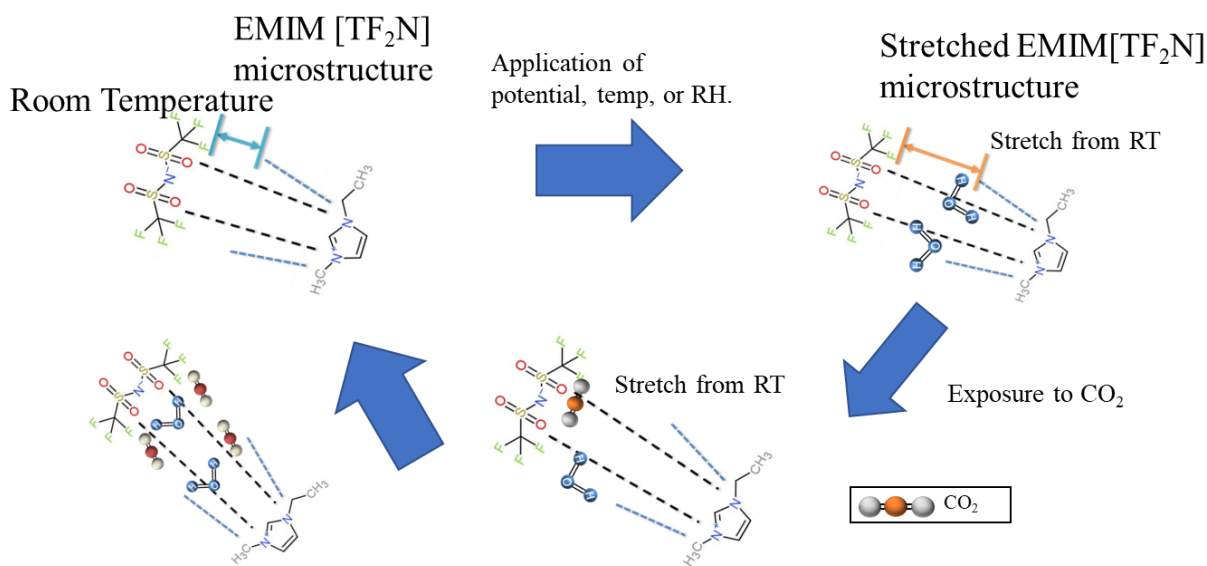


Figure 43: Proposed interaction mechanism for EMIM[TF₂N] with the addition of heat, humidity, and CO₂ concentrations.

Figure 43 and Figure 44 show such hypotheses of interaction for each of the RTILs. When either has a potential or temperature applied to it, the interaction between the anion and cation begins to weaken, or stretch. The different components of the individual RTIL molecules may show a weaker interaction, so there may be more interstitial space between the anions and cations in both the bulk and EDL regions of the system or there may even be secondary processes that are occurring that have yet to be reported on. With the introduction of just CO₂, at low temperatures,

the high solubility (low Henry's constant) allows for the preferential diffusion of CO₂ to occur with the different RTILs regardless of H₂O presence. As the CO₂ quickly reaches the EDL layer, the applied potential across the electrodes allows for CO₂/anion to interact. As discussed in the introduction; fluorinated anions are known to be able to interact with CO₂ preferentially over other gases.

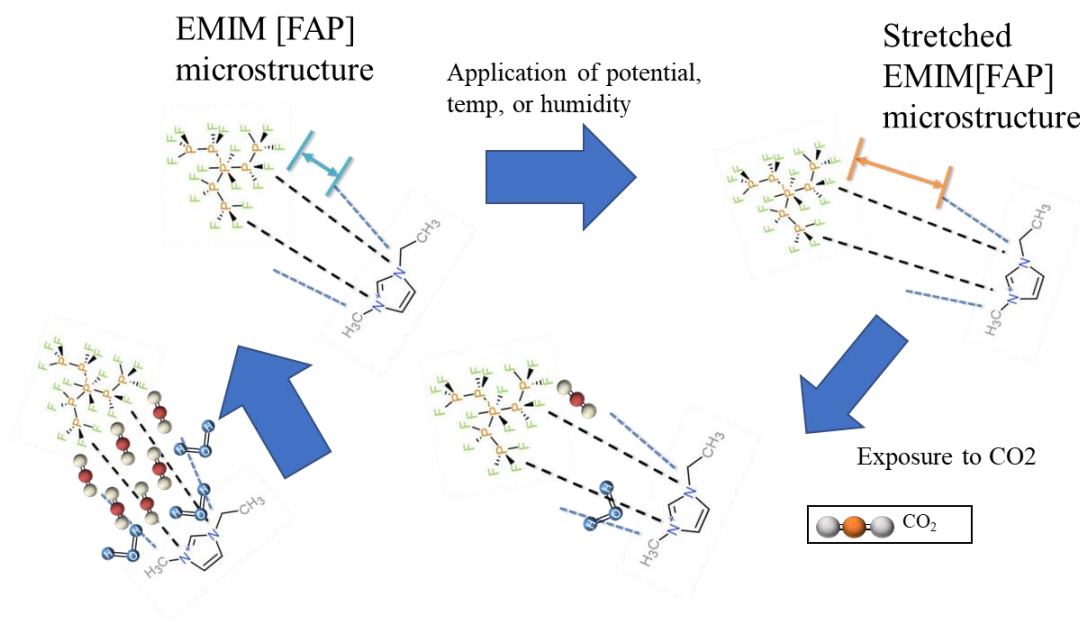


Figure 44: Proposed interaction mechanism for EMIM[FAP] with the addition of heat, humidity, and CO₂ concentrations.

For the results reported for EMIM[TF₂N] there is an overall downward trend in C_{DL} as one increases the temperature of the RTIL. These upward and downward trends are ideal for the SRC project because this allows for the future development of calibration curves that would be used to extract the actual ppm concentration given the impedance change from baseline in combination with knowing the local temperature and humidity values. This is hypothesized to be caused by the increasing Henry's constant that is shown for most RTILs in the literature as temperature

increases. [27,31,56] The physisorption provides the CO₂ the ability to interact, but the interaction mechanism may have weakened such that there is no real capacitive interaction. This idea is also bolstered by the fact that, overall from Table 9, the R_{ct} of the system remains invariant once the temperature is raised from 25 °C. Overall, EMIM[TF₂N] has shown the largest capacitive response across the selected temperature and humidity concentrations. [57] It's ability to show non-oscillatory behavior at the different conditions is ideal when attempts to develop calibration tables occurs.

For EMIM[FAP] the opposite relationship occurs. As one begins to increase the temperature and humidity of the system, the capacitive response not only decreases, but the trend also changes direction in the case of the 65/65 testing simlary to EMIM[TF₂N]. It is important to note that one of the major differences between the two different RTILs is the quantity of fluorine available for interaction. It is possible to conclude from Table 10 that with the slight changes of R_{ct} and large changes in the C_{DL} that there is more potential for CO₂ interacting at the lower temperature/humidity thresholds than at the 65/65 regime. While still sensitive to CO₂, EMIM[FAP] has shown to respond with a lower overall impedance change than that of EMIM[TF₂N] though it still shows potential to be utilized in continued sensor development.

In summary, utilizing Table 14, the combination of both temperature and humidity has a profound effect of the response of the two different RTILs. For EMIM[FAP] at low concentrations of CO₂, we see a larger overall capacitive behavior across than that of EMIM[TF₂N]. This may be due to a changing of the interaction mechanism or interstitial diffusion ability of the CO₂ within the RTIL. It has been mentioned in the literature for BMIM[BF₄] that as one increases the amount of humidity an RTIL is exposed to, the electrochemical window of the system shrinks, this may

be a cause in the higher capacitive response to CO₂ at 65/65. [56] At 65/65 we see a high C_{DL}, but an even higher one is observed at 45/45 for EMIM[TF₂N] and at 25/25 for EMIM[FAP]. The anionic moiety appears to be the main driver of the overall environment interaction that EMIM. There may also be water molecules interacting with the CO₂ as well as interact with the RTIL anions in a competitive process. Further development is warranted for these materials as actual CO₂ sensing devices due to their initial ability to responds to CO₂ across a large range of temperature and humidity values.

Table 14: Summary of capacitance change to CO₂ concentration as the temperature and humidity are varied for EMIM[FAP] and EMIM[TF₂N].

65C at 65% RH			
RTIL	400ppm	750ppm	1000ppm
EMIM[FAP]	3.9nF	3.0nF	1.4nF
EMIM[TF ₂ N]	22.0nF	1.20nF	0.9nF
45C at 45% RH			
EMIM[FAP]	1.8nF	4.3nF	8.1nF
EMIM[TF ₂ N]	4.3nF	16.5nF	34nF
25C at 25% RH			
EMIM[FAP]	5.9nF	8.8nF	11.5nF
EMIM[TF ₂ N]	2.3nF	4.8nF	19.6nF

Overall both EMIM[TF₂N] and EMIM[FAP] showed that these materials predictable responses with respect to CO₂ concentration across the different environmental conditions explored. While the mechanism is still being investigated, the empirical results show that their behavior is dominated by the CO₂ interaction over that of H₂O. With respect to the SRC sponsored projects requirements, EMIM[TF₂N] was evaluated as the better of these two RTILs investigated for further studies towards a new low power CO₂ sensor.

CHAPTER 5

CONCLUSIONS AND FUTURE EFFORTS

5.1 Conclusions on the Use of RTILs in residual CO₂ gas sensing

These previous chapters have shown the empirical approach of how three fluorinated RTILs were evaluated for SRC sponsored efforts towards the development of a new form of CO₂ gas sensor. The physical properties of these RTILs lean them towards applications utilizing gold electrodes over carbon electrodes due to their lower standard deviation across the different RTILs explored. When the RTILs were exposed to CO₂ without humidity, all three showed empirically to be sensitive to the three different CO₂ concentrations. EMIM[BF₄] was excluded from the further temperature and humidity studies due to its solubility in water.

From the initial temperature investigation, both EMIM[FAP] and EMIM[TF₂N] continued to show sensitivity to CO₂ from 25°C to 65°C. Specifically, EMIM[FAP] showed a proportional trend to CO₂ in its C_{DL} with respect to temperature while EMIM[TF₂N] showed an inverse proportionality with respect to temperature. With the addition of humidity to the equation, it was shown that both materials behave proportionally with respect to CO₂ concentration to each other at 25°C and 25 %RH as well as at 45°C and 45 %RH. At the extreme end of the operational range 65°C and 65 %RH however, their behaviors diverge with an inverse response to CO₂ at these conditions. When comparing the behavior of these RTILs, the evaluation was toward ease of signal sensitivity and establishment of CO₂ response trends. While EMIM[FAP] still shows sensitivity, EMIM[TF₂N] has the higher overall capacitive response to CO₂ across the different temperature and humidity ranges. The mechanism for the interaction of CO₂, H₂O, and a given fluoride based anion has not clearly addressed in the literature, but further work will be performed

to better understand the actual effects occurring within the RTIL in efforts toward building a CO₂ gas sensing system.

5.2 Future work utilizing RTILs in gas sensing

5.2.1 Chronoamperometry

Chronoamperometry is another potentiostatic electrochemical technique that is used in investigating the diffusion behavior of different chemicals by observing the response and decay behavior of the system, Figure 45. [60] The method applies a known potential step to the system. The system equalizes with respect to this applied potential. The applied potential is either stepped up or down the current response of the system is measured. [61] The charging or discharging of the system and how it varies gives us insight into how the EDL of the system is reacting with respect to the presence of CO₂. [61]

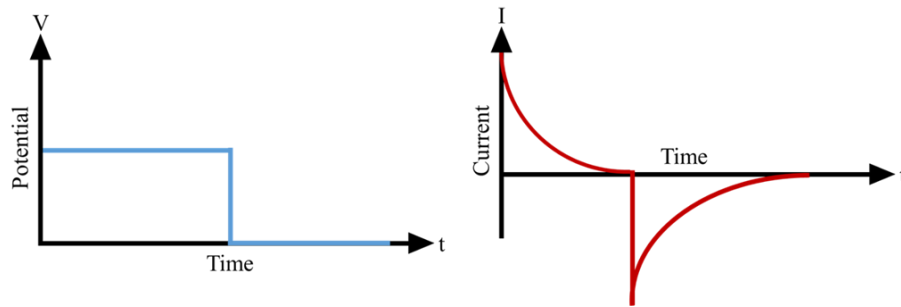


Figure 45: Schematic of the potential applied and possible current response from and electrochemical system when performing Chronoamperometry.

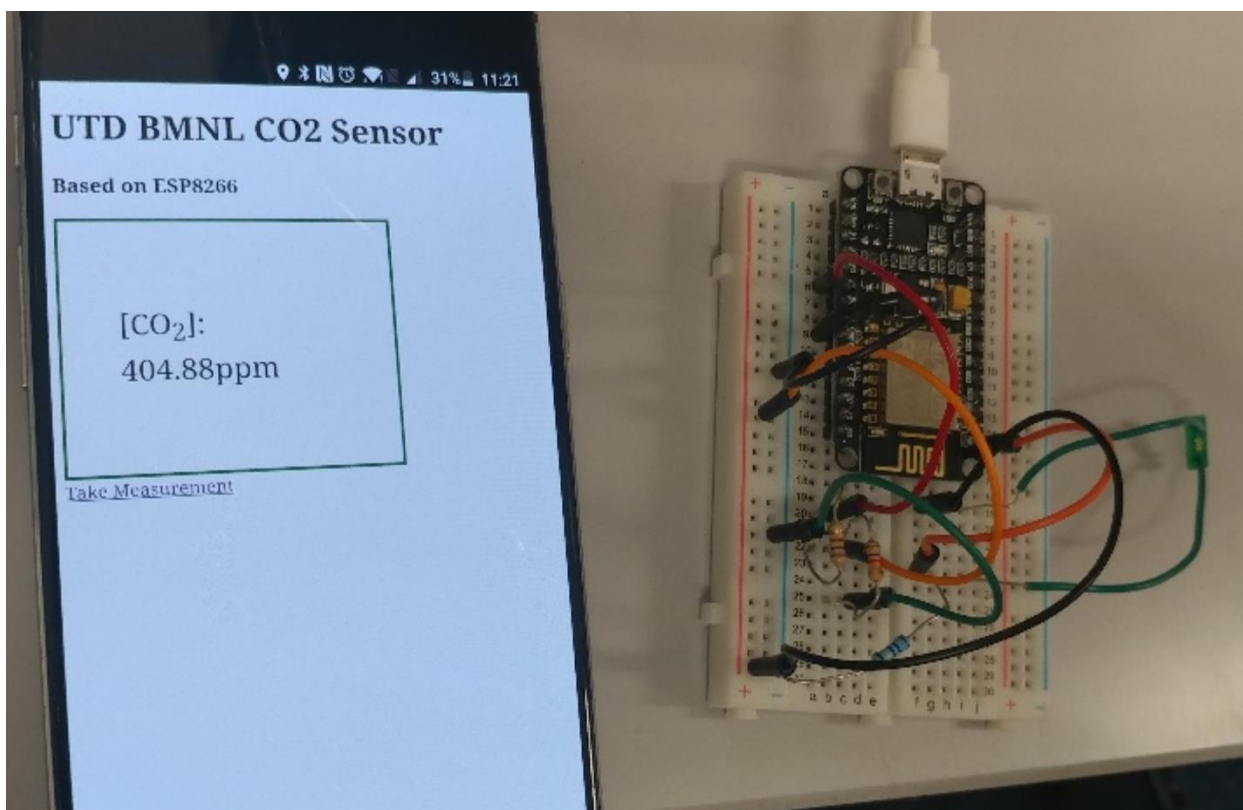


Figure 46: Mockup of EMIM[TF₂N] sensing system operating in ambient environment.

The proposed sensing system will periodically monitor the CO₂ conditions and compare a measured current to a look up table utilizing local temperature and humidity values. Figure 46 shows a mockup of such a detector communicating with a cell phone. It reports a local CO₂ value as a form of personal sensing equipment. Figure 47 shows the mockup response in a high CO₂ environment. Trigger levels could be defined such that the monitoring device alerted the user to a danger. Next year's SRC deliverables are towards the final development of a working prototype CO₂ sensing system using RITLs. Additional work involves using other analytical techniques to explore the interaction mechanisms that a combination of gases would have on these fluorinated RTILs. From this, novel empirical models can be developed to describe these interactions.

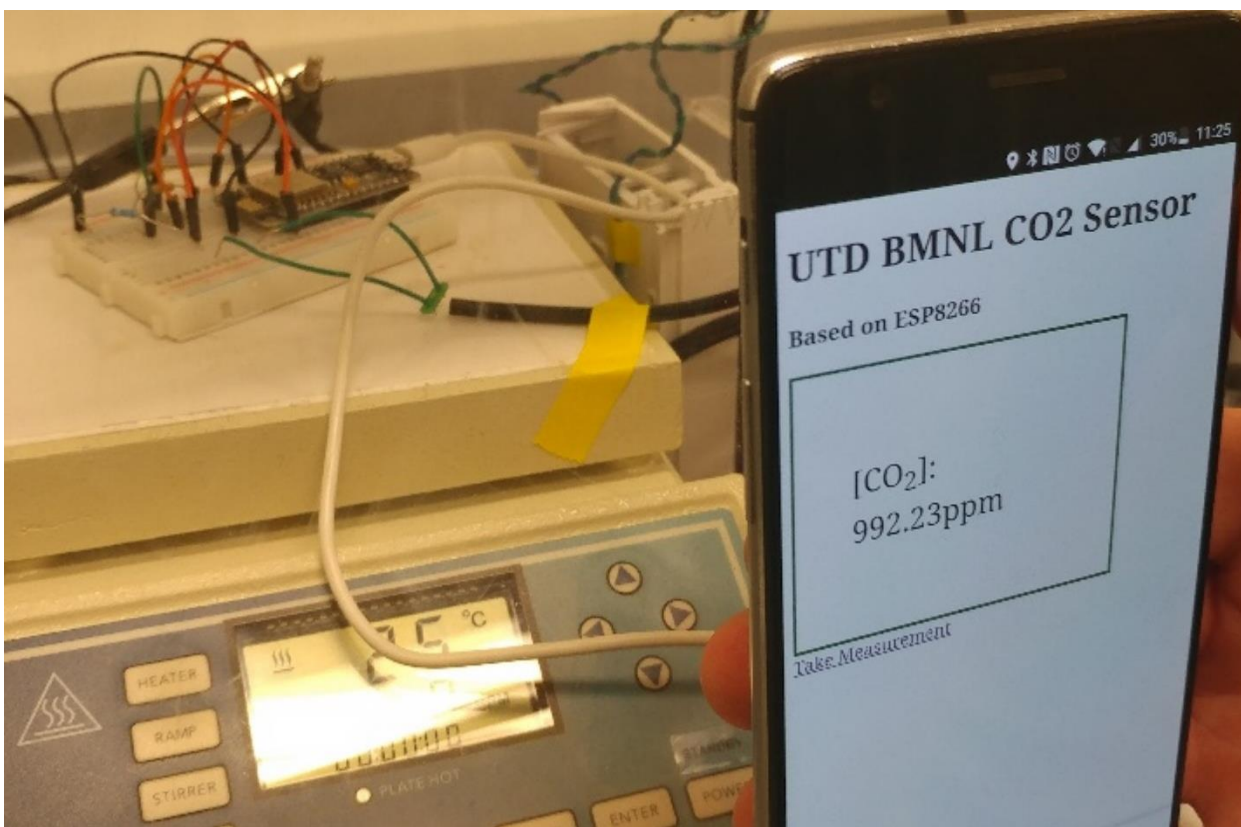


Figure 47: Mockup of EMIM[TF₂N] sensing system in an elevated CO₂ environment.

In conclusion, the need for low powered sensors that can work in different humidity and temperature environments is needed. Current detectors on the market all suffer from one issue or another; whether it be cross sensitivity, drift, lifetime, or temperature restrictions. Fluorinated room temperature ionic liquids offer a novel solution to these challenges due to their high temperature capabilities, selectivity towards CO₂, and stable electrochemical properties. It has been shown that of the RTILs studied that EMIM[TF₂N] show the most promise for the development of the next generation CO₂ sensor.

APPENDIX

EMIM[TF₂N] plots at 45 %RH and 45 °C

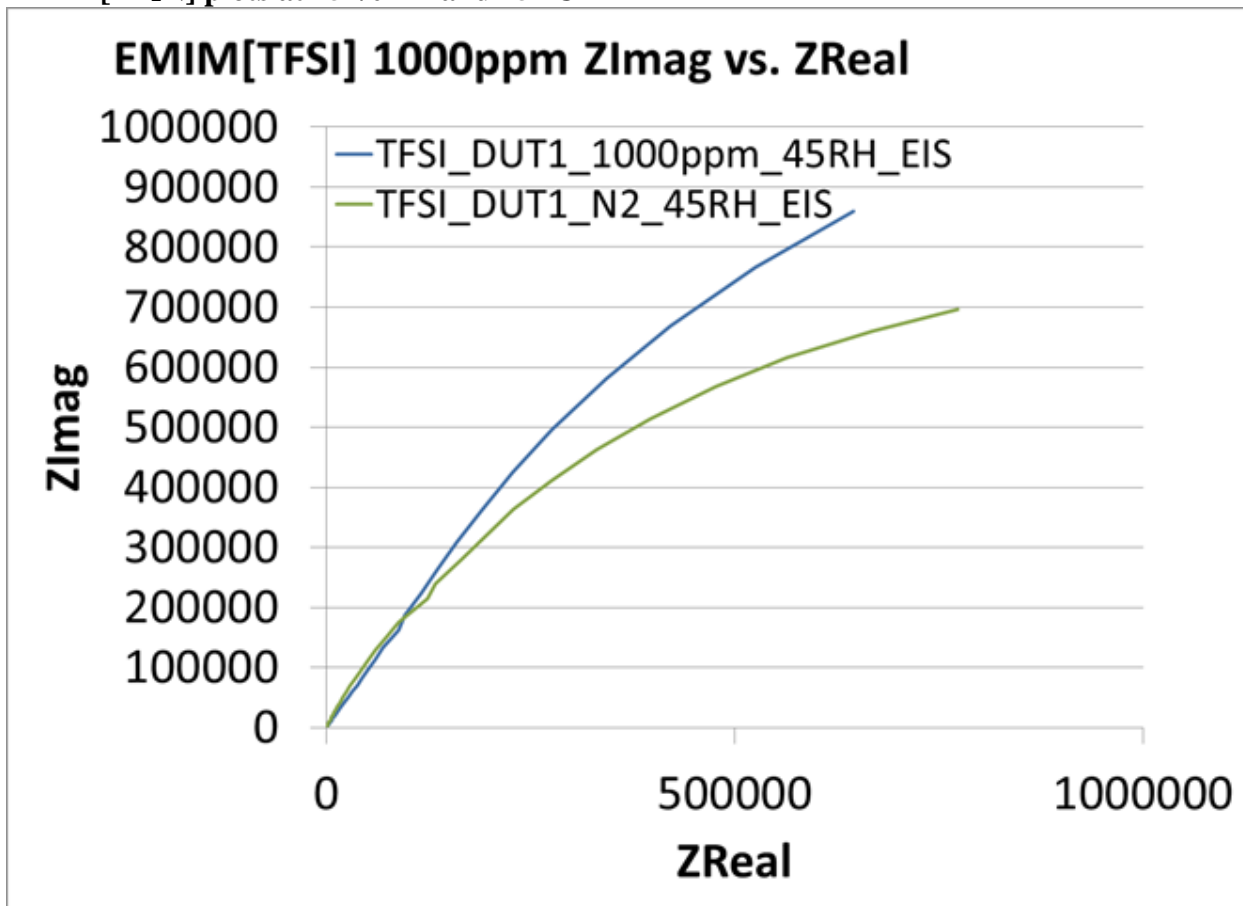


Figure 48: Nyquist of EMIM[TF₂N] at 45 %RH and 45 °C at 1000ppm CO₂.

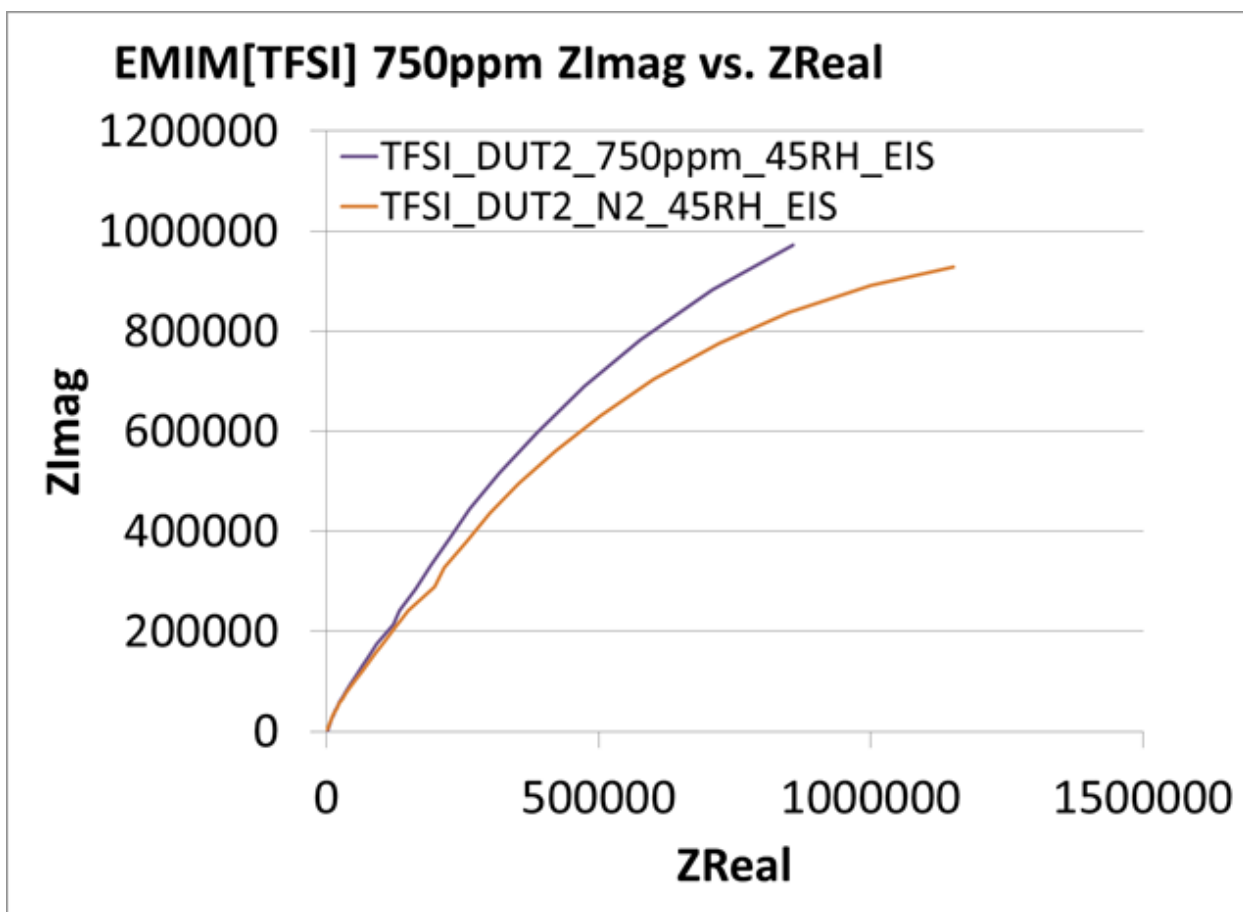


Figure 49: Nyquist of EMIM[TF2N] at 45 %RH and 45 °C at 750ppm CO₂.

EMIM[FAP] plots at 25 %RH and 25 °C

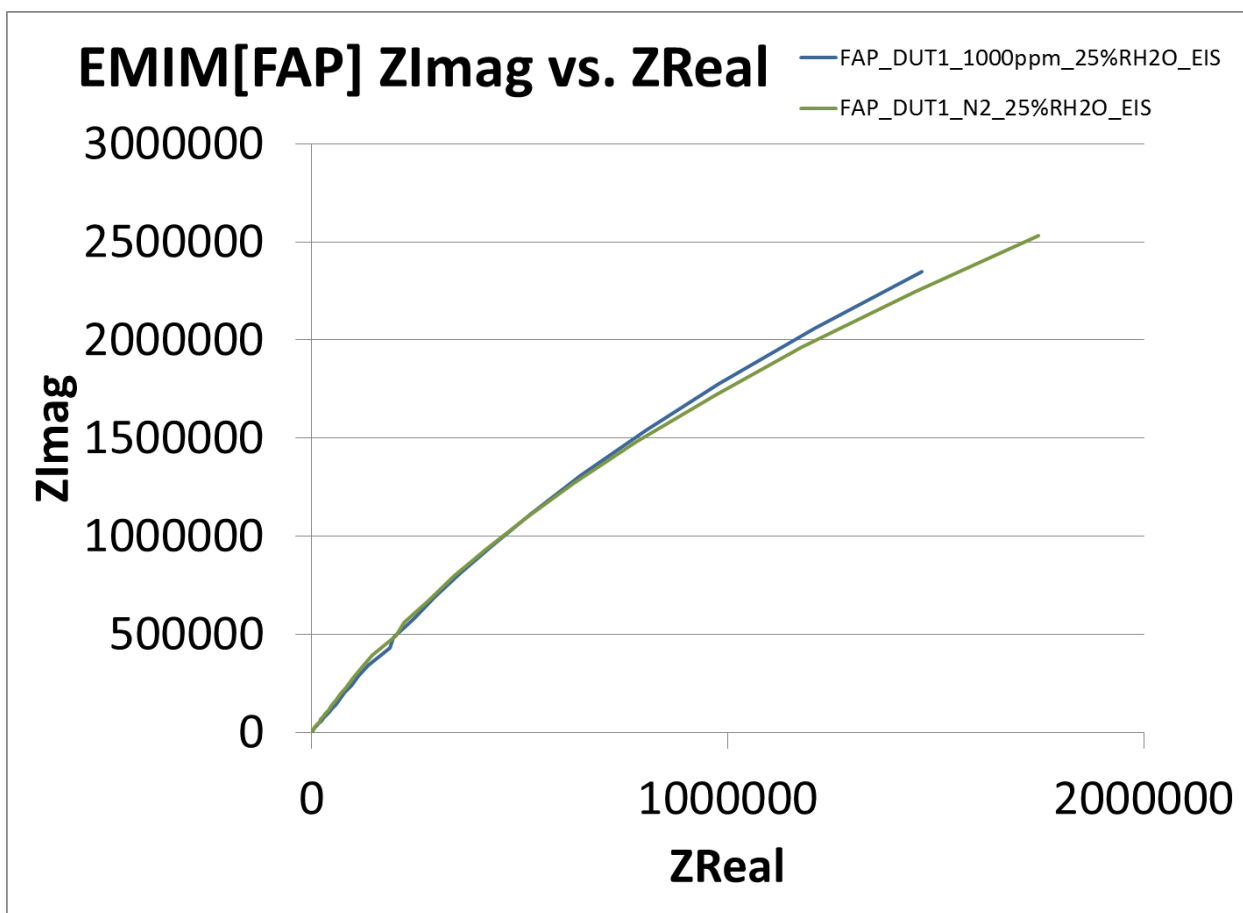


Figure 50: Nyquist plot of EMIM[FAP] at 25 %RH and 25 °C at 1000ppm CO₂.

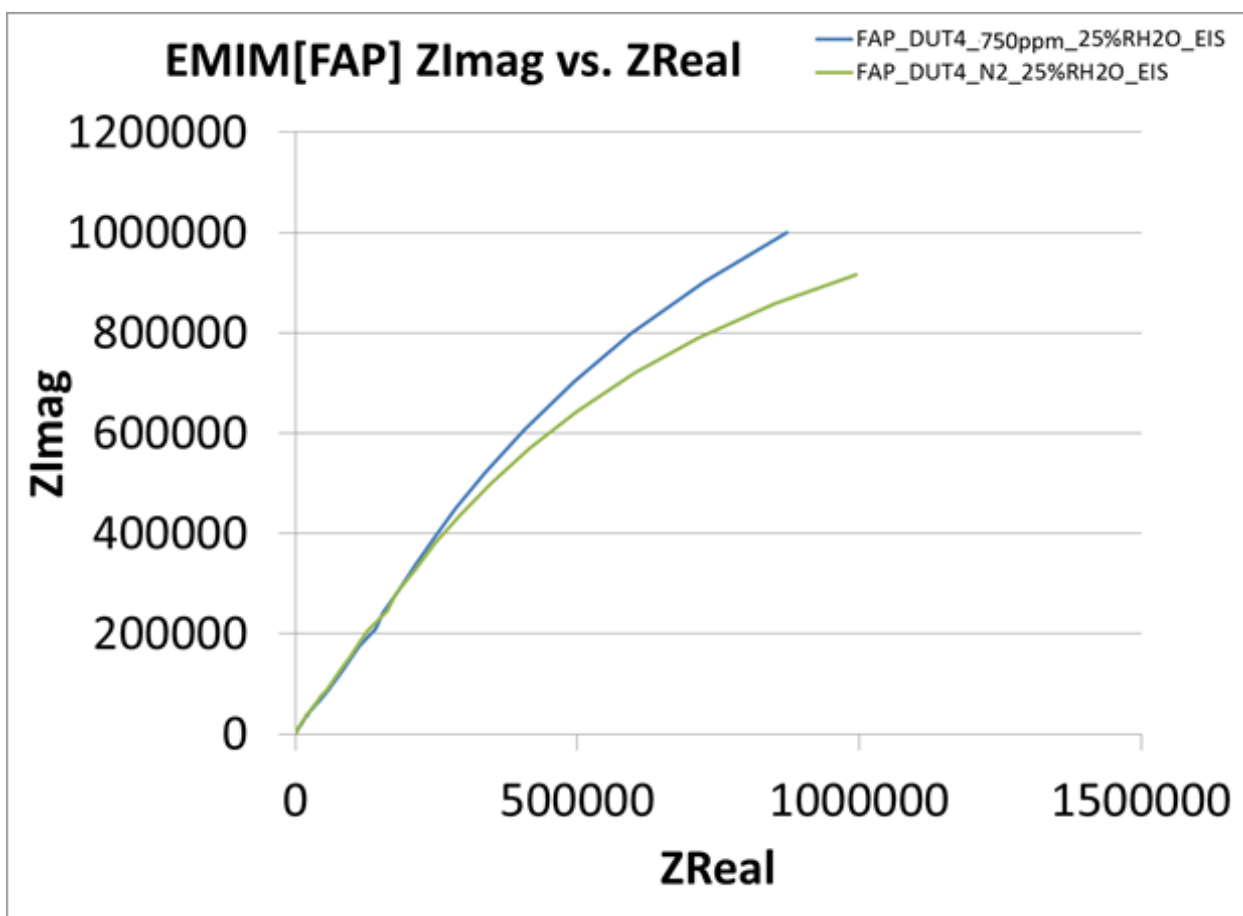


Figure 51: EMIM[FAP] Nyquist plot of EMIM[FAP] at 25 %RH and 25 °C at 750ppm CO₂.

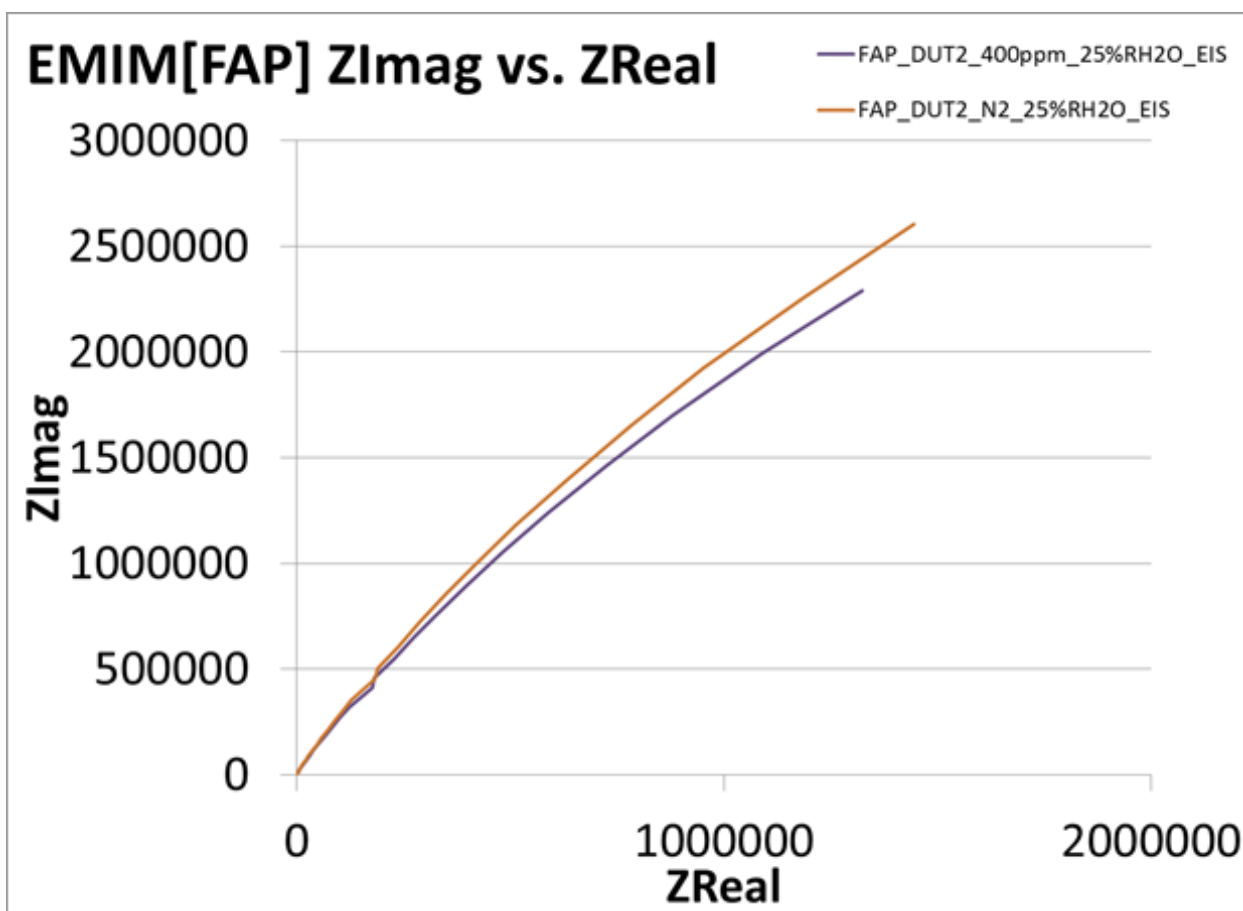


Figure 52: Nyquist plot of EMIM[FAP] at 25 %RH and 25 °C at 400ppm CO₂.

Overall DOE results for all combinations of CO₂, humidity, and temperature

Table 1: Summary tables detailing all possible combinations of temperature and humidity for EMIM[TF₂N] and EMIM[FAP] with 400, 750, and 1000ppm CO₂ concentrations.

Capacitive Change at 65C at 65% RH				Capacitive Change at 45C at 65% RH				Capacitive Change at 25C at 65% RH			
RTIL	400ppm	750ppm	1000ppm	RTIL	400ppm	750ppm	1000ppm	RTIL	400ppm	750ppm	1000ppm
EMIM[FAP]	3.9nF	3.0nF	1.4nF	EMIM[FAP]	17nF	27nF	29nF	EMIM[FAP]	17.9nF	23.7nF	93.1nF
EMIM[TF ₂ N]	22.0nF	1.20nF	0.9nF	EMIM[TF ₂ N]	67nF	40.1nF	29nF	EMIM[TF ₂ N]	297nF	222nF	187nF
Capacitive Change at 65C at 45% RH				Capacitive Change at 45C at 45% RH				Capacitive Change at 25C at 45% RH			
RTIL	400ppm	750ppm	1000ppm	RTIL	400ppm	750ppm	1000ppm	RTIL	400ppm	750ppm	1000ppm
EMIM[FAP]	0.2nF	1.6nF	3.1nF	EMIM[FAP]	1.8nF	4.3nF	8.1nF	EMIM[FAP]	36nF	43nF	64.1nF
EMIM[TF ₂ N]	0.6nF	1.3nF	1.8nF	EMIM[TF ₂ N]	4.3nF	16.5nF	34nF	EMIM[TF ₂ N]	40nF	88nF	137nF
Capacitive Change at 65C at 25% RH				Capacitive Change at 45C at 25% RH				Capacitive Change at 25C at 25% RH			
RTIL	400ppm	750ppm	1000ppm	RTIL	400ppm	750ppm	1000ppm	RTIL	400ppm	750ppm	1000ppm
EMIM[FAP]	0.26nF	0.4nF	0.5nF	EMIM[FAP]	0.1nF	0.2nF	0.7nF	EMIM[FAP]	5.9nF	8.8nF	11.5nF
EMIM[TF ₂ N]	1.5nF	1.8nF	3nF	EMIM[TF ₂ N]	0.2nF	0.39nF	1.3nF	EMIM[TF ₂ N]	2.3nF	4.8nF	19.6nF

BIBLIOGRAPHY

1. Pörtner, Hans O., Martina Langenbuch, and Anke Reipschläger. "Biological impact of elevated ocean CO₂ concentrations: lessons from animal physiology and earth history." *Journal of Oceanography* 60.4 (2004): 705-718.
2. Polley, H. Wayne, et al. "Changes in Grassland Communities a Response to Rising CO₂ Concentrations?." *Carbon dioxide, populations, and communities* (1996): 177. Camper, Dean, et al. "Gas solubilities in room-temperature ionic liquids." *Industrial & Engineering Chemistry Research* 43.12 (2004): 3049-3054.
3. Meinshausen, Malte, et al. "The RCP greenhouse gas concentrations and their extensions from 1765 to 2300." *Climatic change* 109.1-2 (2011): 213.
4. Change, IPCC Climate. "The Fourth Assessment Report of the Intergovernmental Panel on Climate Change." *Geneva, Switzerland* (2007).
5. Lacis, Andrew A., et al. "Atmospheric CO₂: Principal control knob governing Earth's temperature." *Science* 330.6002 (2010): 356-359.
6. Ziska, Lewis H., Paul R. Epstein, and William H. Schlesinger. "Rising CO₂, climate change, and public health: exploring the links to plant biology." *Environmental health perspectives* 117.2 (2009): 155.
7. Keeling, R. F., et al. *Atmospheric carbon dioxide record from Mauna Loa*. ESS-DIVE (Environmental System Science Data Infrastructure for a Virtual Ecosystem); Oak Ridge National Laboratory (ORNL), Oak Ridge, TN (United States), 2009. Atkin, Rob, and Gregory G. Warr. "Structure in confined room-temperature ionic liquids." *The Journal of Physical Chemistry C* 111.13 (2007): 5162-5168.
8. Haigh, Joanna. "A brief history of the Earth's CO₂," *www.bbc.com*. British Broadcasting Corporation, Oct. 19th 2017. Web. Oct. 25, 2017.
9. Amthor, J. S. "Respiration in a future, higher-CO₂ world." *Plant, Cell & Environment* 14.1 (1991): 13-20.
10. Seppänen, O. A., W. J. Fisk, and M. J. Mendell. "Association of ventilation rates and CO₂ concentrations with health and other responses in commercial and institutional buildings." *Indoor air* 9.4 (1999): 226-252.
11. "CARBON DIOXIDE." *Centers for Disease Control and Prevention*, Centers for Disease Control and Prevention, 28 Sept. 2011, www.cdc.gov/niosh/pel88/124-38.html.

12. Rice, Susan A. "Health Effects of Acute and Prolonged CO₂ Exposure in Normal and Sensitive Populations." (2003).
13. Yasuda, Tomomi, Seiichiro Yonemura, and Akira Tani. "Comparison of the characteristics of small commercial NDIR CO₂ sensor models and development of a portable CO₂ measurement device." *Sensors* 12.3 (2012): 3641-3655.
14. Park, JongSeon, HeeChan Cho, and SeungHwan Yi. "NDIR CO₂ gas sensor with improved temperature compensation." *Procedia Engineering* 5 (2010): 303-306.
15. Kwon, Jongwon, et al. "A study on NDIR-based CO₂ sensor to apply remote air quality monitoring system." *ICCAS-SICE, 2009*. IEEE, 2009.
16. Wang, Chengxiang, et al. "Metal oxide gas sensors: sensitivity and influencing factors." *Sensors* 10.3 (2010): 2088-2106.
17. Barsan, Nicolae, and Udo Weimar. "Conduction model of metal oxide gas sensors." *Journal of Electroceramics* 7.3 (2001): 143-167.
18. Miller, Derek R., Sheikh A. Akbar, and Patricia A. Morris. "Nanoscale metal oxide-based heterojunctions for gas sensing: a review." *Sensors and Actuators B: Chemical* 204 (2014): 250-272.
19. Tierney, Michael J., and Hyun Ok L. Kim. "Electrochemical gas sensor with extremely fast response times." *Analytical Chemistry* 65.23 (1993): 3435-3440.
20. J. R. Stetter and J. Li, "Amperometric gas sensors a review," *Chemical reviews*, vol. 108, pp. 352-366, 2008.
21. Finotello, J. E. Bara, D. Camper, and R. D. Noble, "Room-temperature ionic liquids: temperature dependence of gas solubility selectivity," *Industrial & Engineering Chemistry Research*, vol. 47, pp. 3453-3459, 2008.
22. Tokuda, Hiroyuki, et al. "How ionic are room-temperature ionic liquids? An indicator of the physicochemical properties." *The Journal of Physical Chemistry B* 110.39 (2006): 19593-19600.
23. Swan, Melanie. "Sensor mania! the internet of things, wearable computing, objective metrics, and the quantified self 2.0." *Journal of Sensor and Actuator Networks* 1.3 (2012): 217-253.
24. Wilkes, John S. "A short history of ionic liquids—from molten salts to neoteric solvents." *Green Chemistry* 4.2 (2002): 73-80.
25. Carlin, Richard T., et al. "Dual intercalating molten electrolyte batteries." *Journal of the Electrochemical Society* 141.7 (1994): L73-L76.

26. Holbrey, John D., and Kenneth R. Seddon. "The phase behaviour of 1-alkyl-3-methylimidazolium tetrafluoroborates; ionic liquids and ionic liquid crystals." *Journal of the Chemical Society, Dalton Transactions* 13 (1999): 2133-2140.
27. G.-H. Min, T.-e. Yim, H.-Y. Lee, D.-H. Huh, E.-j. Lee, J.-y. Mun, *et al.*, "Synthesis and properties of ionic liquids: imidazolium tetrafluoroborates with unsaturated side chains," *Bulletin of the Korean Chemical Society*, vol. 27, pp. 847-852, 2006.
28. A. N. Soriano, B. T. Doma Jr, and M.-H. Li, "Solubility of carbon dioxide in 1-ethyl-3-methylimidazolium tetrafluoroborate," *Journal of Chemical & Engineering Data*, vol. 53, pp. 2550-2555, 2008.
29. Bates, Eleanor D., *et al.* "CO₂ capture by a task-specific ionic liquid." *Journal of the American Chemical Society* 124.6 (2002): 926-927.
30. B.-H. Lim, W.-H. Choe, J.-J. Shim, C. S. Ra, D. Tuma, H. Lee, *et al.*, "High-pressure solubility of carbon dioxide in imidazolium-based ionic liquids with anions [PF₆] and [BF₄]," *Korean journal of chemical engineering*, vol. 26, pp. 1130-1136, 2009.
31. S. Chen, S. Zhang, X. Liu, J. Wang, J. Wang, K. Dong, *et al.*, "Ionic liquid clusters: structure, formation mechanism, and effect on the behavior of ionic liquids," *Physical Chemistry Chemical Physics*, vol. 16, pp. 5893-5906, 2014.
32. Wan, Hao, *et al.* "Miniaturized Planar Room Temperature Ionic Liquid Electrochemical Gas Sensor for Rapid Multiple Gas Pollutants Monitoring." *Sensors and Actuators B: Chemical* (2017).
33. C. Aliaga, C. S. Santos, and S. Baldelli, "Surface chemistry of room-temperature ionic liquids," *Physical Chemistry Chemical Physics*, vol. 9, pp. 3683-3700, 2007.
34. Sato, Takaya, Gen Masuda, and Kentaro Takagi. "Electrochemical properties of novel ionic liquids for electric double layer capacitor applications." *Electrochimica Acta* 49.21 (2004): 3603-3611.
35. Bazant, Martin Z., Brian D. Storey, and Alexei A. Kornyshev. "Double layer in ionic liquids: Overscreening versus crowding." *Physical Review Letters* 106.4 (2011): 046102.
36. Fedorov, Maxim V., and Alexei A. Kornyshev. "Ionic liquid near a charged wall: structure and capacitance of electrical double layer." *The Journal of Physical Chemistry B* 112.38 (2008): 11868-11872.
37. Kurzweil, Peter. "Electrochemical double-layer capacitors." *Electrochemical Energy Storage for Renewable Sources and Grid Balancing*. 2015. 345-407.

38. Weingarth, D., et al. "A reliable determination method of stability limits for electrochemical double layer capacitors." *Electrochimica Acta* 103 (2013): 119-124.
39. Kornyshev, Alexei A. "Double-layer in ionic liquids: paradigm change?" (2007): 5545-5557.
40. Cadena, Cesar, et al. "Why is CO₂ so soluble in imidazolium-based ionic liquids?" *Journal of the American Chemical Society* 126.16 (2004): 5300-5308.
41. Scovazzo, Paul, et al. "Regular solution theory and CO₂ gas solubility in room-temperature ionic liquids." *Industrial & engineering chemistry research* 43.21 (2004): 6855-6860.
42. Bazant, Martin Z., Brian D. Storey, and Alexei A. Kornyshev. "Double layer in ionic liquids: Overscreening versus crowding." *Physical Review Letters* 106.4 (2011): 046102.
43. Atkin, Rob, and Gregory G. Warr. "Structure in confined room-temperature ionic liquids." *The Journal of Physical Chemistry C* 111.13 (2007): 5162-5168.
44. A. Yokozeki, M. B. Shiflett, C. P. Junk, L. M. Grieco, and T. Foo, "Physical and chemical absorptions of carbon dioxide in room-temperature ionic liquids," *The Journal of Physical Chemistry B*, vol. 112, pp. 16654-16663, 2008.
45. Huddleston, Jonathan G., et al. "Characterization and comparison of hydrophilic and hydrophobic room temperature ionic liquids incorporating the imidazolium cation." *Green chemistry* 3.4 (2001): 156-164.
46. Brackbill, J. U., Douglas B. Kothe, and Charles Zemach. "A continuum method for modeling surface tension." *Journal of computational physics* 100.2 (1992): 335-354.
47. Restolho, José, José L. Mata, and Benilde Saramago. "Electrowetting of ionic liquids: Contact angle saturation and irreversibility." *The Journal of Physical Chemistry C* 113.21 (2009): 9321-9327.
48. X. Hu and W. Yang, "Planar capacitive sensors-designs and applications," *Sensor Review*, vol. 30, pp. 24-39, 2010.
49. Scovazzo, Paul, et al. "Supported ionic liquid membranes and facilitated ionic liquid membranes." 2002. 69-87.
50. Li, Haitao, et al. "Low power multimode electrochemical gas sensor array system for wearable health and safety monitoring." *IEEE Sensors Journal* 14.10 (2014): 3391-3399.
51. E. P. Randviir and C. E. Banks, "Electrochemical impedance spectroscopy: an overview of bioanalytical applications," *Analytical Methods*, vol. 5, pp. 1098-1115, 2013.

52. Barrosse-Antle, Laura E., Christopher Hardacre, and Richard G. Compton. "Voltammetric currents in room temperature ionic liquids can reflect solutes other than the electroactive species and are influenced by carbon dioxide." *The Journal of Physical Chemistry B* 113.9 (2009): 2805-2809.
53. Munje, R. D., E. Graef, and S. Prasad. "Interfacial impedance based electrochemical detection of carbon dioxide using RTIL." *Nanotechnology Materials and Devices Conference (NMDC), 2016 IEEE*. IEEE, 2016.
54. Graef, Edward W., Rujuta D. Munje, and Shalini Prasad. "A Robust Electrochemical CO₂ Sensor Utilizing Room Temperature Ionic Liquids." *IEEE Transactions on Nanotechnology* (2017).
55. S. G. Kazarian, B. J. Briscoe, and T. Welton, "Combining ionic liquids and supercritical fluids: in situ ATR-IR study of CO₂ dissolved in two ionic liquids at high pressures Electronic supplementary information (ESI) available: schematic view of the miniature high-pressure flow cell. See <http://www.rsc.org/suppdata/cc/b0/b005514j>," *Chemical Communications*, pp. 2047-2048, 2000.S
56. Finotello, Alexia, et al. "Room-temperature ionic liquids: temperature dependence of gas solubility selectivity." *Industrial & Engineering Chemistry Research* 47.10 (2008): 3453-3459.
57. Moganty, Surya Sekhar. *Thermodynamic, transport and electrochemical properties of room temperature ionic liquids*. Clarkson University, 2009.
58. Shiflett, Mark B., et al. "Carbon dioxide capture using ionic liquid 1-butyl-3-methylimidazolium acetate." *Energy & Fuels* 24.10 (2010): 5781-5789.
59. de Riva, Juan, et al. "Ionic liquids for post-combustion CO₂ capture by physical absorption: Thermodynamic, kinetic and process analysis." *International Journal of Greenhouse Gas Control* 61 (2017): 61-70.
60. Barrosse-Antle, Laura E., Christopher Hardacre, and Richard G. Compton. "Voltammetric currents in room temperature ionic liquids can reflect solutes other than the electroactive species and are influenced by carbon dioxide." *The Journal of Physical Chemistry B* 113.9 (2009): 2805-2809.
61. Li, Peilin, et al. "Rate and Extent of Carbon Dioxide Uptake In Room Temperature Ionic Liquids: A New Approach Using Microdisc Electrode Voltammetry." *Electroanalysis* 25.10 (2013): 2268-2274.

BIOGRAPHICAL SKETCH

Edward William Graef Jr. was born in Saint Louis, MO. After the completion of his schoolwork at Seckman Senior High School, he entered Southeast Missouri State University in Cape Girardeau, MO in 2003. During the summers of 2006 and 2007, he was awarded REU positions at the University of Arkansas in their Microelectronics-photonics program. Upon graduating with a Bachelor of Science majoring in both Physics and Engineering Physics in December of 2007, he entered the University of Arkansas' Microelectronics-photonics program. He completed his Master of Science in Microelectronics-photonics in August of 2010 with a thesis titled "Thinning of Solid State Nanopores." He then entered The University of Texas at Dallas pursuing a Doctorate of Philosophy in Physics. From May 2013 to January of 2016 he worked as the Test Engineer at L-3 Communications Infrared Products. Since January of 2016 he has worked on a Semiconductor Research Council sponsored project developing a CO₂ gas sensor utilizing Room Temperature Ionic Liquids in conjunction with mentors at Texas Instruments.

CURRICULUM VITAE

EDUCATION

Doctorate of Philosophy Candidate

The University of Texas at Dallas, Department of Physics, Dallas, TX

Dissertation: Empirical Investigation of CO₂ Utilizing Room Temperature Ionic Liquids

Attending: August 2010 to Present

Masters of Science, Microelectronics-photonics

The University of Arkansas, Microelectronics-photonics Program, Fayetteville, AR,

Thesis: Reducing the Thickness of Silicon Nitride Nanopores.

Graduated: August 2010

Bachelors of Science, Physics & Engineering Physics

Southeast Missouri State University, Department of Physics and Engineering Physics,
Cape Girardeau, MO,

Graduated: December 2007

EXPERIENCE

PhD. Graduate Student

August 2017 – Present

The University of Texas at Dallas, Department of Physics, BMNL

1. Designed and completed DOE for collection of humidity and temperature based studies of RTIL based sensors utilizing dielectric spectroscopy.
2. Developed DOE for FTIR analysis of RTILs doped with different humidity and CO₂ concentrations for better understanding of bulk behavior.

3. Currently working on chronoamperometry DOE experiments for long term cycle testing of material and sensor variation.

SRC Engineering Intern

May 2017 - August 2017

Texas Instruments, TMG/Analog Signal Chain, Temperature and Humidity Sensing Group

1. Developed automated Labview software to reduce user touch time on data collection of temperature and humidity sensors.
2. Outlined DOE for root cause analysis of high contact resistance post probe and worked with production to acquire necessary material.

PhD. Graduate Student

January 2016 - May 2017

The University of Texas at Dallas, Department of Physics, BMNL

1. Designed and constructed a semiautonomous environment chamber for controlled testing and data collection of room temperature ionic liquid based sensors.
2. Developed settings and procedures for inkjet printing of RTILs onto different sensor geometries.
3. Investigated impedance variance of room temperature ionic liquids utilizing dielectric spectroscopy in controlled environments.
4. Determined impedance response and models for selected ionic liquids when exposed to different CO₂ and humidity concentrations at varying temperatures.

Senior Test Engineer

October 2013 - January 2016

L-3 Communications, Warrior Systems Division, Infrared Products

1. Owned and maintained all test yield points for MEMS based silicon thermal imaging sensors.

2. Developed C/C++ automated testing methods for collection of sensor data to determine detector quality for delivery.
3. Created uniform C/C++ testing methodologies across all yield points to provide detailed data for resolving key Pareto items.
4. Reduced cycle time at wafer probe by 83% for all product lines.
5. Worked on multidisciplinary teams to address quality and yield impacts involved with customer returns.
6. Delivered presentations and assisted in proposals to both internal and external customers for current and new specifications across different sensor technologies.

Production Engineering Intern

May 2013 - October 2013

L-3 Communications, Warrior Systems Division, Infrared Products

1. Developed C/C++ control software to automate wafer probing of MEMS based silicon thermal imaging sensors.
2. Created C/C++ test algorithms for deployment across all test yield points in efforts to provide uniform data sources for front end and back end engineering analysis.

PhD. Graduate Researcher

January 2012 - May 2013

The University of Texas at Dallas, Department of Physics, Space Science Group

1. Assembled unmanned aerial systems capable of transporting sensor packages for UV, IR, and visible spectra collection.
2. Correlated PM2.5 data with low altitude particulate data sets to help determine local drivers of particulate generation.

3. Analyzed satellite and air based images via MATLAB self-learning algorithms for creation of secondary analysis products such as normalized vegetative indices to correlate soil moisture to atmospheric dust concentration.

Graduate Researcher

January 2008 - August 2010

Department of Physics, Microelectronics-photonics Program, University of Arkansas, Fayetteville

1. Created silicon nitride nanopores using FIB and low energy ion beam sculpting to study the in vitro properties of DNA and proteins.
2. Analyzed wet and dry etching methods via TEM for control of nanopore thickness in efforts to increase the resolution of these biosensors.
3. Developed MATLAB code for thickness analysis of nanopores via EFTEM EELS data.
4. Used EFTEM EELS results; created a geometric model that describes the topology of a nanopore.

SKILLS

ANALYTICAL SKILLS

1. Microscopy: TEM, STEM, EELS, SEM, FIB, custom ion beam.
2. Electronics: Impedance spectroscopy techniques, voltammetry techniques, and basic electronics.
3. Practical: Basic machining, circuit troubleshooting, optical design, and custom algorithm development.

COMPUTER SKILLS

1. Languages & Software: C/C++, Python, MATLAB, LabWindowsCVI, LabView, IGOR, Origin, MS Suite.

2. Operating Systems: Windows, Linux, OS X.

LEADERSHIP SKILLS

1. Educated undergraduate and graduate students on operation of gas and inkjet systems.
2. Lead and assisted on multidisciplinary teams resolving customer returns and requests.
3. Trained technicians on proper protocols of test equipment and data logging.
4. Educated graduate students on proper TEM and lab practices.

HONORS & SOCIETIES

1. SRC & TxACE Best Poster Award - 2016
2. NSF GK-12 Fellowship - 2008
3. Sigma Pi Sigma Physics Honors Society - 2007
4. American Physical Society
 - a. Local Society President - 2006-2007
5. Eagle Scout Award - 2003

PUBLICATIONS

1. E. Graef, R. Munje, and S. Prasad, "A Robust Electrochemical CO₂ Sensor Utilizing Room Temperature Ionic Liquids", IEEE Transactions on Nanotechnology 99 (2017).
2. M. Munje, E. Graef, S. Prasad, "Interfacial impedance based electrochemical detection of carbon dioxide using RTIL." IEEE NMDC Conference, Oct. 2016.
3. R. Rollings, E. Graef, N. Walsh, S. Nandivada, M. Benamara, and J. Li "The effects of geometry and stability of solid-state nanopores on detecting single DNA molecules." Nanotechnology 26 (2015).

4. R. Rollings, E. Graef, D. Tita, S. Nandivada, M. Benamara, J. Li "The Effect of Ion Beam Sculpted Nanopore Size and Shape on DNA Translocation." Bulletin of the American Physical Society 56 (2011).
5. E. Graef, C. Hyun, M. Benamara, J. Li "Modification of Solid State Nanopore Characteristics Through Chemical Etching." Bulletin of the American Physical Society 55 (2010).